



Gran Sasso Science Institute
Scuola Internazionale Superiore di Studi Avanzati



The potential of Imaging Atmospheric Cherenkov Telescope arrays for morphological and spectrometric studies

PhD thesis

submitted April 14, 2017

PhD Candidate

Lucia Ambrogi

Advisor

Prof. Felix Aharonian

Dublin Institute for Advanced Studies, Dublin, Ireland

Max Planck Institute for Nuclear Physics, Heidelberg, Germany

Gran Sasso Science Institute, L'Aquila, Italy

Co-advisor

Dr. Emma de Oña Wilhelmi

Institute for Space Sciences (CSIC/IEEC), Barcelona, Spain

Gran Sasso Science Institute

Ciclo XXIX

Acknowledgements

I would like to express my sincere gratitude to my supervisors Felix Aharonian and Emma De Oña Wilhelmi for their support and their advices: without your precious knowledge and your expertise this work would not have been possible. Thank you very much for the good work together and for your help during these years. I would like to thank also Giovanni Morlino and Roberta Zanin for the careful reading of parts of this work and the relevant comments they sent me. I am also grateful to GSSI and its staff for providing an exciting scientific environment where to grow and improve.

I thank my family, who has given me the motivation and the support I needed during these years. I wish I'll make you always proud of me. I want to thank also my old friends, for being the beautiful women they are. A very special thanks goes to my friends here in L'Aquila: without you this period of my life would not have been the same, you deserve a special place in my heart. Lastly, thank you Ivano for your support, encouragement, patience and all the smiles that you managed to get out of me. I wish I could do the same with you one day.

Contents

1	Gamma-ray astronomy with Imaging Atmospheric Cherenkov Telescopes	1
1.1	Detection techniques	2
1.1.1	Space-based instruments	3
1.1.2	Ground-based instruments	5
1.2	Extensive atmospheric showers	7
1.2.1	Electromagnetic showers	7
1.2.2	Hadronic showers	9
1.2.3	The Cherenkov effect	10
1.3	Imaging Atmospheric Cherenkov Telescopes	12
1.3.1	The imaging of the Cherenkov light	12
1.3.2	Signal and background characterization	13
1.3.3	The stereoscopic imaging	16
1.3.4	Technical features of the telescopes	17
1.4	Current IACT instruments	18
1.5	The Cherenkov Telescope Array	20
1.5.1	CTA layout	21
1.5.2	CTA performance	24
1.5.3	Science with CTA	25
2	Morphological studies	29
2.1	Instrument response parameterization	29
2.1.1	Angular resolution	30
2.1.2	Effective Area	33
2.1.3	Energy resolution	33
2.1.4	Background rate	34
2.2	Methodology	35
2.3	Isolated source	36
2.3.1	Event rates and background regimes	36
2.3.2	Signal-to-noise	38
2.3.3	Reconstruction of morphological parameters for Gaussian PSF response	40
2.3.4	Reconstruction of morphological parameters for non-Gaussian PSF response	41
2.4	Multiple sources	44
2.4.1	Two nearby sources	44
2.4.2	Compact source on a diffuse, halo-type, extended source	46

3	Sensitivity studies	51
3.1	Methodology	51
3.2	Two neighbor sources	52
3.2.1	Event rate	52
3.2.2	The sensitivity	56
3.3	Extended sources	60
3.3.1	Event rates	60
3.3.2	The sensitivity	61
4	Spectrometric studies	69
4.1	Methodology	71
4.2	Power-law	72
4.3	Power-law with exponential cutoff	75
4.4	Broken power-law	79
5	Summary and conclusions	83
A	Gamma-ray production and absorption mechanisms	89
A.1	Basic overview	89
A.2	Interactions in radiation field	91
A.3	Interactions in magnetic field	94
A.4	Interactions in matter field	97
A.5	Dark Matter annihilation	99
B	Very high energy gamma-ray sources	101
B.1	Galactic sources	101
B.1.1	Pulsars and pulsar wind nebula	101
B.1.2	Supernova remnants	103
B.1.3	Supernova remnants interacting with molecular clouds	104
B.1.4	Compact binary systems	105
B.1.5	The Galactic Center and the Galactic ridge	105
B.2	Extragalactic sources	107
B.2.1	Active galactic nuclei	107
B.2.2	Gamma-ray bursts	109
B.2.3	Starburst galaxies	109
B.2.4	Galaxy clusters	110

Abstract

In recent years, the current generation of ground-based gamma-ray telescopes has proved the great potential of the stereoscopic arrays of Imaging Atmospheric Cherenkov Telescopes (IACTs) as effective multifunctional tools for spectral and morphological studies of gamma-ray sources at energies from a few tens of GeV up to tens of TeV. The next generation IACT observatory, namely the Cherenkov Telescope Array (CTA), is designed to pursue the next step of development in terms of instrument performance. Consequently, a strong impact on our understanding of the non-thermal Universe is foreseen. In this work, the actual potential of the next generation IACT arrays in general, and CTA, in particular, to perform morphological and spectrometric studies of very high energy (VHE) gamma-ray sources is explored.

In addition to the ideal (Gaussian form) point spread function (PSF), the impact of more realistic non-Gaussian PSFs with extended tails has been considered. Simulations of isolated point-like and extended sources have been performed, motivated by the fact that morphological studies of complex regions of extended emission or regions crowded by gamma-ray sources, such as the region of the Galactic Center, represent one of the main challenges to be faced by the the upcoming observatory. The simulations have been used to understand the response of the instrument under different assumptions regarding the PSF model. When the contribution of the tails accounts for $\geq 5\%$ of the Gaussian PSF, the reconstruction of the source morphology is significantly compromised, due to the artificial emission induced by the presence of the tails.

Then, the capability of the instrument to resolve multiple sources has been analyzed and the corresponding instrument sensitivities calculated. It has been shown that, depending on the PSF shape and on the distance to the test source, the presence of a nearby gamma-ray emitter increases the minimum detectable flux up to an order of magnitude with respect to what foreseen by CTA in case of an isolated point-like source and Gaussian PSF. The CTA expectations on the flux sensitivity are found to be reduced also in correspondence to isolated extended objects. The worsening is especially significant in the low energy domain: around few tens of GeV, a degradation of the sensitivity by an order of magnitude or more is expected. These results should be taken into account when planning the observations with future IACT arrays, especially in the densely populated part of the Galactic plane, where the chance of clustering of two or more gamma-ray sources within 1 deg is high and many of the objects are found to be better described as extended sources, rather than point-like.

Finally, the potential of CTA for spectrometric studies of VHE gamma-ray objects has been evaluated. Besides the featureless, e.g. pure power-law, energy spectra, the cases of spectra with ex-

ponential cutoffs and broken power-law energy distributions have been examined. It has been demonstrated that the significant improvement expected for CTA regarding both the detection area and the energy resolution will allow the reconstruction of energy spectra with sharp spectral features with great accuracy. Sharp cutoffs or breaks around tens of TeV could be properly reconstructed, provided adequate exposure times (≥ 50 hours) and moderately strong sources ($\sim 10\%$ of Crab Nebula flux).

The thesis is organized as follows:

- In **Chapter §1** the IACT detection technique is described and the current and future Cherenkov telescopes are reviewed.
- In **Chapter §2** the morphological studies of point-like and extended gamma-ray objects are reported and the accurate modeling of the PSF shape to determine CTA's ability to resolve confused region is explored. The results described in this chapter have passed through an internal review by the CTA Consortium and have been published in [71] and [70].
- In **Chapter §3** the study of the CTA sensitivity in case of a companion gamma-ray emitter in the proximity of a test source is disclosed. This section is based on the results published in [71], after the approval for publication by the CTA Consortium. Then, the instrument sensitivity to extended sources is discussed. At the time of writing, this part of the work is ready to be submitted to the internal review by the CTA and the KM3NeT Consortiums.
- In **Chapter §4** the spectrometric studies of VHE gamma-ray objects and the modeling of the CTA's ability to reconstruct abrupt spectral features, in form of cutoffs and spectral breaks, are presented. This part of the work already passed the internal review by the CTA Consortium and a paper based on these results has been submitted to *Astroparticle Physics Journal*.
- The main results of the work are summarized in **Chapter §5**.
- In **Appendix §A** a description of the different gamma-ray production and absorption mechanisms is given, while in **Appendix §B** an overview of the known and potential astronomical sources expected to emit in the VHE domain is presented. The survey presented in these appendices is not essential to the ultimate intent of the work and the reader familiar with these topics can skip this section. Nevertheless, for the sake of completeness, it is given as a useful support for the reader who is not expert in the field to understand the importance of the scientific results described throughout the thesis.

1

Gamma-ray astronomy with Imaging Atmospheric Cherenkov Telescopes

Our current knowledge of the Universe comes almost entirely from the detection of the electromagnetic radiation, a powerful mean to explore the distant cosmos. After the telescope was invented in the 17th century, astronomy went through a revolution which made the scientists able to investigate weak sources visible in the optical. After this huge step, much progress has been made: new techniques were developed and other parts of the electromagnetic spectrum were reached and exploited to learn about the Universe.

During the recent years, a new window in the observation of the electromagnetic components has been opened, up to the highest energies. Thanks to the availability of new detectors coming from technologies typical of the experimental particle physics, the gamma-ray astronomy made possible the exploration of the upper end part of the electromagnetic spectrum. Photon radiation in the gamma-ray band differs fundamentally from lower energy radiation: MeV to TeV gamma rays cannot be created thermally in celestial systems. Therefore, very high energy gamma rays are ideal carriers of information about non-thermal relativistic processes in astrophysical objects. They are copiously produced in many galactic and extragalactic sources and they do freely propagate in space without deflection by interstellar and intergalactic magnetic fields, making their detection a direct link to their source of origin.

Space-based experiments cover a broad energy band of primary gamma rays, from few MeV to tens of GeV. However, beyond tens of GeV the gamma-ray photon statistics is too small for detectors on board of satellites and larger detection areas are needed. In the TeV domain, gamma rays can be effectively detected by ground-based detector, and among various techniques, the Imaging Atmospheric Cherenkov Telescope (IACT) technique has proven to be the most promising approach. In 1989 the Crab Nebula was observed by the Whipple IACT for the first time [187]. Following this detection, many very high energy gamma-ray objects have been detected with past and current IACT instruments, firmly confirming the gamma-ray astronomy as a discipline in its own right [30].

Gamma-ray astronomy has revealed several categories of objects whose emission is dominated by non-thermal processes, as shown in Fig. 1.1. The total number of detected TeV sources is currently approaching the level of

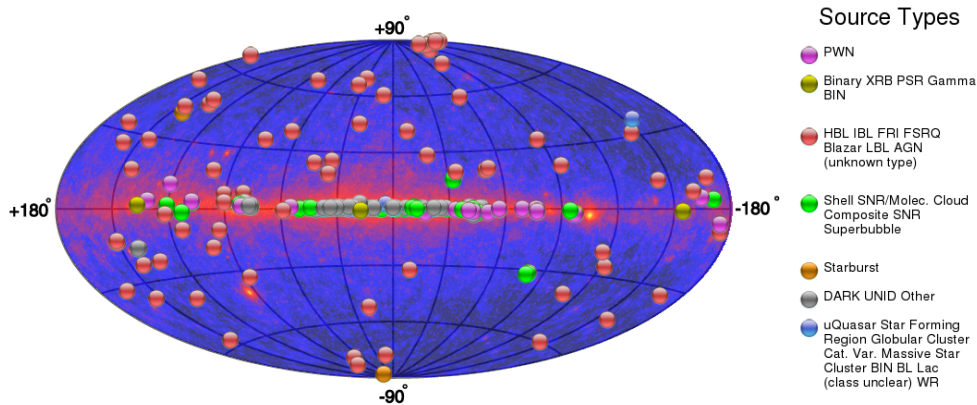


Figure 1.1: The locations, in Galactic coordinates, of all reported astrophysical sources of TeV gamma-ray emission (Winter 2017) displayed with different color code according to their source population identity. The Fermi skymap is also reported in the map. Extracted from the online TeV catalog (<http://tevcat.uchicago.edu>).

200 (!) and this number will dramatically (by at least an order of magnitude) increase as the next-generation IACT will be operational. The Cherenkov Telescope Array (CTA) will be the major future observatory for very high energy gamma-ray astronomy and it is expected to significantly boost the scientific discoveries in the field.

1.1 Detection techniques

High energy astrophysical processes are known to produce relativistic particles and the associated gamma-ray radiation over an extremely vast range of energy. The energy domain covered by the cosmic gamma-ray radiation spans at least 14 energy decades, from 100 keV to 100 EeV, more than all the rest of the electromagnetic spectrum (i.e. from MHz radio waves to keV X-rays) [32]. The lower bound is associated with the characteristic energy of nuclear gamma-ray lines, while the upper bound is fixed by the maximum energy observed in cosmic rays. This huge energy band is generally divided into sub ranges:

- *low energy* (LE) gamma rays, with $E \in [0.1 - 100]$ MeV
- *high energy* (HE) gamma rays, with $E \in [0.1 - 100]$ GeV
- *very high energy* (VHE) gamma rays, with $E \in [0.1 - 100]$ TeV
- *ultra high energy* (UHE) gamma rays, with $E > 100$ TeV

These gamma-ray regions are not defined by the physics of their production but rather by the techniques employed in their detection [186]. A wide variety of detection methods is used to cover the whole energy range. The sky below 100 MeV is mostly observed with Compton telescopes (see e.g. [186] for further

details concerning this detection technique) but unfortunately it is a poorly explored field, due to the lack of detectors with an appropriate sensitivity.

As for the LE, also the HE range is covered by space-based experiments. These instruments are placed beyond the atmospheric absorption and therefore they directly observe the HE photons. Recent results have been obtained with space-based instruments such as the Fermi Large Area Telescope (LAT) [79] and the AGILE satellites [173], providing new insights into the HE gamma-ray sky. However, given the constraints on the maximum weight and size of an instrument that has to be launched into space, the effective detection area of any satellite is limited to $\sim 1 \text{ m}^2$. This significantly limits the observations of gamma-ray sources above 100 GeV from the space [35].

To overcome the limits of space-borne observatories, the energy ranges typical of VHE and UHE gamma rays are generally covered by ground-based experiments. Counting on huge detection areas and effective rejection of cosmic-ray background events, ground-based detectors are the only instruments capable to study emitters in this energy domain, characterized by very low gamma-ray flux ($\mathcal{O}(10^{-11})$ photons/cm²s above 1 TeV for strong sources (Crab-like flux level¹) [126]). Earth's atmosphere is opaque to gamma-ray photons, it effectively arrests all electromagnetic radiation of energies greater than 10 eV. Therefore, gamma-ray detection from the ground takes advantage of the absorption and reconstructs the primary gamma rays from the products of their interaction with the medium.

1.1.1 Space-based instruments

As mentioned above, the only way to directly detect primary gamma rays is through detectors located in balloons or satellites. Unlike optical photons, gamma rays cannot be refracted by a lens or reflected by a mirror, thus they cannot be focused. Their detection with space-based detectors makes use of techniques similar to those of particle physics, exploiting the electron-positron pair production induced by the interaction of the primary photon with the detector medium. A schematic illustration of a pair conversion telescope is shown in Fig. 1.2. An anti-coincidence system (AS) made of plastic scintillators and read out by photomultiplier tubes (PMTs) is used to veto charged particles. The gamma ray candidate, entering the detector without producing a signal in the AS, interacts within thin sheets of high-Z material, leading to the production of electron positron pairs. The trajectories of pairs detected by the tracker give information about the direction of the primary gamma-ray photon. The energy of the latter is measured by the energy deposited in the calorimeter located below the trackers. Combining together the information from the AS, the tracker and the calorimeter it is therefore possible to reconstruct the energy and the direction of the primary photon, and reject the background induced by the charged cosmic rays.

The first gamma-ray telescope carried into orbit, on the Explorer 11 satellite in 1961, collected less than 100 cosmic gamma-ray photons [142]. Few

¹The Crab flux at 1 TeV corresponds to $2.8 \cdot 10^{-11}$ photons $\text{TeV}^{-1} \text{cm}^{-2} \text{s}^{-1}$ as in ref. [38].

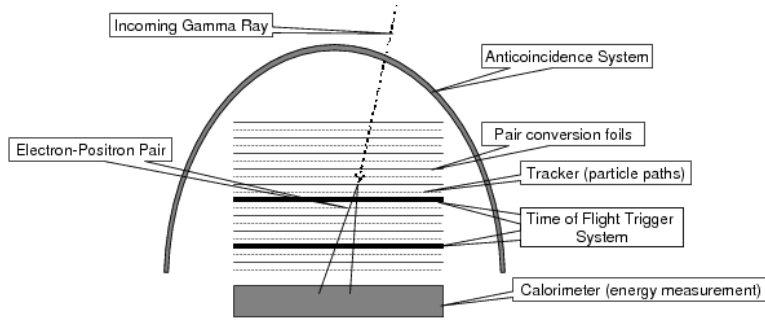


Figure 1.2: Schematic illustration of a pair production telescope. Extracted from [175].

years later, in 1967, the first robust detection of gamma-ray emission was obtained by the gamma-ray detector aboard the OSO-3 satellite [93]. In the 70s the field of space-based gamma-ray astronomy made strong progress with the SAS-2 (1972) [109] and the COS-B (1975-1982) satellites [87]. In 1991, NASA launched the Compton Gamma Ray Observatory (CGRO), which was successfully operated until June 2000. The CGRO carried on board four gamma-ray instruments, each with its own energy domain, detection technique and scientific goals. The overall energy coverage was from 15 keV to > 30 GeV. The detector of higher energies (from 30 MeV to 30 GeV) was EGRET, based on the same pair production technique used by SAS-2 and COS-B detectors, but with a much larger collection area ($\simeq 1500 \text{ cm}^2$), a field of view (FoV) of ~ 0.5 sr and a single-photon angular resolution of ~ 6 deg at 100 MeV [176]. During its 9 years lifetime EGRET discovered 271 sources [120] and allowed to build up the first picture of the entire HE gamma-ray sky (see [175] for a detailed review of EGRET results). However, a real breakthrough in the exploration of the sky in HE gamma rays happened after the launch of the Fermi satellite in 2008. Its main instrument is the LAT, a pair conversion detector that operates from 20 MeV to $\simeq 300$ GeV [80], reaching the TeV energies although with limited statistics [24]. The newer technology used for detection of particles, as well as the larger detection area ($\simeq 6500 \text{ cm}^2$ at 1 GeV), the larger field FoV (2.4 sr at 1 GeV) and the better angular resolution (~ 0.8 deg at 1 GeV, asymptoting reaching 0.2 deg above 20 GeV) of Fermi LAT compared to EGRET, raised the observational gamma-ray astronomy to a new level [21]. The third full catalog of LAT sources is based on the first 48 months of survey data and includes 3033 sources above 4σ significance [18]. Many important results and discoveries have been produced by Fermi, like the detection of the characteristic pion-decay signature in SNRs [22] and the discovery of the so-called *Fermi Bubbles*, bilateral bubble-like emissions centered on the core of the Milky Way and extending to ~ 10 kpc above and below the Galactic plane [23].

1.1.2 Ground-based instruments

As the atmospheric absorption prevents the gamma-ray photons from reaching the ground-based detectors, for these instruments the atmosphere itself becomes an integral part of the detection system, working as a huge calorimeter in which the primary photons (and cosmic rays as well) lose their energy and generate particle cascades. These cascades of secondary particles are called *extensive air showers* (EAS). EAS can be detected from the ground in two ways: by detecting the shower particles or by detecting the Cherenkov radiation produced in the atmosphere by the secondary electrons and positrons within the shower. Correspondingly, two types of ground based detectors are used: *air shower (particle) detectors* and *Imaging Atmospheric Cherenkov Telescopes* (IACTs).

The IACTs are basically composed by an optical reflector used to focus the Cherenkov light into a system of photo-sensors. On the other hand, air showers detectors exploit arrays of particle counters deployed on the ground to measure the particles in the showers. The two detection techniques are complementary. Air shower detectors continuously view the entire overhead sky, counting approximately 1 sr FoV and on a duty cycle larger than 90% [35]. IACTs are optical instruments, therefore they can be operated only during cloudless and moonless night, with a duty factor of the order of 10%². Also their FoV is much smaller compared to air shower instruments (\sim few msr). However, IACTs are characterized by a significantly better angular and energy resolution, lower energy threshold, excellent background rejection and, correspondingly, much higher significance per unit observing time. IACTs are basically pointing instruments while air shower observatories are suited to perform unbiased surveys to search for new or transient sources.

Air showers arrays are based on different type of particle detectors. Tibet AS-gamma [72] observatory detects the footprint of the EAS using a sparse array of plastic scintillators. It is located in Tibet (P.R. China, YangBaJing laboratory) at an altitude of 4300 m above the sea level. High altitudes are preferred for EAS arrays: the detector level is closer to the shower maximum (see §1.2 for the details about the EAS development) and this leads to a better sensitivity and lower energy threshold. At the same altitude was placed the ARGO-YBJ experiment (Tibet, P.R. China, YangBaJing laboratory, 4300 m a.s.l., taking data for five years since November 2007) [98], a full-coverage detector made of a single layer of resistive plate chambers (RPCs).

Alternatively, the air shower detectors can be tanks filled of water: when particles from the EAS pass through the water, they emit Cherenkov light (see §1.2.3 for a description of the Cherenkov radiation). Such arrays are called *water Cherenkov detectors*, see Fig. 1.3. The Milagro experiment [78] was an EAS water Cherenkov detector located near Los Alamos (New Mexico, 2650 m a.s.l., stopped taking data in April 2008 after seven years of operation). As show in Fig. 1.3, the array consists of a central pond and 175 outrigger tanks,

²The standard conditions to perform observation with an IACT require clear sky with both the Sun and the Moon below the horizon; this corresponds to an average of 1650 h/yr of possible dark observation time [86].

which increase the physical area of the detector by a factor of 8. Milagro was sensitive to energies between 100 GeV and 100 TeV and it demonstrated the sensitivity of this technique with the first detection of the galactic diffuse emission at TeV energies [77] as well as several new TeV gamma-ray sources [2].

On the experience of Milagro, the High Altitude Water Cherenkov (HAWC) experiment was built (Sierra Negra, Mexico, 4100 m a.s.l.) [7]. The HAWC gamma-ray observatory is a second-generation water Cherenkov detector. It comprises 300 identical water Cherenkov detectors (WCDs), i.e. water tanks with PMTs at the bottom, over an area of 20000 m² (see Fig. 1.3). The pattern of energy deposition in the WCDs allows for the identification of the background events, i.e. hadronic showers. While gamma-ray induced showers have compact cores with smooth lateral profile, hadronic showers typically deposit large amounts of energy in bundles far from the shower core, as described in the next section §1.2. Selection cuts based on gamma/hadron different shower morphologies eliminate > 99% of the hadronic background in the large event size (large number of hit PMTs), 85% of background near the energy threshold ($\simeq 100$ GeV), while retaining more than 50% of the gamma-ray signal events. Also the angular resolution varies with the number of hit PMTs, ranging from ~ 1 deg (near the threshold) to ~ 0.2 deg (large event size). The combination of larger effective area, high elevation and unique background rejection allows HAWC to achieve sensitivity improved by more than one order of magnitude compared to previous air shower detectors, with a sensitivity peak around 10 TeV and 1 year survey sensitivity of 5 – 10% of the Crab Nebula [7]. Recently the HAWC collaboration has released the second catalog of gamma-ray sources, in which a total of 39 sources are found. It has been realized with 507 days of data and represents the most sensitive TeV survey to date for such a large region of the sky [8].



Figure 1.3: Two water Cherenkov detectors, Milagro (on the left) and HAWC (on the right). Further details on the instruments are reported in the text.

The next-generation air shower detector will be the Large High Altitude Air Shower Observatory (LHAASO) project, to be built in China at 4410 m altitude. This multi-component experiment (scintillator detectors, water Cherenkov tanks and air Cherenkov telescopes) will continuously survey the VHE gamma-ray sky, searching for steady and transient sources from about 100 GeV to PeV energies. The completion of the installation is expected by the end of 2021; in the next decade CTA-North and LHAASO are expected to be the most sensitive instruments to study gamma-ray astronomy in the Northern hemisphere

[99].

1.2 Extensive atmospheric showers

The Earth's atmosphere is constantly bombarded by particles originating in the outer space. Among these cosmic particles, those with enough energy generate showers of secondaries, the so-called extensive atmospheric showers (EAS). Charged particles within the EAS moving through the atmosphere with velocity larger than the speed of light emit Cherenkov radiation (see §1.2.3), the detection of which allows indirect registration of the primary. Depending on the nature of the primary particle, the resulting EAS shows specific features, typical of the physical processes triggered by the interaction with the medium. Therefore, it is possible to distinguish between *electromagnetic showers*, induced by gamma rays, and *hadronic showers*, owing to cosmic-ray interactions in the upper atmosphere. The latter represent the main source of background for an IACT system. The capabilities to reject background showers is a key performance criterion for gamma-ray detection systems.

1.2.1 Electromagnetic showers

A gamma ray entering the atmosphere interacts with the medium primarily via pair production. The electron-positron pair dissipates its energy through bremsstrahlung process in the Coulomb field of the nuclei (see §A.4 for further details about the physics of the processes). Pair production and bremsstrahlung emission combined together lead to the formation of an *electromagnetic shower*.

Some properties of the electromagnetic showers can be understood within a simple toy model [122]. In this model, the radiation length X_0 represents both photon and electron mean free paths in matter, if one neglects the factor $7/9$ which links the two processes as $X_{0,brems} \simeq (7/9)X_{0,pp}$ ³. The shower is considered to develop in discrete steps, each of length equal to the radiation length, which for the air is $X_0 \simeq 36.6 \text{ g cm}^{-24}$. After $t = x/X_0$ radiation lengths, the number of particle comprising the shower at a depth x is roughly given by $N(t) = 2^t$. At each step electrons split their energy approximately in half via bremsstrahlung emission of a single photon while photons produce a pair of electron and positron with equal energy. Therefore, at t radiation lengths each particle of the shower has an average energy of $E(t) = E_0/2^t$, where E_0 is the energy of the primary photon. The exponential growth of the number of particles in the shower is interrupted when the electron rate of ionization energy loss exceeds that of bremsstrahlung. In air it happens for a critical energy $E_c \simeq 86 \text{ MeV}$. Once the average energy per particle is below 86 MeV the cascade effect is not efficient anymore and the number of particles in the shower starts to decrease. The atmospheric depth at which

³At 1 radiation length, bremsstrahlung photons lose all but $1/e$ of their energy. This length corresponds also to $7/9$ of the mean free path for the pair production process.

⁴The total vertical thickness of the atmosphere above sea level is 1030 g cm^{-2} , therefore it amounts to more than 28 radiation lengths [186].

the shower achieve the maximum number of particles is called *shower maximum*, occurring at $x_{max} = X_0 \ln(E_0/E_c)$, logarithmically increasing with energy. For a 1 TeV gamma ray this maximum atmospheric depth is of the order of 10 km. The number of particles at the maximum of the shower is $N(t_{max}) = 2^{t_{max}} \simeq E_0/E_c$, approximately proportional to the primary energy. Beyond this maximum the shower is attenuated according to $E/E_0 = (1.65)^{-k}$, where k is the number of radiation lengths after the shower maximum. As a consequence, only the 10% of the primary gamma ray energy is able to reach an observation altitude of 5200 m [35].

An accurate analytical treatment of the shower development was given by Greisen [119]. Based on the solutions of the cascade equations, the longitudinal development of the electromagnetic shower can be quantified by the total number of secondary electrons and positrons as a function of the shower depth:

$$N_e(t) = \left(\frac{0.31}{\sqrt{\ln(E_0/E_c)}} \right) \exp [t(1 - 1.5 \ln s)] \quad (1.1)$$

where $s = 3(1 + 2 \ln(E_0/E_c)X_0/x)^{-1}$ is the so-called *shower age*, parametrized so that at the shower maximum $s = 1$. The distribution of $N_e(t)$ is shown in Fig. 1.4 for different E_0 values. The angle of emission in all processes

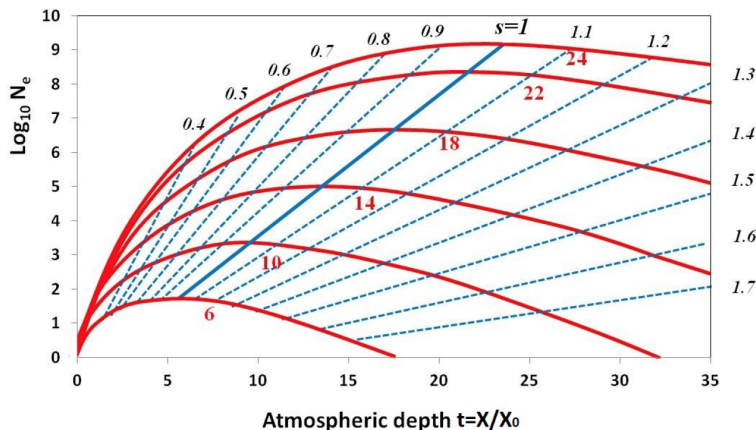


Figure 1.4: Longitudinal size of the electromagnetic shower $N_e(t)$ as a function of the shower depth $t = x/X_0$. The red numbers on the curves indicate the value of $\ln(E_0/E_c)$. Correspondingly, each red curve is for an specific value of the initial photon energy E_0 : 35 GeV, 2 TeV, 100 TeV, 5.7 PeV, 320 PeV and 2300 PeV. Blue lines define points of equal shower age s . The sea level is at $t \simeq 27$. Extracted from [170].

involved in the shower development (i.e. pair-production and bremsstrahlung, see §A.4) is $\propto m_e c/E$ rad, where E is the energy of the electron and m_e its rest mass [186]. The later distribution of the shower is determined by multiple Coulomb scattering and it scales with a quantity called *Moliere radius* R_{mol} , that is the radius of a cylinder containing roughly the 90% of the secondary particles created in the shower:

$$R_{mol} = \frac{X_0 E_s}{\rho E_c} \quad (1.2)$$

where $E_s = 21$ MeV and ρ is the density of the atmosphere. The resulting electromagnetic cascade is tightly clumped along the projection of the original gamma-ray trajectory.

1.2.2 Hadronic showers

When the primary particle interacting in the upper atmosphere is a proton or a nucleus, then an hadronic shower is created. Cosmic rays are mostly protons, with less than 10% of helium ions, and because of interstellar magnetic fields, the arrival directions of these charged particles are isotropic.

They initiate the hadronic shower after traversing on average one interaction length X_h . The products of this interaction with the atmosphere are mainly pions and kaons (about 90% and 10%, respectively). After the first interaction, pions and kaons may interact again with the nuclei in the atmosphere, or decay. The produced hadrons carry κE_0 of the primary cosmic ray energy. The parameter $\kappa \simeq 0.7$ is called the inelasticity of the process and is defined as $\kappa = (E_0 - E')/(E_0 + M_T)$, where E' is the residual energy after the collision and M_T the mass of the target nucleon. The residual energy E' is used by the leading particle (i.e. the highest energy secondary produced in the interaction) for a subsequent interaction after traversing (on average) one more X_h [170]. The process can continue until the hadron energy is below an interaction threshold. The part of the shower that continues to interact hadronically with the atmosphere constitutes the so-called *hadronic core* of the shower, and will keep on undergoing hadronic interactions until the energy per nucleon is smaller than the pion production threshold (~ 1 GeV).

Since the main component of the produced secondaries is constituted by pions, the competition between interaction and decay processes of these mesons roughly determines the details of the development of the hadronic showers. Neutral pions in the cascade have a lifetime $\tau_{\pi^0} = 8.4 \cdot 10^{-17}$ s, and therefore they decay into two photons ($\pi^0 \rightarrow \gamma + \gamma$) after traversing a distance $d_{\pi^0} = \Gamma c \tau_{\pi^0} = \Gamma \cdot 2.5 \cdot 10^{-6}$ cm, where Γ is the Lorentz factor of the pion. Given the small value of d_{π^0} , the so-called *decay length*, neutral pions decay into two photons almost as soon as they are generated. These photons in turn initiate electromagnetic showers. Note that in this process about one third of the primary energy E_0 is transferred from the hadronic to the electromagnetic component of the shower via decay of neutral pions. If the charged hadrons start to decay on average after n_d interaction lengths, then the energy in the electromagnetic component is $E_{em} \approx E_0(1 - (2/3)^{n_d})$, the so-called *calorimetric energy* of the shower [136].

On the other hand, the lifetime of charged pions is $\tau_{\pi^\pm} = 2.6 \cdot 10^{-8}$ s, corresponding to a decay length $d_{\pi^\pm} = \Gamma c \tau_{\pi^\pm} = \Gamma \cdot 780$ cm, after which they decay into muons and neutrinos ($\pi^\pm \rightarrow \mu^\pm + \nu_\mu(\bar{\nu}_\mu)$). In order to understand if charged pions keep on interacting with the atmospheric nucleons, the decay length d_{π^\pm} has to be compared with their interaction length, $\lambda_{\pi^\pm} = 120$ g/cm². For this reason, π^\pm can either interact or decay once they have been produced and the stochastic interplay of the two channels, further complicated by the

dependence of λ_{π^\pm} on the density of the atmosphere, can be fully treated only with Monte Carlo simulations [170].

The combinations of all these processes makes the hadronic showers to be formed by three main components: an hadronic core, an electromagnetic component, and a muon and neutrino component. The long lifetime of muons ($\tau_\mu = 2.2 \cdot 10^{-6}$ s) combined with small cross section for radiative processes, implies that most likely they will survive to the ground before they decay ($\mu^\pm \rightarrow e^\pm + \nu_e(\bar{\nu}_e) + \bar{\nu}_\mu(\nu_\mu)$). For example, approximately 20% of 1 GeV muons produced at 10 km will reach the sea level before they decay [35].

Despite the very complex evolution of hadronic showers, one can extend the simple approach used in the description of the electromagnetic showers to the case of a nucleus with atomic mass number A and energy E_0 assuming that this nucleus interacting in atmosphere is equivalent to A individual single nucleons, each with energy E_0/A , and each acting independently (the so-called *superposition model*). The depth at which the shower maximum is expected can be approximated as: $x_{max} \propto X_h \ln(E_0/AE_c)$. It is important to note that the hadron interaction length $X_h \approx 80$ g/cm² is more than twice the radiation length X_0 . This means that in general the hadronic showers will reach their maximum later in atmosphere compared to electromagnetic shower initiated by primary gamma ray with the same energy.

Another important difference of hadronic showers with respect to electromagnetic showers is that hadron interactions in the core emit their secondary products at wider angles, so that the hadronic cascade is broader and more scattered [186]. The wider transverse evolution and the intrinsic fluctuations of the hadronic shower development make them more irregular than electromagnetic showers

1.2.3 The Cherenkov effect

When a charged particle moves in a dielectric medium with velocity βc greater than the phase velocity c/n of the light in the same medium (n is the refraction index of the medium), the so-called *Cherenkov radiation* is emitted. The process of production of Cherenkov radiation is illustrated in Fig. 1.5a, where the effect of a charged particle moving through the medium's atoms is shown. In the region close to the passing particle, the electric field of the particle distorts the atoms and the medium becomes polarized. While the atoms are distorted they behave like elementary dipoles. Whether the particle moves slower than the local speed of the light, i.e. $\beta c < c/n \rightarrow \beta < 1/n$, the disturbed medium relaxes back to an equilibrium as the particle transits through, owing to the complete symmetry of the polarization field surrounding the electrons. On the other hand, if the particle is faster than the light, i.e. $\beta c > c/n \rightarrow \beta > 1/n$, the medium does not relax back since since the polarization field is asymmetric. Along the axis of the particle trajectory there is a resultant dipole field which leads to the emission of an electromagnetic pulse at each element along the particle track. The wavelets from all the portions of the track interfere constructively so that Cherenkov photons are emitted [89]. This

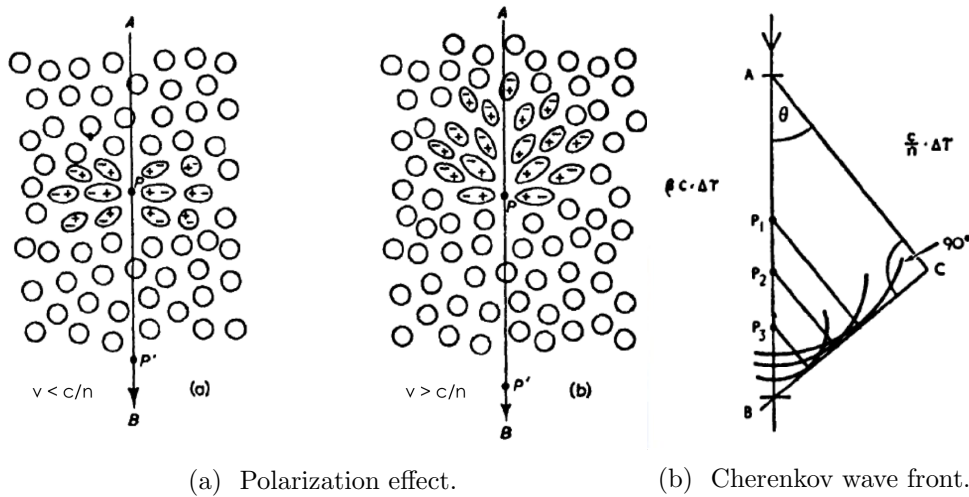


Figure 1.5: Fig. 1.5a shows the polarization effect induced by a charged particle moving through a medium with a velocity smaller (left) and larger (right) with respect to the speed of light in the same medium. Fig. 1.5b illustrates the creation of a plane wave front by the in-phase wavelets emitted by the charged particle along its track when it moves faster than light. Extracted from [89].

Cherenkov radiation is emitted at a specific angle, namely the point at which all the wavelets from arbitrary points of the track are coherent and combine to form a plane wave front. Using the terminology in Fig. 1.5b, the coherence among the wavelets is verified when the time needed by the particle to travel the segment AB is equal to the time needed by the light to travel AC . From this condition it is possible to define the *Cherenkov angle* as:

$$\cos \theta_C = \frac{1}{\beta n} \quad (1.3)$$

Eq. [1.3] fixes the minimum for the velocity of the charged particle to emit Cherenkov radiation: $\beta_{min} = 1/n$. Correspondingly, the threshold energy the particle with rest mass m needs in order to emit Cherenkov photons is:

$$E_C^{thr} = \frac{mc^2}{\sqrt{1 - \beta_{min}^2}} = \frac{mc^2}{\sqrt{1 - (1/n)^2}} \quad (1.4)$$

From Eq. [1.3] one can also define the maximum angle of the conical shaped wave front; from $\beta_{max} = 1$ it turns out that $\theta_C^{max} = \cos^{-1}(1/n)$.

It is clear from all the previous treatment that the index of refraction of the medium n is a critical parameter for understanding the Cherenkov light production. The profile of the index of refraction in atmosphere can be parametrized as a function of the altitude:

$$n(h) \approx 1 + n_0 \exp(-h/h_0) \quad (1.5)$$

where $n_0 = 2.9 \cdot 10^{-4}$ and $h_0 = 7250$ m [35]. At sea level the Cherenkov threshold energy for electrons, muons, pions and protons is 21 MeV, 4.4 GeV,

5.8 GeV and 39 GeV, respectively. Taking into account Eq. [1.5], θ_C^{max} is modified into $\theta_C^{max} \approx \sqrt{2n_0} \exp(-h/2h_0)$. Above 15 km it is less than 0.5 deg, broadening at lower altitudes up to 1 deg at 5 Km and reaching 1.4 deg at sea level.

The number of Cherenkov photons produced per unit path length and per unit of energy of a particle with charge Z is given by the *Frank-Tamm formula*:

$$\frac{d^2 N}{dx dE} = \frac{\alpha Z^2}{\hbar c} \left(1 - \frac{1}{\beta^2 n^2} \right) \sim 370 Z^2 \sin^2(\theta_C) \text{ eV}^{-1} \text{ cm}^{-1} \quad (1.6)$$

The spectrum of the Cherenkov radiation is peaked in the UV-blue region of the electromagnetic spectrum, with a maximum around around 330 nm (light blue). The absorption and the scattering processes suffered by the UV component due to the atmosphere significantly modify the observed Cherenkov spectrum, so that it depends on the height of the detection area, the zenith angle of observation and the shower maximum. At sea level, the number of Cherenkov photons emitted per unit length is $n_C \sim 0.1$ photons/cm. Scaling n_C by the path length of the shower and by the total number of particles at the shower maximum, it turns out that the total number of Cherenkov photons is roughly $N_C \sim 10^6$ for 1 TeV gamma ray, where that N_C is proportional to energy of the primary gamma ray [170].

1.3 Imaging Atmospheric Cherenkov Telescopes

The faint Cherenkov radiation reaching the ground can be collected by optical telescopes. IACTs are essentially optical telescopes consisting of large reflectors reflecting the Cherenkov light (*the image*) into an array of PMTs and placed in the focal plane of the mirrors [35].

1.3.1 The imaging of the Cherenkov light

At the detector level the Cherenkov light consists of different components. The first portion of the Cherenkov light ($\sim 25\%$ of the total light) comes from electrons emitting at elevations between the height of the first interaction down to an elevation of 10 km, which correspond to the atmospheric depth of the shower maximum for a typical 1 TeV gamma ray. The Cherenkov angle broadens with decreasing altitude and at 10 km it is of the order of 0.66 deg (12 mrad). On the ground, this results in a blurred Cherenkov ring with radius $R_{light} \approx 10 \text{ km} \cdot 0.012 \text{ rad} = 120 \text{ m}$, the so-called *Cherenkov light pool*. The majority of the light ($\sim 50\%$) comes from a cylinder centered on the shower core and containing the shower maximum. This portion of the light corresponds to the bulk of the Cherenkov radiation and therefore the light from this region is a good measure of the total energy. The remaining 25% of the light is due to local component of the shower, emitted below 6 km. This light is dominated by the few surviving particles and therefore it is subject to large fluctuations. Moreover, the multiple Coulomb scattering suffered by electrons gives rise to an exponential distribution of scattering angles with

respect to the shower axis, with typical angular spread of the order of few degrees [35]. All these effects lead to a rather uniformly illuminated light pool at the ground level.

The imaging of the shower Cherenkov light as performed with an IACT is schematically shown in Fig. 1.6. The telescope is directed towards the putative direction of the gamma ray source. The *camera*, that is the array of PMTs in the focal plane of the mirror, is triggered when a preset number of PMTs detect a light level above a set threshold within a short integration time and correspondingly the Cherenkov light picture of the air shower is recorded. The signal from all pixels is then digitalized and the obtained image allow the characterization of the primary particle originating the EAS. The discrimination against the background is therefore performed on image-bases.

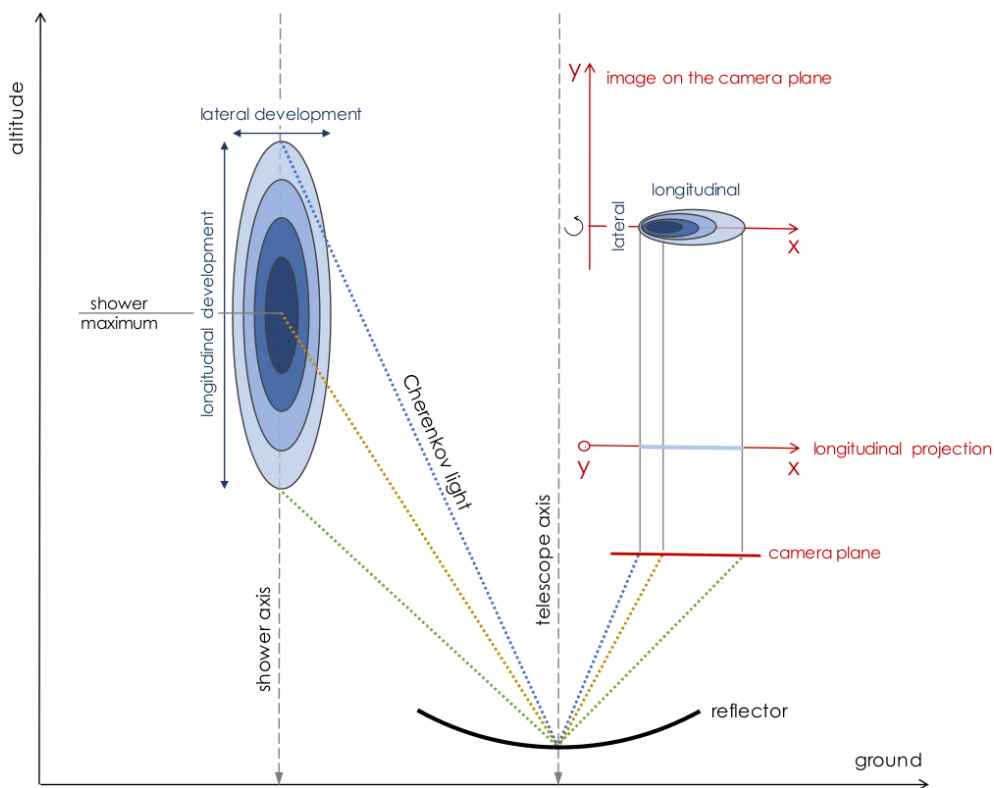


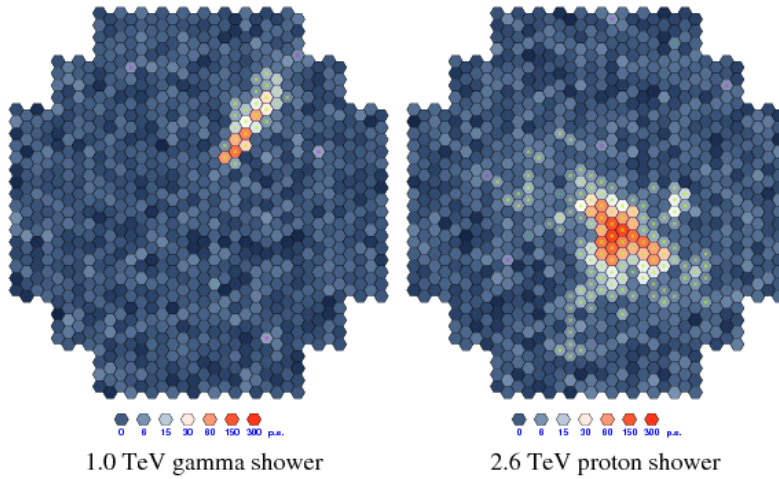
Figure 1.6: Schematic illustration of a shower imaging as performed by a IACT telescope.

1.3.2 Signal and background characterization

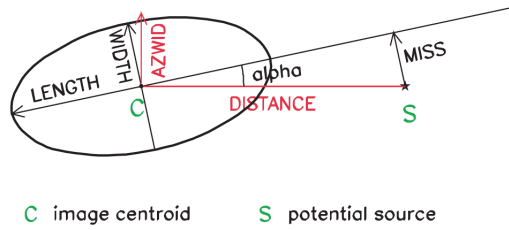
The *image analysis* was suggested by M. Hillas [124], who proposed to characterize the images on the basis of only a few parameters. The aim of Hillas' algorithm was to reject the dominant events from cosmic-ray nuclei by suitable cuts on the images based on Monte Carlo simulations. The assumption is that the regular shape of gamma-ray induced showers is reflected in an image defined by a characteristic comet-like shape with the major axis pointing

towards the source position and long exponential tails which are due to the projection of the longitudinal distribution of the electromagnetic shower (see Fig. 1.7a). In Fig. 1.7b a schematic illustration of the *Hillas parameters* is presented. The idea is that, from the knowledge of the brightness of each pixel, the image can be described by the position of the *image centroid* (the point corresponding to the mean value of the light intensity) and second moments (width and length in Fig. 1.7b) of the (noise-cleaned) light distribution. The analysis of the *width* (the RMS angular size of the minor axis of the ellipse) and of the *length* (the RMS angular size of the major axis of the ellipse), is therefore used to deduce the lateral and the longitudinal development of the shower. The elongation of the ellipse increases as the *impact parameter* gets larger, that is the distance between the telescope and the projection of the shower maximum on the ground. Consequently, also the angular distance of image centroid is increased, and this allows for a reliable reconstruction of the point of origin. The orientation of the shower in the camera system can be quantified by the angle *Alpha*, that is the angle made between the major axis of the ellipse and the line between the source position and centroid, the so-called *distance*. This angle should be very close to zero for showers originating from the source position. Finally, the intensity of the ellipse, i.e. the so-called *size*, gives a measurement for the energy of the primary particle. A very effective single parameter is the azimuthal width, (or *azwidth*), that is the RMS spread of the image measured perpendicular to the line drawn from the source to the centroid. Also this parameter is expected to be small for showers initiated by VHE photons, corresponding to images that are both narrow and approximately aligned with the source [125]. Note that all the projected dimensions of the shower in the image vary with the zenith angle θ . As θ increases, the radius of the Cherenkov light-pool increases by a factor $1/\cos\theta$ and the projected lengths in the image will appear a factor $\sim \cos\theta$ smaller.

This parameterization of the EAS image, together with more complex multi-variate analysis methods (see e.g. [146, 157, 82]), is used to separate gamma-rays and hadrons. The lateral spread and irregularity of cosmic-ray induced showers make these events visible in the camera through an irregularly structured image, as show in Fig. 1.7a. The rejection of the cosmic-ray showers is also done at the trigger level, exploiting the fact that they present a lower Cherenkov light yield with respect to gamma rays. For every neutral pion generating electromagnetic showers through the decay into two photons, $\sim 2/3$ of the initial energy budget is converted into charged pions which in turns produce muons and neutrinos which effectively reduce the available energy for the cascade [35]. Another information that is used to further discriminate electromagnetic showers from hadronic ones is the arrival time of the Cherenkov light. The time spread of the Cherenkov light pulse from the hadronic shower is longer than that from the pure electromagnetic cascade, because of the penetrating particles (and their Cherenkov radiation) which arrive early at the detector level, as for the case of muons. Muons are produced in hadronic showers and usually reach the ground before decaying. Along their path through the atmosphere they emit Cherenkov photons. They do not appreciably suffer multiple scattering and therefore their trajectories are



(a) Imaging of gamma and proton showers.



(b) Hillas parameters.

Figure 1.7: Fig. 1.7a: gamma-ray (on the top-left) and a proton (on the top-right) induced EAS as seen by an IACT. The different shape of the two *images* is used to reject the cosmic-ray background. Extracted from [182]. Fig. 1.7b: the so-called *Hillas parameters*, used to characterize the Cherenkov shower images. Taken from [125].

straight. Consequently, the patter of their Cherenkov light is well described by cones of constant angle, creating rings (or arcs) in the image of the IACT. Muons passing near the telescope are easily suppressed due to the peculiar annular shape. However, very short arcs produced by muons with very large impact parameter look very similar to low energy gamma-ray events. Another source of (virtually irreducible) background is due to cosmic electrons, which produce in atmosphere purely electromagnetic showers. Although electrons are a factor 100 – 1000 times less than the background due to hadronic cosmic rays, their effect is not negligible in the energetic region in which cosmic hadrons are efficiently suppressed (TeV scale). The separation of gamma-ray and electron induced showers in an extremely hard task. Since electron and gamma-ray air showers involve the same interactions in atmosphere, the shape of the parameterized images of both types of electromagnetic showers is practically indistinguishable and the rejection of the electron background can be attempted only by exploiting new variables. Essentially the only useful separation parameter is the depth of shower maximum (X_{max}) which occurs on average half a radiation length higher in the atmosphere for electrons [167, 28].

An additional source of the background is the so-called *night-sky background* (NSB), that is the visible light due to star light, diffuse light from the Galactic plane, zodiacal light, airglow, polar light and artificial light. This is very dependent on the sky region (increases in the Galactic Plane), zenith angle, and moon phase. The NSB photons can mimic low energy gamma-ray events and in order to minimize their contamination at the harder level, very short exposure times (≈ 10 ns) are requested. In fact, the Cherenkov light pulse lasts $\sim 3 - 4$ ns and in principle the detector response should be matched to this short duration. Unfortunately, this represents the main technical limitation for IACTs because camera electronics are required to work at very high speed.

1.3.3 The stereoscopic imaging

Since the beginning of the development of the IACT technique, it was understood that the stereo detection of the showers by multiple telescopes would lead to an improved reconstruction of the arrival direction of the gamma ray and allow a more effective rejection of cosmic-ray EASs. This approach was first demonstrated by the HEGRA collaboration with five small telescopes on La Palma in 1997 [140, 38]. A direct successor to the stereoscopic system of HEGRA Cherenkov telescopes is the H.E.S.S. experiment. Currently, all IACT experiments incorporate this technique (see §1.4 for a description of the current IACT systems).

Multiple images of the same shower offer many advantages. When a system of multiple telescopes observe individual showers, the three-dimensional structure of gamma ray showers can be reconstructed and the determination of shower maximum can be performed in a more accurate way. The direction of gamma rays can be more significantly estimated by taking the intersection point of the major axes of all the elliptically shaped images of multiple telescopes, as illustrated in Fig. 1.8. The angular resolution depends on the num-

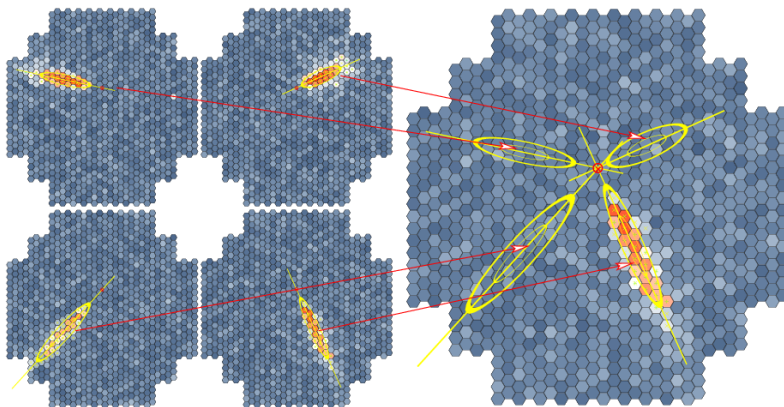


Figure 1.8: Reconstruction of the arrival direction of a gamma ray as performed by a system of IACTs operating in stereoscopic mode. Extracted from [182].

ber N_t of telescopes used in the reconstruction of the event, and up $N_t \sim 50$

it improves as $\propto N_t^{-1/2}$ [128]. The energy threshold of the telescope can be lowered by using a coincident trigger between telescopes. The estimation of the energy of the primary particle is generally a function of the distance of the event from the telescope. With the stereo observation, the determination of the impact parameter is improved and (on average) an higher percentage of the emitted Cherenkov light can be detected, leading to an enhanced energy reconstruction. Also the hadron discrimination benefit greatly from the stereoscopic approach; multiple image characterization permits to better constrain the primary particle, especially in case of local muons with very large impact parameter which mimic low energy gamma rays and can be identified thanks to the different views of the event. The information collected by the cameras of the array allows a 3D parameterization of the reconstructed showers, introducing new variables for the rejection of the background, which exploits the characteristic rotational symmetry (with respect to the incident direction) and the small lateral spread of the electromagnetic showers [146]. The additional three-dimensional parameters, coupled to the image parameters described in §1.3.2, can be used for a background suppression based on a multivariate analysis. Various multivariate classification methods are used nowadays to perform gamma-ray detection analysis with IACT arrays, as the Random Forest (see e.g. [157]), the Neural Network (see e.g. [86]) and the Boost Decision Tree (see e.g. [81, 82]). The classifier output of such multivariate analysis gives a measure of the *hadronness* of the event and allows an improved rejection of cosmic-ray showers.

1.3.4 Technical features of the telescopes

A Cherenkov telescope is primarily characterized by its light collection capability, that is the convolution of its mirror area, its photon collection efficiency and its photon detection efficiency, by its FoV and by its pixel size. The optical system and the electronics for signal collection and triggering are also fundamental aspects in order to match the required conditions on the minimum image size and the short duration of the Cherenkov pulse.

The telescope optics

In order to maximize the collection of Cherenkov photons IACTs exploit large reflectors made of tessellated arrays of individual mirrors. The important parameters of the optical system are: (i) the *point spread function* (PSF), which quantifies how well the reflector concentrates the light from a point-like source and (ii) the time dispersion of the light signal which should not exceed the intrinsic spread of the Cherenkov pulse (~ 3 ns). Different layouts of the optics can be used, each with different properties in terms of time dispersion and imaging quality. In the Davies-Cotton design spherical mirrors of the same focal length are located on an optical support structure with the same radius of curvature as the focal length. This layout provides good off-axis imaging but it introduces a time spread in the time of arrival of the light in the focal plane. In case of a large dish, photons from different part of the reflector travel different

path lengths and this difference broadens the light pulse. This problem with the time dispersion is not present in case of parabolic shaped mirrors and therefore they are preferred in case of large reflectors. A third option is the Schwarzschild-Couder double mirror design [178]. This dual-reflector optics allows large FoV with reduced optical aberration, providing improved imaging at the expense of a more complex structure of the telescope.

The telescope photo-detectors

The photo-sensors used for IACTs are PMTs which convert the hitting photons into a charge pulse. The size of this charge pulse is measured in number of photoelectrons. They are sensitive in the wavelength range of 300-600 nm, with quantum efficiency $\geq 30\%$. The Cherenkov spectrum drops below 300 nm while beyond 550 nm the NSB becomes significant, with typical rates of ~ 10 MHz to more than 100 MHz (depending on the pixel size). Therefore the photo-sensors should match the peak in the Cherenkov spectrum at around 350 nm.

The telescope field of view

Large FoV are especially good since they allow the detection of high energy showers with large impact parameter, avoiding the truncation of the image. Moreover they are desirable for the study of extended sources, diffuse emission and to perform large-scale surveys, for which large FoV help to increase the effective observation time per source compared to instruments which can observe only single sources at a time. The drawback of very large FoV is that, for a given pixel size, the number of photo-sensor pixel and electronics channels grows.

The telescope pixel size

The size of the pixels limit the size of image features that can be resolved with the telescope. Low energy events are dominated by the fluctuations of the NSB and therefore very small pixels (< 0.1 deg) are favored to reduce NSB contamination. On the other hand, for high energy events larger pixels ($\simeq 0.1 - 0.2$ deg) can be used in order to find also a reasonable trade-off with the larger FoV.

1.4 Current IACT instruments

At present, there are three major IACT arrays in operation: H.E.S.S., MAGIC and VERITAS. These instruments consist up to five telescopes (the H.E.S.S. array). They reach sensitivities of $\sim 1\%$ of the Crab Nebula in the energy range from 100 GeV to 1 TeV, with a typical angular resolution of the order of 0.1 deg and energy resolution of 10 – 15% per event. In the following a description of the three arrays is reported.

H.E.S.S.

The High Energy Stereoscopic System (H.E.S.S.) observatory is located in Namibia at 1800 m above sea level (see Fig. 1.9). The initial four H.E.S.S. telescopes (the so-called H.E.S.S. I telescopes) are distributed in form of a square with 120 m side length. Each of these four telescopes is a 12 m diameter class instrument (108 m^2 total mirror area) with Davies-Cotton shape, 5 deg FoV and 960 pixels. In the second phase of the project, a fifth very large telescope was placed at the center of the array. This last telescope, named H.E.S.S. II, is made of a 28 m diameter reflector (614 m^2 total mirror area) with parabolic design, 3.5 deg FoV and a camera containing 2048 pixels. It is operational since July 2012, extending the energy coverage towards lower energies and significantly improving the sensitivity below 300 GeV. H.E.S.S.



Figure 1.9: The H.E.S.S. telescopes, in Namibia. Extracted from the H.E.S.S. website <https://www.mpi-hd.mpg.de/hfm/HESS/>.

is the only IACT array in the Southern Hemisphere and this location allows the observation of one of the most interesting and most populated area in the TeV sky, that is the region of the Galactic center [11, 41]. Moreover, the large FoV of the H.E.S.S. I telescopes (the largest compared to current instruments) permits efficient observations of extended objects and makes it possible to perform an efficient sky survey, as done for the Galactic Plane [100]. A review on the status of the H.E.S.S. telescope can be found in ref. [117].

MAGIC

The Major Atmospheric Gamma Imaging Cherenkov (MAGIC) telescope is located at the Roque de los Muchachos Observatory (La Palma, Spain) at 2200 m above sea level (see Fig. 1.10). It is a system composed by two IACTs of 17 m of diameter (236 m^2 total mirror area) with a parabolic design separated by 85 m. The telescopes have a 3.5 deg FoV and a 576-pixel cameras. The first telescope (MAGIC-I) started to take data in 2004, while the commissioning of second telescope (MAGIC-II) has been finished in autumn 2009.

The two telescopes are usually operated in stereoscopic mode; this provides a significant increase of the sensitivity due to stronger background rejection. Also the energy and angular resolutions have improved, due to the three-dimensional reconstruction of air showers. Given the large reflector surface,



Figure 1.10: The two large telescope of the MAGIC observatory. Extracted from the MAGIC website <https://magic.mpp.mpg.de/>.

the energy threshold of the observatory is notably low, of the order of 30 GeV, traditionally considered the domain of space-based instruments. At this low energies, the Universe becomes progressively more transparent the search of powerful sources residing at large redshifts, e.g. AGNs (see e.g. [156]), is possible. Moreover, a very fast (average time 40 seconds) repositioning of the telescope axis is one of the major characteristic of MAGIC with respect to other IACTs. This is especially important when short-lived phenomena are signaled by other active devices, e.g. GRB alerts from space-based instruments. The reader interested in the latest performance results of the MAGIC telescope is advised to consult ref. [67].

VERITAS

The Very Energetic Radiation Imaging Telescope Array System (VERITAS) is operating at the Fred Lawrence Whipple Observatory (FLWO) in southern Arizona, USA, at 1268 m above sea level (see Fig. 1.11). The array is composed by four 12 m optical reflectors with similar characteristics of H.E.S.S. I, with 499-pixel cameras, with a 3.5 deg FoV. The covered energy range is between 50 GeV to 50 TeV, with peak sensitivity in from 100 GeV to 10 TeV. For a review on the recent results and the status of VERITAS telescope, please refer to ref. [129].

1.5 The Cherenkov Telescope Array

The latest generation of ground-based gamma-ray instruments have demonstrated the great power of the IACT technique to perform imaging and spectrometric studies of VHE gamma-ray sources, pushing this field into a solid branch of the modern astronomy. On the advances pioneered by its predecessors, a next-generation IACT array will be built: the Cherenkov Telescope



Figure 1.11: The VERITAS observatory. Extracted from the VERITAS website <http://veritas.sao.arizona.edu/>.

Array (CTA) [19, 104]. CTA will be the largest and most sensitive ground-based instrument for VHE gamma-ray astronomy on Earth with more than 100 telescopes spread on a huge area and an unprecedented wide energy coverage, from few tens of GeV to more than hundred TeV. Consequently, an extraordinary discovery potential is expected for what concerns key aspects of the astronomy, astrophysics and fundamental physics fields. For the first time in the history of ground-based gamma-ray facilities, CTA will be operated as a proposal-driven open observatory, providing transparent access to data and analysis and visualization tools. Such an observatory-mode operation of CTA is expected to significantly boost its scientific output by engaging a much wider research community. The public release of unique gamma-ray data to the world-wide astronomical and particle physics communities and the synergies with other multi-wavelength and multi-messenger facilities will greatly enhance the significance of the upcoming CTA discoveries.

1.5.1 CTA layout

The optimization of instrument layout is driven by the physics goals. For instance, the studies of AGNs and GRBs require very low energy thresholds to extend the gamma-ray horizon to cosmological distances. On the other hand, for TeV Galactic sources, e.g. SNRs and PWNe, the extension of the energy coverage up to 100 TeV is of prime importance. To cover the full CTA energy range three classes of telescope types will be exploited:

I. Large Size Telescopes (LSTs)

In the *sub-TeV regime* the photon rate is high and the only limitation comes from the systematic uncertainties of the background. Consequently, the area covered by this part of the instrument can be relatively small (of the order of 10^4 m^2). In this energy domain the main target is to lower the energy threshold. Lower energy gamma-rays produce smaller showers and correspondingly less Cherenkov light, which has to be collected efficiently. Therefore, to lower the energy threshold down to tens of GeV and efficiently sample the signal, few large telescopes with mirror area of the order of $\sim 20 \text{ m}$ represent the best solution.

To cover energies up to 100 GeV, CTA will use the so-called *Large Size*

Telescopes (LSTs). LSTs will consist of 23 m diameter parabolic reflective surfaces (400 m² total mirror area), with 4.5 deg FoV and a camera consisting of 1855 pixels. The goal is to be able to re-position the pointing-instrument within 20 seconds, that is the critical aspect for CTA studies of transient phenomena [134].

II. Medium Size Telescopes (MSTs)

The energy range from 100 GeV to about 10 TeV represents the *core* energy of CTA. The detection and the reconstruction of the showers in this energy domain is well known from the current instruments. Therefore, the employment of telescopes similar to those currently in use represents a natural and fruitful solution. These will be the so-called *Medium Size Telescopes* (MSTs), 12 m class telescopes (88 m² total mirror area) distributed on a regular grid with ~ 100 m spacing. MST cameras will have a large FoV of 7 deg, extremely useful in order to rapidly survey the TeV sky. The improvement with respect to previous IACTs is obtained by increased area covered on ground and higher level shower reconstruction, thanks to the multiple views of the event by a larger number of telescopes [25].

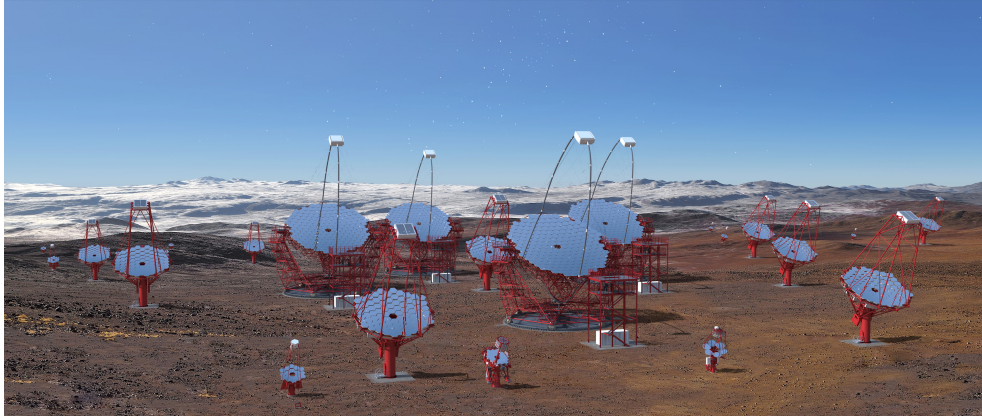
A dual mirror version for this class instruments has been proposed as a high-performance alternative to the baseline MSTs. These telescopes would be Schwarzschild-Couder Telescopes (SCTs), with 7 deg FoV, improved angular resolution and very large number of camera pixels (> 11000) [178].

III. Small Size Telescopes (SSTs)

In the *TeV regime*, the flux level sharply drops due to the typical power-law spectra of non-thermal processes. Therefore, in this energy domain it is necessary to maximize the effective area. Despite the limited number of incoming gamma rays, at this energies the light yield is large and showers can be detected well beyond the typical Cherenkov light pool. For this reason, large number of small telescopes with mirror area of few m² and ~ 400 m spacing represents the best approach for the detection of these rare VHE events.

These telescopes will be so-called CTA *Small Size Telescopes* (SSTs). Three different SST implementations are being proposed and tested: one single-mirror design (SST-1M [123]) and two dual-mirror designs (SST-2M ASTRI [160] and SST-2M GCT [102]). Most probably the array will include a mixture of these designs. The SST mirrors will be about 4 m, with a very large FoV of 9 deg, extremely desirable for deep large-scale surveys above tens of TeV.

In order to view the whole sky, CTA will consist of two arrays of IACTs, one in the Northern and one in the Southern hemisphere, pictured in Fig. 1.12. Together, the two arrays will constitute the CTA Observatory (CTAO). The presence of IACT arrays in both hemispheres, together with the large FoV of the telescopes, will likely enable CTA to provide the first extended gamma-ray map of the entire TeV sky [101], extending the blind exploration of the Uni-



(a) CTA Southern array.



(b) CTA Northern array.

Figure 1.12: Illustrative picture of the future Southern (Fig. 1.12a) and Northern (Fig. 1.12b) arrays of CTA. Extracted from the CTA webpage <https://www.cta-observatory.org/>.

verse beyond the Galactic plane. After years of studies of the environmental conditions, simulations of the science performance and evaluation of the costs, the sites of the two arrays have been decided. The Southern array site will be less than 10 km southeast of the existing Paranal Observatory in the Atacama Desert in Chile (2600 above sea level), while the Northern array will be built in the current MAGIC site, on the island of La Palma, in the Canary Islands (2200 m above sea level).

The Southern array is aimed to observe the central part of the Galactic plane and many nearby Galactic sources. Given the wealth of source populations and morphological details in Southern sky, CTA South will cover the entire energy range of CTA exploiting all three classes of telescopes distributed over a huge area ($\sim 4\text{ km}^2$). In Fig. 1.13 a schematic map of the Southern array is shown, with the planned spacing and numbers of telescopes for each type.

The Northern array is aimed mainly at extragalactic studies, thus the coverage of the highest energies will not be as critical as for the Southern site. It will cover a smaller area on the ground, being optimized for detections in the energy range from tens of GeV to few tens of TeV. No SSTs will be hosted in the Northern array, as summarized in Fig. 1.13.

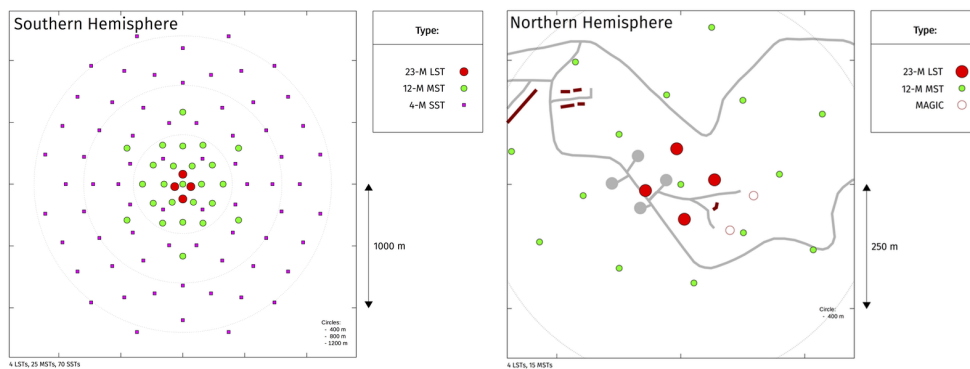


Figure 1.13: Planned layout for the Southern (left) and Northern (right) array of CTA. Different size and color circles are for different type of telescopes. Extracted from the CTA webpage <https://www.cta-observatory.org/>.

1.5.2 CTA performance

The improvements expected for CTA are targeted to achieve specific performance goals. In the following a summary on the expected CTA performance is reported.

- **Angular resolution**

Above 1 TeV, the CTA angular resolution should achieve values as good as 2 arcmin, that is a factor ~ 3 better with respect to the typical resolution of current instruments. This will allow to resolve the details of complex morphologies of extended sources and will definitely help observations of densely populated sky region.

- **Effective area**

As previously mentioned, the CTA Southern array will be distributed over an area of the order of $\sim 4 \text{ km}^2$. This huge detection area is a crucial parameter in order to perform observations of VHE phenomena in the nearby non-thermal Universe, for which the corresponding VHE photons do not suffer severe gamma-ray absorption.

- **Energy resolution**

The wide energy coverage of CTA (more than 3 orders of magnitude in energy) will come together with an unprecedented energy resolution, which above 1 TeV should achieve the level of $\sim 6\%$, corresponding to a factor 2 improvement with respect to the current IACT facilities.

- **Temporal resolution**

Thanks to its large detection area, CTA will resolve flaring and time-variable emission on sub-minute scales [19]. These time-scales are currently not accessible: the shortest time variability detected so far by the present instruments is of the order of few minutes, in correspondence to flaring AGNs (see e.g. [63]).

- **Sensitivity**

In its core energy, CTA is required to achieve milli-Crab sensitivity in 50

hours of observation on a point-like source, slightly worsening towards lower energies, due to poorer background rejection efficiency, and towards higher energies, due to the limited number of gamma rays. This corresponds to a factor 10 improvement with respect to the sensitivity of the current instruments. This achievement would allow both the detailed study of known objects and the serendipitous discovery of several faint objects currently below the potential of existing observatories.

1.5.3 Science with CTA

The superior capabilities of CTA will significantly impact on several areas of modern astrophysics and cosmology. Besides the detection of new classes of gamma-ray emitters and new phenomena, CTA will allow a deep understanding of already known objects and mechanisms [19]. The main science goals of CTA can be summarized in three main themes, reported in the following. For a deeper description on the source populations and on the mechanisms at play in astrophysical environments, the reader is encouraged to look at §A and §B.

1. Understanding the origin of Galactic and extragalactic cosmic rays and their role in the Universe. The most accepted scenario explains Galactic cosmic rays as due to acceleration processes in SNRs and hints in favor of such paradigm have been found both by Fermi and AGILE with the detection of the characteristic π^0 -bump [3, 174, 22]. CTA should be able to detect a large population of SNRs emitting VHE photons and, among them, special expectations are reserved to the search for PeVatrons, which is a key issue for understanding of the origin of galactic cosmic rays. Moreover, present instruments have proved that the interaction of cosmic rays with interstellar gas produce a measurable gamma-ray flux. The detection of these VHE photons from other galaxies can be used by CTA to infer the role of cosmic rays in processes of star formation [17].
2. Understanding the nature of particle acceleration and radiation processes in extreme astrophysical environments. In particular, the study of relativistic outflows, as the jets related to accreting black holes, and ultra-relativistic cold winds, related to pulsars, would allow detailed tests of magnetohydrodynamics and plasma physics on scales that are not accessible with laboratory experiments. CTA should detect a large sample of AGNs with SMBHs at their center, which offer excellent conditions for particle accelerations in shocks [169].
3. Searching for the nature of Dark Matter and physics beyond the Standard Model. Dark matter in the form of WIMPs should be detectable by CTA through their annihilation process and the corresponding production of VHE photons. The wide energy coverage of CTA will allow the detection of possible low mass WIMP candidates and the improved energy resolution will increase the chance to resolve spectral features and lines characteristic of WIMPs. In addition, the enhanced performance

of CTA might enable the investigation of other questions related to the fundamental physics, as the search for axions-like particles or the test of the Lorentz invariance [101].

These three core themes serve as science drivers and to address these points the CTA Collaboration has investigated a number of key projects to be carried out by the Consortium. One of the prime science targets for CTA will be the region of the *Galactic Center*, probably the most densely populated region in the gamma-ray sky and therefore a prime object for the search of dark matter annihilation signature [101]. The improved angular resolution of CTA should allow a deeper understanding about the nature of the bright TeV source positionally coincident with the SMBH Sgr A*. Moreover, the wide energy coverage up to hundreds of TeVs, the large FoV and the improved energy resolution of CTA will permit accurate spectroscopic and morphological studies of the diffuse emission from the extended region of the Galactic Center ridge, extremely interesting in the context of PeVatron study.

Another key project of CTA is the *survey of the Galactic plane*. CTA should be able to carry out an unbiased exploration of the Galactic plane region ($|l| \leq 60$ deg, $|b| \leq 2$ deg) with a uniform sensitivity of 3 milli-Crab, giving access to hundreds of new sources in the broad CTA energy range (mainly PWN and SNRs) along with new and unexpected gamma-ray sources [104]. This will permit the first high statistics population studies, tracing discrete sources as well as diffuse emission meanwhile facing the problem of source confusion which unavoidably will show up in the crowded regions of the Galactic plane. Moreover, thanks to the large FoV and the improved sensitivity, CTA should be able to survey the $\sim 25\%$ of the sky at high galactic latitudes ($b > 10$ deg) down to sensitivity of 20 milli-Crab, performing for the first time a blind search beyond the Galactic plane. This *extragalactic survey* would complement the survey done by Fermi at lower energies [18] and would lead to the detection of about a dozen blazars, or counterparts to Fermi sources [104], as well as to the serendipitous detection of transient phenomena. The measure of such *transient phenomena* represents another key goal of CTA. Thanks to the low energy threshold and the fast re-positioning of the telescopes, CTA should be able to measure for the first time the VHE variability from GRBs [133] as well as the transient emission from PWN and/or binary systems flaring up [159, 96].

The significant increase of sensitivity of CTA will open the way to statistical studies of AGNs [169]. This, combined with the broad energy coverage and the high spectral resolution of CTA, will help to rule out AGN models and constrain the scenario for the explanation of their VHE emission. Moreover, the excellent angular resolution of CTA should permit to resolve the extended emission surrounding the central compact object, that is unavoidably produced due to interactions of primary gamma-rays with the EBL [151]. The detection of this faint halo emission would provide cosmological information about the intergalactic radiation and magnetic fields, representing an extremely attractive detection in the context of *extragalactic source* studies.

A diffuse extended emission is expected also from *Galaxy clusters*, due to

the possible presence of cosmic rays interacting with the cluster gas and subsequently producing VHE gamma rays through pion decays. A direct evidence for the existence of these cosmic protons in clusters does not exist yet and therefore gamma rays would represent an unambiguous proof [17]. The improved performance of CTA should enable the detection of diffuse gamma-ray emission from nearest galaxy clusters, like Perseus and Coma, which is also an interesting target for dark matter search due to its large mass [101].

2

Morphological studies

Since its conception in 2005, CTA has made considerable progress: working prototypes exist for all telescope types but the large size ones (which is under construction already as part of the Northern observatory), in few years the operations should begin and the end of array construction is foreseen for 2024. Although the general design of the observatory is already defined, the final layout of the array is still under discussion. In this chapter the CTA observatory is used as a template for the description of a generic IACT array. With simple analysis methods, questions of primary importance for planning future observations are addressed. The importance of such questions lies in the aim to draw general conclusions independently of the specific instrument details, since at this stage absolute results might not be meaningful given the possible changes in the final layout design of CTA. With these ultimate goals, the potential of the array to perform morphological studies of gamma-ray sources in complex environments at the presence of multiple TeV emitters is estimated. In §2.3, simulations of isolated point-like and extended sources are described and used to test and understand the response of the instrument. Then, in §2.4, the capability of the instrument to resolve multiple sources has been analyzed. In particular, the effect of locating the gamma-ray source (i) nearby a second one and (ii) on top of a diffuse halo-type object is investigated.

2.1 Instrument response parameterization

Given the wealth and the variety of VHE TeV emitters in the Southern sky, in this thesis the South array of CTA is considered. In order to cover the broad energy range of CTA, the idea is to have an array formed by a total of 4 LSTs, a few tens of MSTs and about 70 SSTs. One of the proposed layout for the Southern observatory, the so-called *2-Q* layout, consists of 4 LSTs (23 meter class, FoV of the order of 4.5 deg), 24 MSTs (12 meter class, FoV of 7 deg) and 72 SSTs (4 meter class, FoV ranging from 9.1 to 9.6 deg). For such an array, publicly available instrument response functions (IRFs) have been released by the CTA Consortium¹, obtained through a large-scale Monte Carlo (MC) production (the so-called *Prod-2*) aimed to study the impact of the site on the CTA performance and to search for feasible layout candidates [121].

¹The CTA performance files can be accessed at <https://www.cta-observatory.org/science/cta-performance/>.

The evaluation of the array performance is based on analysis tools similar to those currently used by existing IACTs. Simulations of a point-like gamma-ray source located at the center of the FoV and observed at a zenith angle of 20 deg (averaged between north/south-wise in azimuth) are performed together with simulations of background showers (protons, nuclei and electrons). The response of the telescope to these EASs is then simulated. The analyses applied to the simulated events are classical ones, based on parametrized shower images. Merging together the information from all the telescopes observing the event, the stereo reconstruction is performed and the background suppressed. In this way, the performance of the array is estimated, expressed by the IRFs.

In this work, these publicly available IRFs for the $2-Q$ array layout have been exploited to obtain simple analytical parameterizations in the energy range from 50 GeV to 100 TeV. In particular, an analytical expression for the angular resolution, the effective area, the energy resolution and background rate per unit of solid angle have been derived, as reported in the following. In table 2.1 the average values of these analytical functions are shown for four main energy intervals.

Table 2.1: The angular resolution (σ_{PSF}), effective area (A_{eff}) and background rate per square degree ($BgRate$) in the four energy intervals.

Energy	σ_{PSF} [deg]	A_{eff} [m ²]	$BgRate$ [Hz/deg ²]
[0.05 – 0.1] TeV	0.147	$4.1 \cdot 10^4$	$9.69 \cdot 10^{-1}$
[0.1 – 1] TeV	0.083	$2.4 \cdot 10^5$	$1.53 \cdot 10^{-1}$
[1 – 10] TeV	0.042	$1.66 \cdot 10^6$	$3.20 \cdot 10^{-3}$
[10 – 100] TeV	0.031	$3.73 \cdot 10^6$	$3.55 \cdot 10^{-5}$

2.1.1 Angular resolution

The determination of the direction of the incoming gamma ray is of crucial importance for a pointing detector which can be operated in survey mode. As described in §1.3.3, the stereoscopic approach allows for a good reconstruction of the arrival direction of primary gamma rays on an event-by-event basis. In the CTA IRFs here considered, the shower direction is determined by a weighted mean of all pairwise intersections of the major axes of two images, where the weight assigned to each pair depends of the size of the two images, on their orientation and on their width over length ratio, as described in ref. [86]. The reconstructed shower direction corresponds to the weighted average of all intersection points. The high telescope multiplicity of CTA will permit an accurate estimate of the shower direction and will definitely lead to an improved angular resolution of the instrument.

The angular resolution is defined as the angular radius that contains a certain percentage of the gamma-ray PSF. The expected CTA angular resolution (σ_{PSF}) is shown in Fig. 2.1 as a function of the energy. Assuming

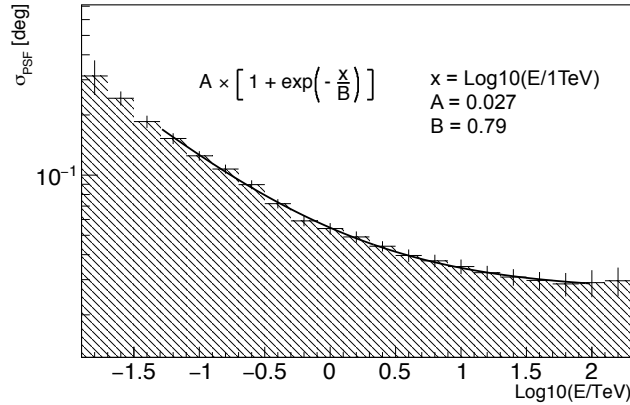


Figure 2.1: Angular resolution of the instrument. The data are taken from the publicly available CTA performance files ¹, solid line corresponds to the best fit. The corresponding analytical function is also shown in the plot.

$x = \log_{10}(E/1 \text{ TeV})$, σ_{PSF} can be approximated in the form:

$$\sigma_{PSF}(x) = A \cdot \left[1 + \exp\left(-\frac{x}{B}\right) \right] \quad (2.1)$$

with $A = 2.71 \cdot 10^{-2}$ deg representing the best angular resolution achievable with the telescope layout considered in this work and $B = 7.90 \cdot 10^{-1}$ the scaling factor describing how fast the angular resolution changes with energy. In general, also the location of the source within the FoV might modify the value of σ_{PSF} . For CTA, this effect is expected to be negligible for energies lower than ~ 10 TeV, with almost no dependence of σ_{PSF} with the source offset up to 3° , and a smooth degradation (by a factor < 2) up to 4° at the higher energies [171]. Nevertheless, this dependence on the source position does not affect the physics scenarios here investigated, being characterized by geometrical extensions below the threshold limits for which a significant effect is expected (see §2.2 for further details).

For morphological studies the shape of the PSF is a key issue. To first approximation the PSF shape can be described by a two-dimensional Gaussian distribution:

$$f_{PSF} = \exp\left(\frac{x^2 + y^2}{2\sigma_{PSF}^2}\right) \quad (2.2)$$

For a wide variety of telescopes operating in different energy bands of the electromagnetic spectrum, in addition to the central Gaussian component, the PSF might contain tails extending well away from the peak. To account for the presence of such tails and to study their impact on the resolution of weak gamma-ray sources, a non-Gaussian shaped PSF has been assumed. Namely, following ref. [42], the PSF is presented in the form²:

$$f_{PSF} = \exp\left(\frac{x^2 + y^2}{2\sigma_{PSF}^2}\right) + K \cdot \exp\left(\frac{x^2 + y^2}{2\sigma_{PSFtails}^2}\right) \quad (2.3)$$

²Note that to compare the PSF as presented in Eq. [2.3] with the one-dimensional PSF reported in ref. [42], one has to scale σ_{PSF} as well as $\sigma_{PSFtails}$ by a factor 1.51 in order to retrieve the same percentage of containment.

The tails of the non-Gaussian PSF are described by a second Gaussian func-

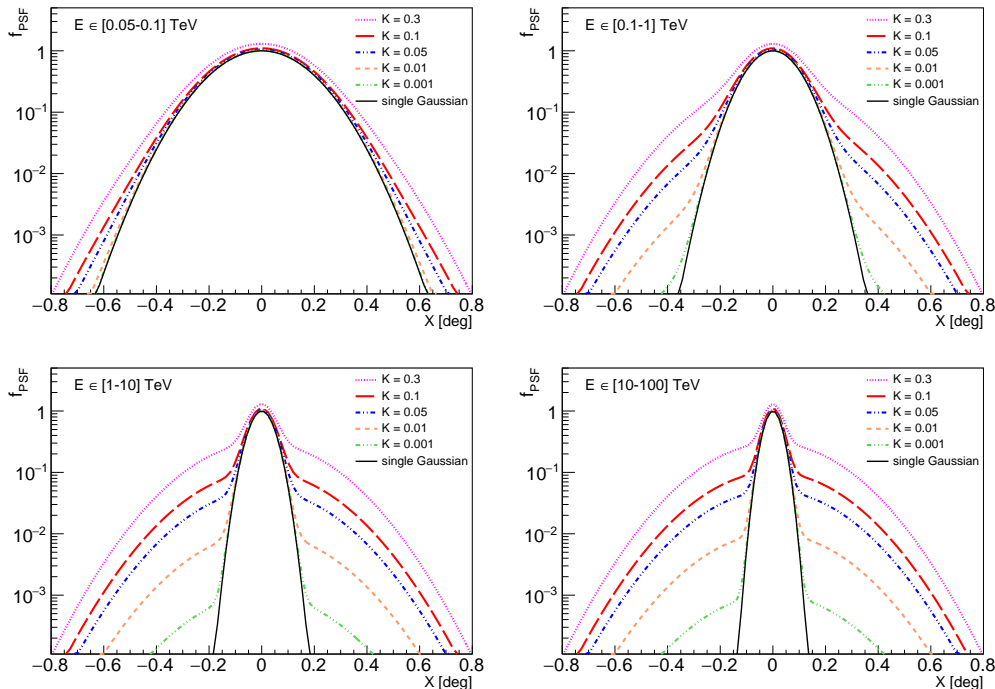


Figure 2.2: Possible shapes of the PSF in four energy intervals: 0.05 – 0.1 TeV, 0.1 – 1 TeV, 1 – 10 TeV and 10 – 100 TeV. Black curves correspond to the ideal case of simple Gaussian PSF, described by Eq. [2.2]. Colored dashed curves are for the more realistic non-Gaussian PSF with tails, described by Eq. [2.3] for five different values of the parameter K (see the text).

tion having a width $\sigma_{PSFtails}$, fixed to the fiducial value of 0.2 deg (assuming a worst case scenario) in the whole energy range. The ratio K of the normalization factor of the main and the secondary Gaussian was adjusted to describe the effects of different tails, namely, the values considered are: 0.3, 0.1, 0.05, 0.01 and 0.001. In Fig. 2.2 the PSFs corresponding to these values are shown in four energy intervals: 0.05 – 0.1 TeV, 0.1 – 1 TeV, 1 – 10 TeV and 10 – 100 TeV. The black curve is for the case of single Gaussian PSF, described by Eq. [2.2], while the colored dashed curves are for the non-Gaussian PSF with tails described by Eq. [2.3]. The more significant the contribution of the tails, i.e. the larger the parameter K , the stronger the modification of the PSF shape with respect to the ideal Gaussian case. Moreover, the value of σ_{PSF} improves with energy (see Fig. 2.1), resulting in a more dramatic alteration when adding $\sigma_{PSFtails}$ to the description of the PSF shape at the higher energies. It is important to highlight that the use of the H.E.S.S. modeling for the non-Gaussian PSF, as reported in ref. [42], has to be considered here as a conservative upper limit. With tens of telescopes, the CTA observatory is expected to do better and this especially concerns the observations at the high energies, i.e. $E \geq 10$ TeV. In fact, although a constant value of $\sigma_{PSFtails}$ is assumed in this work by virtue of the H.E.S.S. results, a reduction of the tails size is likely to take place as the energy increases, due to the larger tele-

scope multiplicity which should reduce the PSF fluctuations responsible for the tails. The energy dependence of the PSF tails is beyond the goals of this work. Nevertheless, detailed MC studies aimed to explore the effect of the tails on the instrument performance and their relevance in different energy domains might represent an extremely important task for the upcoming CTA observatory.

2.1.2 Effective Area

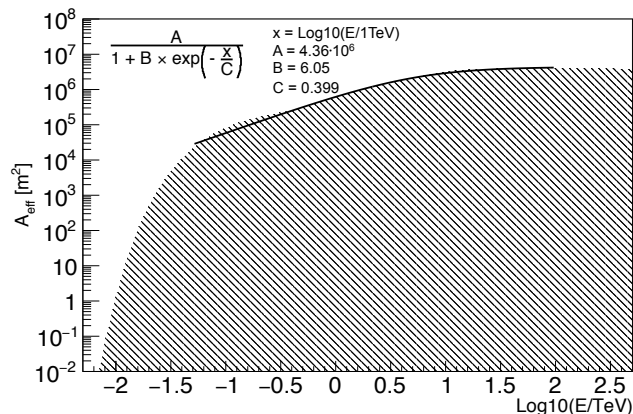


Figure 2.3: Effective area of the telescope layout considered in this study. The data are taken from publicly available calculations of the CTA performance ¹, solid lines correspond to the parametrization formula which is also shown in the figure.

In the Southern CTA array, the telescopes are planned to be distributed over $\sim 4 \text{ km}^2$ on the ground. While for a single telescope the effective area is determined by the radius of the Cherenkov light pool at ground ($R_{light} \sim 120 \text{ m}$), the effective detection area of a multi-telescope system is determined essentially by the total geometrical area [47], as can be seen in Fig. 2.3. For the considered layout of the CTA South observatory, the effective detection area A_{eff} in the energy range from 50 GeV to 100 TeV can be parametrized with the following expression:

$$A_{eff}(x) = \frac{A}{1 + B \cdot \exp\left(-\frac{x}{C}\right)} \quad (2.4)$$

where the saturation value of the effective area is $A = 4.36 \cdot 10^6 \text{ m}^2$, while $B = 6.05$ and $C = 3.99 \cdot 10^{-1}$ define the rate of change of A_{eff} with respect to energy.

2.1.3 Energy resolution

The energy resolution is a figure of merit used to summarize in a single number the information contained in the energy dispersion parameterization. The energy resolution of the instrument, referring to the public CTA MC results,

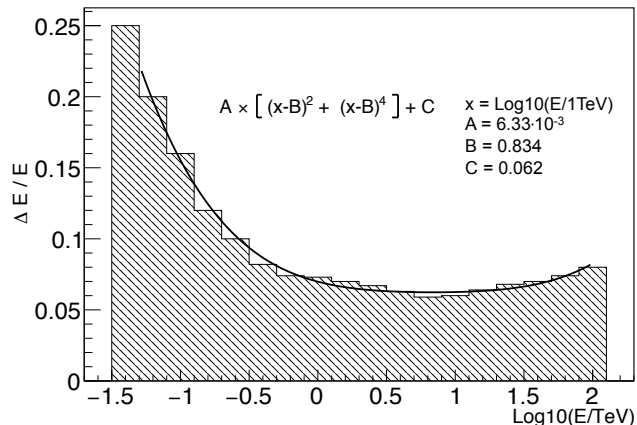


Figure 2.4: Energy resolution for the considered layout of CTA southern array. The data are taken from publicly available calculations of the CTA performance ¹. The solid line corresponds to the analytical parametrization which is also shown in the figure.

is shown in Fig. 2.4. Although energy resolution is rather modest in the low energy range (approximately 20% around 50 GeV), it significantly improves at higher energies saturating at the level of 6 to 8% from 1 TeV to 100 TeV. The energy dependence of the resolution can be parametrized in the following form:

$$(\Delta E/E)(x) = A \times [(x - B)^2 + (x - B)^4] + C \quad (2.5)$$

with the normalization factor A taking the value $A = 6.33 \cdot 10^{-3}$, the parameter $B = 8.34 \cdot 10^{-1}$ fixing the value of the energy for which the resolution takes its best value and $C = 6.24 \cdot 10^{-2}$ representing the best energy resolution achievable with the telescope layout considered in this work.

2.1.4 Background rate

The simulated rate of background events after all the rejection cuts is shown in Fig. 2.5 as function of the energy. Simulations of cosmic-ray background events were performed by the CTA Consortium assuming power-law spectra for all cosmic-ray particles with the exception of the electrons and positrons, described by a log-normal peak on top of an $E^{-3.21}$ power-law spectrum. For the background events initiated by protons and heavier nuclei, an $E^{-\alpha}$ dependence has been adopted, with α ranging from 2.70 (for protons) to 2.63 (for iron), based on measurements performed by BESS [168], Pamela [27], Fermi [20] and other experiments [188, 85]. The noise from the NSB and from electronics is added as well. The NSB corresponds to dark sky observations, i.e. no moon light, and a sky region off the Galactic Plane (the average level of NSB corresponding to dark sky observation is 0.121 photo-electrons/ns/pixel for a MST) [86]. On the simulated background showers, selection cuts are then applied in order to suppress events not induced by gamma rays (see e.g. [121]). For the surviving events, the energy dependence of the overall background rate

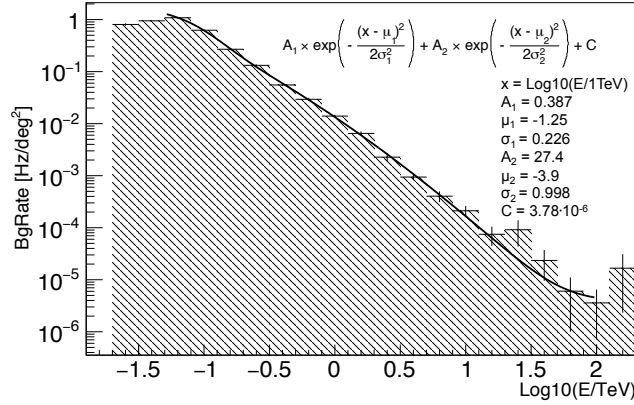


Figure 2.5: Background rate per unit of solid angle. The data are taken from publicly available calculations of the CTA performance ¹. The solid line corresponds to the parametrization formula which is also shown in the figure.

per unit of solid angle can be approximated to the following form:

$$BgRate(x) = A_1 \cdot \exp\left(-\frac{(x - \mu_1)^2}{2 \cdot \sigma_1^2}\right) + A_2 \cdot \exp\left(-\frac{(x - \mu_2)^2}{2\sigma_2^2}\right) + C \quad (2.6)$$

with $A_1 = 3.87 \cdot 10^{-1}$ Hz/deg², $\mu_1 = -1.25$, $\sigma_1 = 2.26 \cdot 10^{-1}$, $A_2 = 27.4$ Hz/deg², $\mu_2 = -3.90$, $\sigma_2 = 9.98 \cdot 10^{-1}$ and $C = 3.78 \cdot 10^{-6}$ Hz/deg².

For each energy interval, we computed the mean number of spurious events N_{BgRate} scaling the rate $BgRate$ by the observation time and by the angular area. In order to take into account fluctuations in the background, we randomly sampled the number of background events N_B from a Poissonian distribution: $f(N_B | \lambda) = (\lambda^{N_B} e^{-\lambda}) / N_B!$, with expected value $\lambda = N_{BgRate}$.

2.2 Methodology

For simulating the source, an excess map of $3^\circ \times 3^\circ$ with pixel size of 0.03° was created. The map was filled with signal S and background B events according to the definition of *excess* used by Li & Ma (formula 2 in in ref. [148]): the content of each pixel of the map was fixed by the relation $N_S = N_{on} - \alpha N_{off}$, where $N_{on} = S + B$ and $N_{off} = B/\alpha$, α being the ratio of the on-source integration time (or region) to the off-source integration time (or region). In this study, three *off* regions have been used for the estimation of the background, therefore $\alpha = 1/3$. The background events were uniformly distributed in the map, whereas for the gamma-ray source a Gaussian shape was assumed:

$$f(x, y) = A \cdot \exp\left(-\left(\frac{(x - X_0)^2}{2\sigma_{src}^2}\right) + \left(\frac{(y - Y_0)^2}{2\sigma_{src}^2}\right)\right) \quad (2.7)$$

centered on the point $(X_0, Y_0) = (0, 0)$ deg (the center of the FoV) and characterized by the size σ_{src} for which three different scenarios have been investigated, shown in Fig. 2.6:

- $\sigma_{src} = 0.03$ deg; this is smaller than the PSF in any energy band, therefore the source can be considered a good approximation of a point-like source;
- $\sigma_{src} = 0.1$ deg; this is comparable to the PSF, therefore the source can be considered as a moderately extended source;
- $\sigma_{src} = 0.2$ deg; this is larger than the PSF (~ 2 times), therefore the source can be considered as an extended source.

The normalization factor A in Eq. [2.7] takes into account the flux strength of the source. The following form for the gamma-ray flux has been considered:

$$\frac{dN}{dE} = k \cdot I_0 \times \left(\frac{E}{1 \text{ TeV}} \right)^{-\alpha} \quad (2.8)$$

with $\alpha = 2.62$ which corresponds to the Crab power-law photon index as measured by HEGRA [38]. The flux is normalized at 1 TeV at the value $k \cdot I_0$, where $I_0 = 2.8 \cdot 10^{-11} \text{ TeV}^{-1} \text{ cm}^{-2} \text{ s}^{-1}$ is value of the Crab flux at 1 TeV [38] and k fixes the number of Crab Units (C.U.) to define the flux strength of the object. For each energy interval and for each source size, the energy integrated flux has been uniformly spread all over the source extension. This means that for a certain flux strength (or percent of the Crab flux), the more extended the object the smaller its photon density, as illustrated in Fig. 2.6.

In order to account for the statistical fluctuations in the simulation of the excess maps and consequently in the estimation of the morphological parameters of the source, tens of realizations of the simulation were performed, which represents a good compromise between a reliable sampling of the errors (i.e. errors are Gaussian distributed) and the computational time. Each simulated excess map has been fitted with a solid χ^2 -minimization approach in order to get an estimation of the source parameters. The results shown in the following correspond to the average values over the tens of realizations.

2.3 Isolated source

Simulations of isolated sources are performed and used as a benchmark to test the instrument performance for different observation modes. First the event rates and the background regimes are investigated. Then the morphological reconstruction of the isolated source, aimed to estimate its center of gravity and its angular size, is evaluated assuming both Gaussian (Eq. [2.2]) and non-Gaussian PSFs (Eq. [2.3]).

2.3.1 Event rates and background regimes

In Fig. 2.7 the rates for signal S and for background B events, as well as the ratio S/B , are shown for different flux strengths of the source and different source sizes. The rates S and B are derived as expected from a *region of*

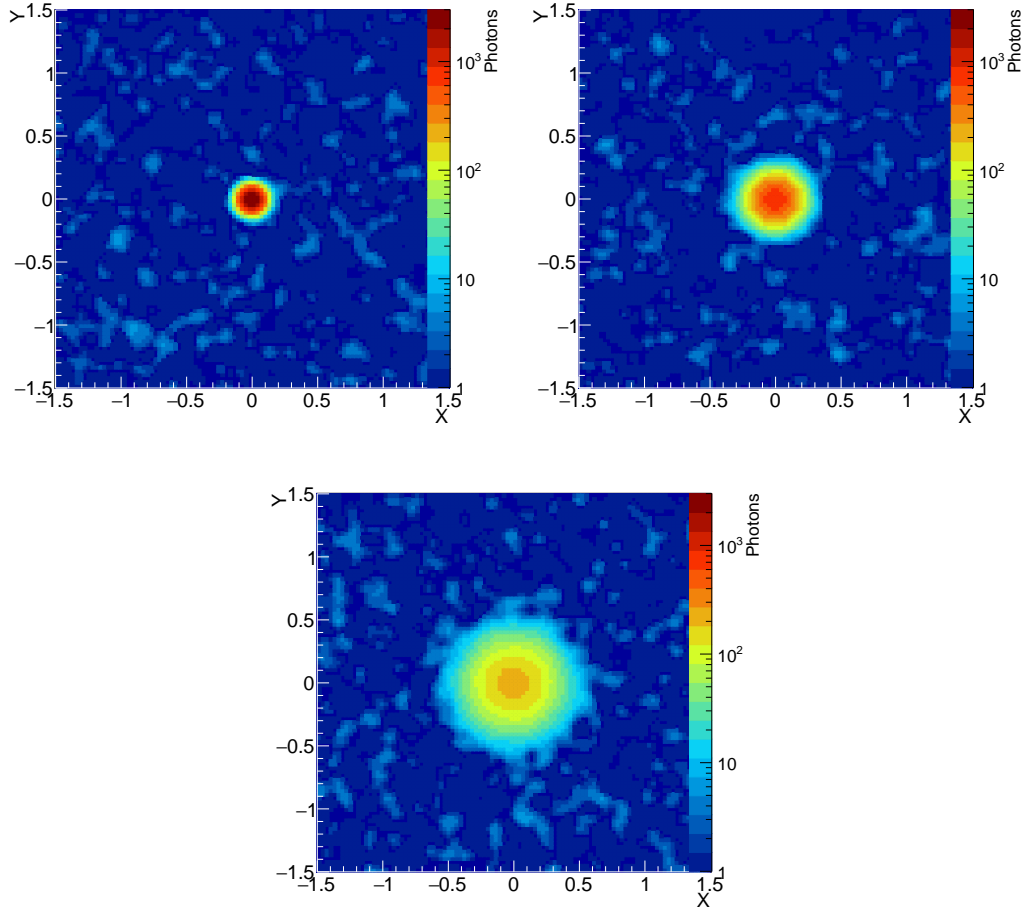


Figure 2.6: Examples of excess count maps for the three source sizes considered in this work: $\sigma_{src} = 0.03$ deg (top-left), $\sigma_{src} = 0.1$ deg (top-right) and $\sigma_{src} = 0.2$ deg (bottom). The shape of the gamma-ray object is described by Eq. [2.7] and its spectrum is given by Eq. [2.8]. The background is randomized according to a Poisson distribution and uniformly distributed in the map (see §2.1.4 for the details on the background simulation). In these plots, 50 hours observation time is assumed and energies from 1 TeV to 10 TeV are considered, where the telescope is expected to achieve the best performance in terms of sensitivity [25]. The flux strength of the object is 0.1 C.U. Note that the energy integrated flux is uniformly spread all over the source extension.

interest (ROI) defined as a circle centered on the center of the source and having radius:

$$R_{ROI} = \sqrt{(2\sigma_{src})^2 + (2\sigma_{PSF})^2} \quad (2.9)$$

which in the case of point-like objects is reduced to $R_{ROI} = 2\sigma_{PSF}$. On the upper horizontal axis of each plot the corresponding flux levels for an E^{-2} power-law spectrum are shown in units of Crab at 1 TeV. Although the source regions have been filled with the same number of events for each assumed flux strength, and the flux is uniformly spread all over the source extension, in the low energy intervals the signal rate S slightly differs depending on the source size. This is due to the larger σ_{PSF} at these energies, which spreads out events on a larger scale, pushing events that belong to the tails of the source distribution to fall outside the ROI. When $S/B < 1$, the detection proceeds in the *background dominated* regime. On the other hand, for larger values of the S/B ratio the *background free* regime is achieved. In table 2.2, the threshold values of the flux strength for which the condition $S/B = 1$ is reached are shown in the four energy intervals for each source size. Since the integrated flux in the region comprised by sources of different size is normalized to the same value (or percent of the Crab flux), while the background events are uniformly distributed in the map regardless the actual size of the object, to achieve the $S/B = 1$ condition, the larger the source size the higher the required flux intensity.

Table 2.2: The flux strengths in Crab Units (C.U.) for which the condition $S/B = 1$ is reached for different source sizes in four energy intervals.

Energy	$\sigma_{src} = 0.03$ deg	$\sigma_{src} = 0.1$ deg	$\sigma_{src} = 0.2$ deg
[0.05 – 0.1] TeV	0.3 C.U.	0.5 C.U.	1 C.U.
[0.1 – 1] TeV	0.006 C.U.	0.03 C.U.	0.1 C.U.
[1 – 10] TeV	< 0.001 C.U.	0.004 C.U.	0.01 C.U.
[10 – 100] TeV	< 0.001 C.U.	0.004 C.U.	0.01 C.U.

2.3.2 Signal-to-noise

Not only the absolute statistics of signal events has to be considered when claiming for a source detection. The significance of the measure needs to be reported in order to ascertain the reliability of the result from a statistical point of view. An indicator of such a significance is the *signal-to-noise ratio*, defined as:

$$\frac{S}{N} = \frac{S}{\sqrt{\delta S^2 + \delta B^2}} = \frac{S}{\sqrt{S + B}} = \frac{T \cdot R_S}{\sqrt{T \cdot R_S + T \cdot R_B}} \quad (2.10)$$

assuming a Poissonian statistics for the number of signal (S) and background (B) events in the ROI and, in the last step, writing the equation in terms of event detection rates (R_S and R_B) and observation time (T). For a given observation time, it is clear that when $R_B \gg R_S$ then $S/N \propto R_S$, while when $R_B \ll R_S$ then $S/N \propto \sqrt{R_S}$. Given the direct relation between signal

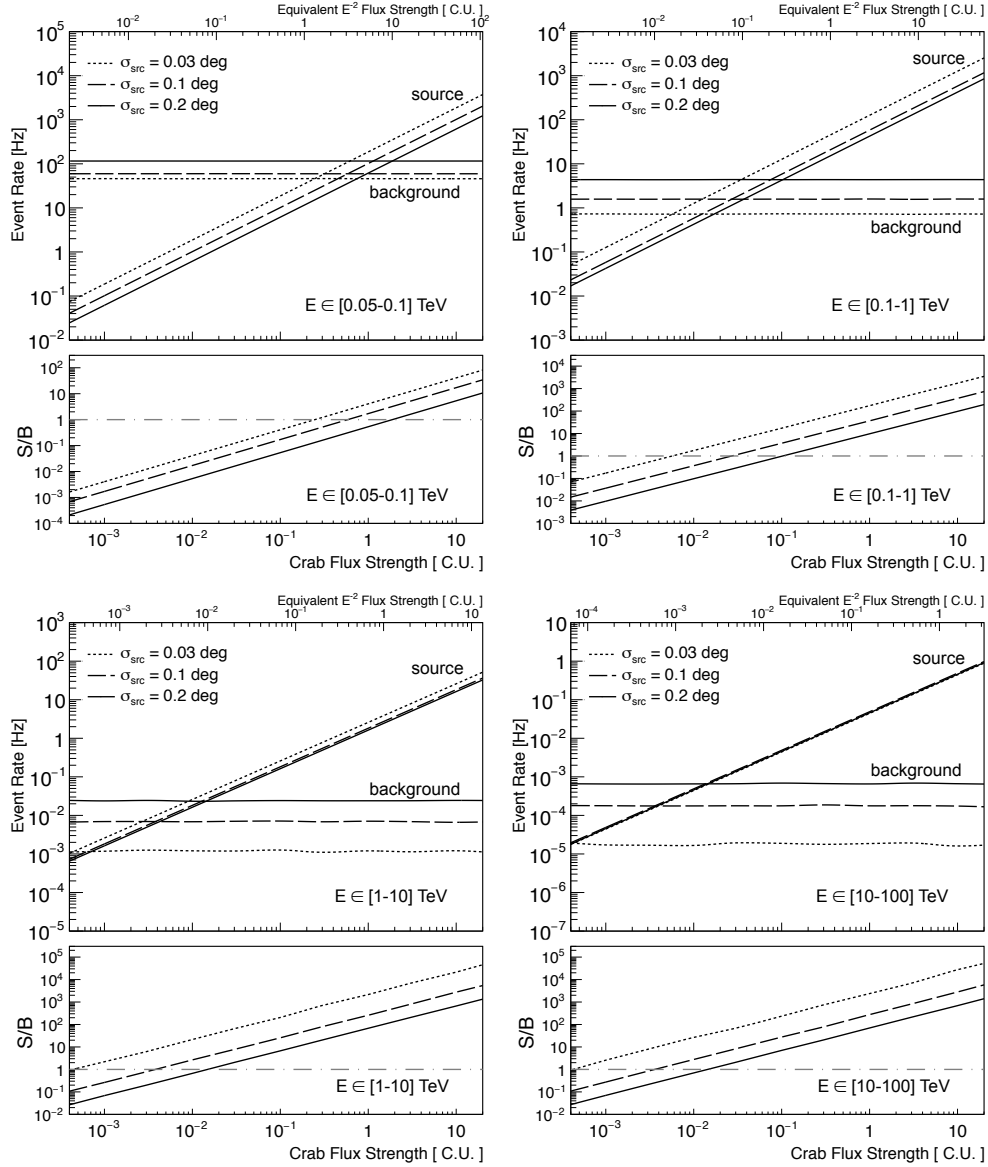


Figure 2.7: Event rates for background events (*background*, B) and signal events (*source*, S). The ratio of the two (S/B) is also shown at the bottom of each panel; the gray dashed-dotted line is for $S/B = 1$. The four panels are for the four different energy ranges, which are shown in each figure. The three sets of curves correspond to three sizes of the source: 0.03 deg (dotted lines), 0.1 deg (dashed lines) and 0.2 deg (solid lines). Depending on the source size, the event rates are calculated in correspondence to different ROI (Eq. [2.9]).

detection rate and flux intensity of the gamma-ray source, a linear dependence of S/N as a function of the flux strength is expected in the background dominated regime, and a square root dependence when the signal dominates on the background. This kind of behavior can be appreciated in Fig. 2.8, where the S/N distributions have been fitted with the following two functions: $f_1(x) = p_0 + p_1 \cdot \sqrt{x}$ (dotted lines) and $f_2(x) = p_0 + p_1 \cdot x$ (solid lines). Different curves are for different energy domains. The higher the energy con-

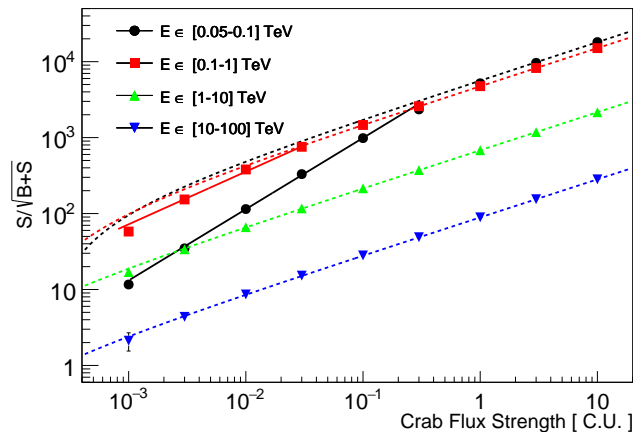


Figure 2.8: Signal-to-noise ratio distribution as a function of the flux of the point-like source, expressed in units of Crab flux at 1 TeV. Four different energy domains are shown. Dashed lines are for the fit with the function $f_1(x) = p_0 + p_1 \cdot \sqrt{x}$, solid lines represents the best fit to the data when the linear function $f_2(x) = p_0 + p_1 \cdot x$ is used. Data are for an observation time of 50 hours. The χ^2/NDF of the fit with the second degree polynomial function are the following: 144552 for [0.05 – 0.1] TeV, 1248 for [0.1 – 1] TeV, 11 for [1 – 10] TeV and 0.4 for [10 – 100] TeV.

sidered, the sooner the signal dominates over the background and therefore the better the function f_1 fits the data, as can be appreciated from the value of the χ^2/NDF ratio of the fit reported in the caption of the figure for each energy domain. On the other hand, at the low energies a deviation from the function f_1 is established when the source is not bright enough and the linear function f_2 better reproduces the distribution. Furthermore, the lower the energy, the higher the value of the flux at which the deviation can be observed, due to the fact that at the low energies the $R_B \gg R_S$ condition is better satisfied and the background dominated regime holds.

2.3.3 Reconstruction of morphological parameters for Gaussian PSF response

The reconstructed image of the source is altered by the noise from the sky and by the intrinsic limiting factors of the detector. Therefore the reconstruction of its features, like its size and its gravity center, is a challenging issue for every morphological study one aims to perform. In order to reconstruct the morphology of the gamma-ray source, the Gaussian-shaped object has been

convolved with the instrument PSF, initially assumed to be described also by a Gaussian function (Eq. [2.2]). The resulting function used to fit the reconstructed excess map is the following:

$$f(x, y) = A \cdot \exp\left(-\left(\frac{(x - X_0)^2}{2(\sigma_{src}^2 + \sigma_{PSF}^2)}\right) + \left(\frac{(y - Y_0)^2}{2(\sigma_{src}^2 + \sigma_{PSF}^2)}\right)\right) \quad (2.11)$$

where σ_{PSF} depends on the energy interval. Treating σ_{PSF} as a fixed parameter, the source size σ_{src} and of its center of gravity (X_0, Y_0) have been estimated through the χ^2 fit.

The skymaps have been simulated for different exposure times and then the minimum time needed to properly reconstruct the morphology of the source has been estimated. This is defined as the minimum time such that (i) the relative error on the reconstructed morphological parameter (either the center of gravity or the source size) is reduced to at least 1% and (ii) the mean value of the estimated parameter is not more than 3σ away from the simulated one. In addition to these criteria, a minimum of 10 signal photons on the source region is required.

In Fig. 2.9 the minimum time needed to reconstruct the center of gravity is shown as a function of the flux strength in four energy intervals³. The gravity center is the point with largest density of photons, i.e. the reconstructed position of the source in the map. The estimation of the parameters X_0 and Y_0 is used to reconstruct the gravity center as $\sqrt{X_0^2 + Y_0^2}$. One can see that the shortest minimum time is required in the energy domains [0.1 – 1] TeV and [1 – 10] TeV, where the best instrument performance is achieved. At very low ([50 – 100] GeV) and very high ([10 – 100] TeV) energies the required time is significantly increased because of the large background rate and low photon statistics, respectively. For instance, for a point-like object with a flux strength of 0.1 C.U., few hours of observation are sufficient to reconstruct the position of the source in the two central energy ranges. Below 0.1 TeV or above 10 TeV, the same object has to be observed for tens of hours in order to achieve the same level of reconstruction accuracy. One should also note that the minimum time required to reconstruct the source position is always larger for extended sources than for point-like sources. The reason being that the flux is normalized to the source size and therefore the photon density is lower than in the case of point sources. The same tendency is observed for the minimum time needed to estimate the source size. The results are shown in Fig. 2.10.

2.3.4 Reconstruction of morphological parameters for non-Gaussian PSF response

As discussed in §2.1.1, the ideal approximation of a Gaussian PSF might not be confirmed by reality and in a more realistic approach tails should to be

³Note that for the shorter observation times the results should be taken with caution since the analytical parameterizations shown in §2.1 are obtained from the CTA simulations optimized for 50 hours observation time.

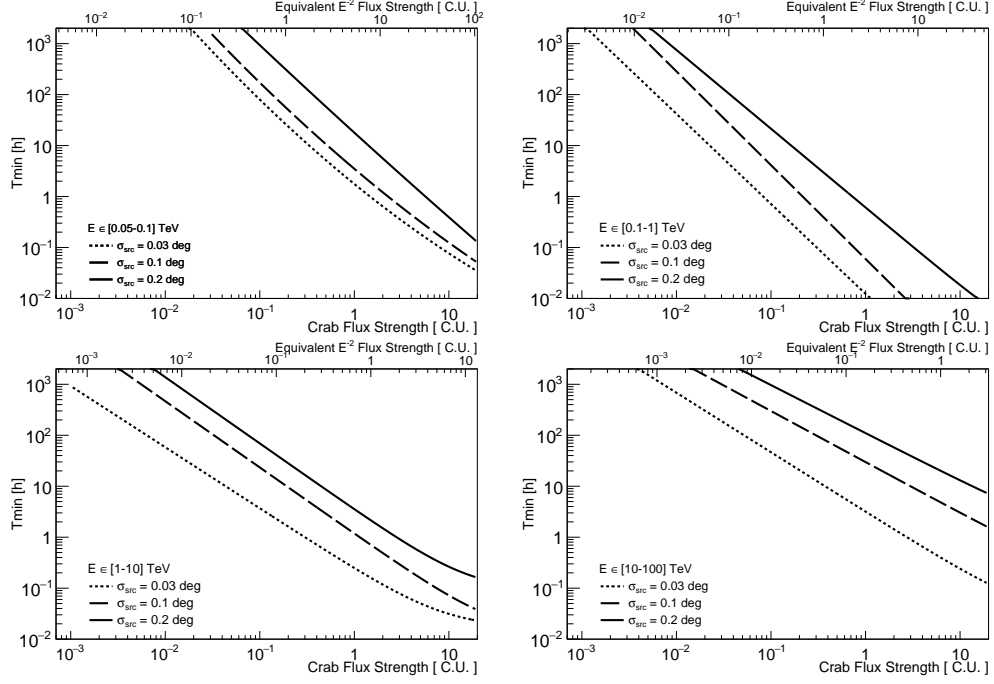


Figure 2.9: Minimum time needed to reconstruct the center of gravity of the source in the case of Gaussian PSF response and for four energy intervals: $[0.05 - 0.1]$ TeV, $[0.1 - 1]$ TeV, $[1 - 10]$ TeV and $[10 - 100]$ TeV.

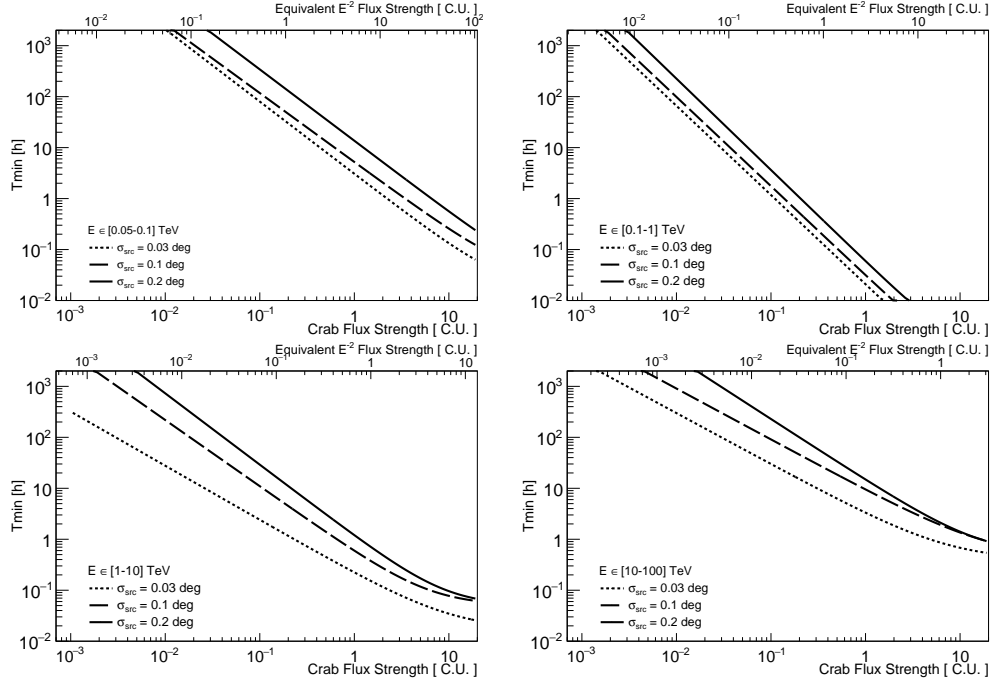


Figure 2.10: Minimum time needed to reconstruct the size of the source as a function of the gamma-ray flux in the case of Gaussian PSF response and for four energy intervals: $[0.05 - 0.1]$ TeV, $[0.1 - 1]$ TeV, $[1 - 10]$ TeV and $[10 - 100]$ TeV.

included. The influence of these tails in the reconstruction of source morphology has been investigated. Simulations of the excess maps have been carried out under the assumption of a non-Gaussian PSF with tails, as defined in Eq. [2.3]. Then, the gamma-ray source is reconstructed using Eq. [2.11] to investigate the effect of tails on the morphological reconstruction when these are not properly evaluated.

The results are summarized in Fig. 2.11, where the reconstructed size of the source is shown as a function of the flux strength for different values of the parameter K in Eq. [2.3]. The errors quantify the spread of the results, estimated as the root mean square deviation over the sample of tens of realizations of the simulation. The grey solid line at 0.1 deg indicates the input size value used in the simulation.

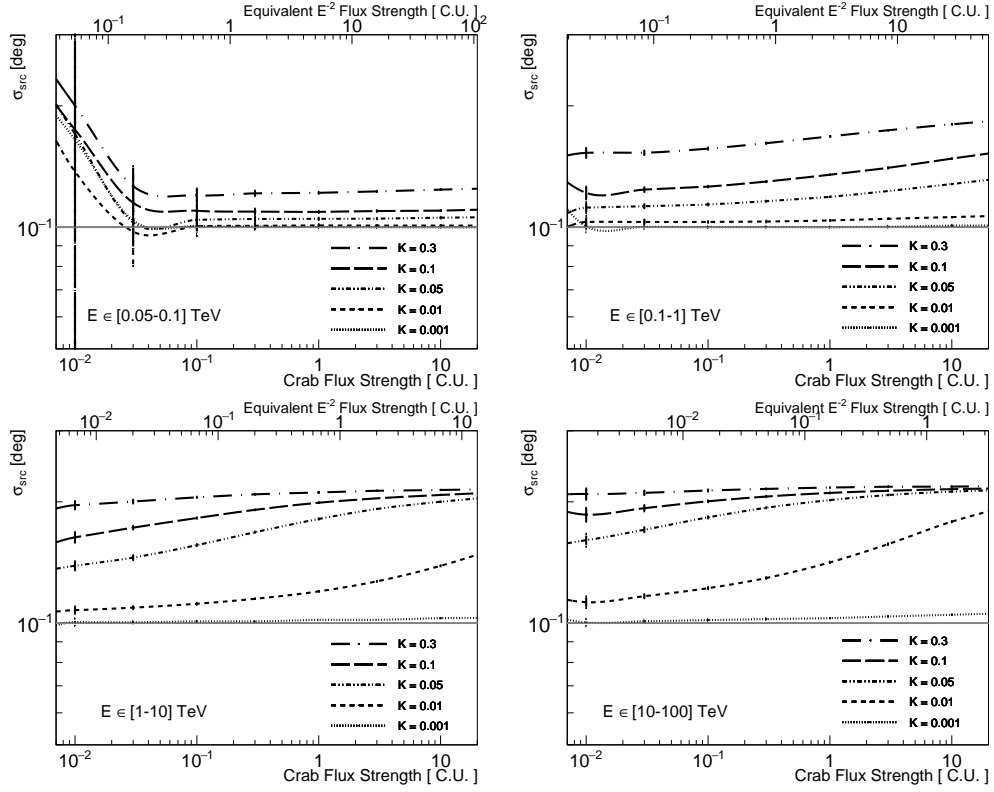


Figure 2.11: Reconstructed size of the source as a function of the flux strength for different values of the parameter K which defines the PSF shape composed with superposition of two Gaussians. The input value for the source size is indicated as a solid gray line, $\sigma_{src} = 0.1$ deg. The observation time is 50 hours. Four energy intervals are shown: $[0.05 - 0.1]$ TeV, $[0.1 - 1]$ TeV, $[1 - 10]$ TeV and $[10 - 100]$ TeV.

In the lowest energy domain ($[0.05, 0.1]$ TeV), where the background dominates, the results for sources with fluxes ≤ 0.1 C.U. are strongly affected by fluctuations. For brighter sources a proper estimation of the size can be done when the ratio K is in the 0.01 to 0.001 range. In this energy interval σ_{PSF} is almost of the same order of the $\sigma_{PSFtails}$, i.e. $\sigma_{PSF} = 0.147$ deg and $\sigma_{PSFtails} = 0.2$ deg. This results in a relatively small effect of the tails for

small K values, since the final shape of the PSF does not differ much from the simple Gaussian model, as shown in Fig. 2.2. Nevertheless, when K is very large ($K \sim 0.3$), the PSF cannot be described as a single Gaussian and the effect of the wider distribution prevents a proper reconstruction of the real size of the source.

The value of σ_{PSF} improves with energy (see Fig. 2.1), resulting in a more dramatic effect when adding $\sigma_{PSFtails}$ to the description of the PSF shape. In the high energy intervals, the reconstruction of σ_{src} is strongly affected by the tails and what is reconstructed is essentially $\sigma_{PSFtails} = 0.2$ deg. The results in Fig. 2.11 shows that the larger the ratio K , the sooner in terms of flux a deviation from the expected value takes place, especially when the tail contributions amounts to at least 5% of the peak value.

2.4 Multiple sources

On the basis of the simulations of isolated objects, the response of the telescope has been tested also in case of complex environments. The capability to reconstruct the source morphology might be compromised in case of crowded environments, where a not trivial distribution of the sources might limit the instrument performance. The potential of the instrument to disentangle multiple objects has been evaluated assuming both the Gaussian and the non-Gaussian shape of the PSF. Two different scenarios are studied in this section: (i) the case of two nearby objects (see Fig. 2.12, on the left), which represent a key issue when planning observation of the Galactic plane region and (ii) the case of a compact source on top of an diffuse halo-type emission (see Fig. 2.12, on the right), which might be relevant in the framework of extended extragalactic sources surrounding AGNs.

2.4.1 Two nearby sources

The chance to observe two TeV emitters in the same FoV is non negligible when the instrument points toward the region of the Galactic plane (see §B.1 for an overview on the Galactic sources). The question of resolvability of nearby gamma-ray sources is a critical aspect for future instruments since the improved sensitivity will allow for the detection of very faint objects, increasing the probability to catch multiple sources in a single observation. Two nearby gamma-ray objects have been simulated considering different separation distances between the two bodies. Each of the two objects is described as a Gaussian-shaped source (Eq. [2.7]) while the background is uniformly distributed in the map. As for the isolated objects, the Crab-like spectrum defined in Eq. [2.8] is assumed. An example of the two companion gamma-ray sources is reported in Fig. 2.12.

The centers of gravity of the two sources have been estimated through a joint χ^2 -fitting analysis and from the reconstructed positions the distance between the two sources has been calculated. In Fig. 2.13 the reconstructed distances, d_{rec} , between the two sources is shown for different combinations of

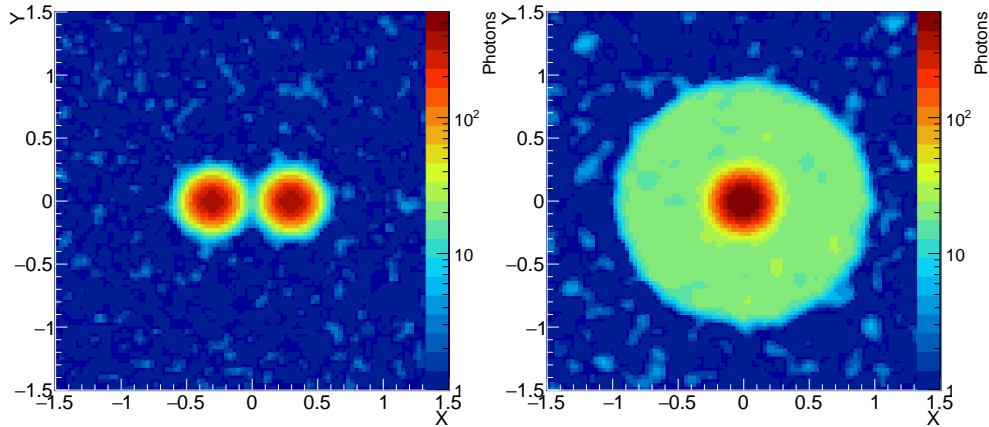


Figure 2.12: Left: example of an excess count map in the case of two nearby objects. The shape of the two gamma-ray objects is described by Eq. [2.7] (calculated for $\sigma_{src1} = \sigma_{src2} = 0.1$ deg) and their spectrum is given by Eq. [2.8], here fixed at a flux strength of 0.1 C.U. Right: example of an excess count map in the case of a compact source on top of an diffuse halo-type emission. The central object is again described by Eq. [2.7] ($\sigma_{src} = 0.1$ deg) and its spectrum is given by Eq. [2.8] (kept at 0.1 C.U.). The extended halo is simulated according to Eq. [2.12] (further details are given in the following). In both the two maps, 50 hours observation time is assumed and energies from 1 TeV to 10 TeV are considered, for which the telescope is expected to achieve the best performance in terms of sensitivity [25]. Note that the energy integrated flux is uniformly spread all over the source extension, regardless the specific spacial distribution of the object.

their flux strengths. These results are obtained with the assumption of a Gaussian PSF and are referred to the CTA core energies, i.e. from 1 TeV to 10 TeV, where the best sensitivity of the instrument is expected to be achieved [121]. The true distance, d_{true} , is shown on top of each plot, ranging from 0.2 deg to 0.5 deg. Obviously, the larger the distance the better the reconstruction. For small separations, the distance is well estimated only when the fluxes of the two sources are similar. Otherwise the reconstruction fails, leading to a null separation, since the weakest source turns out to be hidden by the companion and only the strongest of the two objects is visible.

These studies have been done also under the assumption of a non-Gaussian PSF. Eq. [2.3] has been calculated for $K = 0.3$ which represents the worst scenario in terms of effects induced by the tails in the PSF model. The fake emission from the tails adds to the gamma emission of the sources. For separations in the range of those shown in Fig. 2.13, the distance is always estimated as zero, since the presence of the tails does not allow anymore to resolve the two sources. The effect of the tails disappears only when the distance between the two sources is large enough ($d \geq 0.7$ deg). In Fig. 2.14 the reconstructed distance between the two sources, placed at distances ranging from 0.7 deg to 1.4 deg, is shown. To disentangle the two sources a minimum distance of

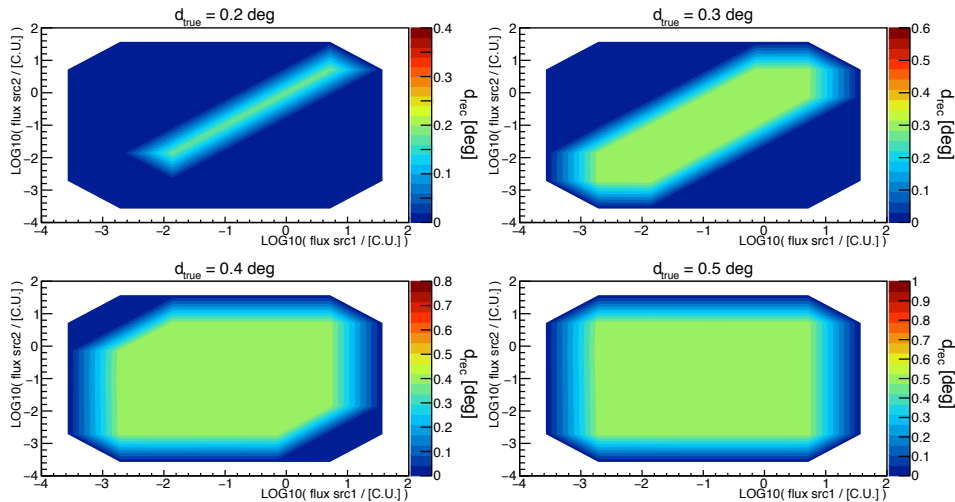


Figure 2.13: Reconstructed distance (d_{rec}) between two nearby sources (named src1 and src2 in the plots) for different combinations of the flux strengths of the two objects. The Gaussian shape of the two sources is defined by Eq. [2.7], calculated for $\sigma_{src1} = \sigma_{src2} = 0.1$ deg. The true distances used in the simulation, d_{true} , are shown on the top of each distribution, ranging from 0.2 deg to 0.5 deg. The energy interval is from 1 TeV to 10 TeV and the Gaussian PSF is assumed (Eq. [2.2]). The exposure time is 50 hours.

~ 0.8 deg is required.

2.4.2 Compact source on a diffuse, halo-type, extended source

The problem of separating multiple objects might arise also in case of a compact source on top of a diffuse halo-type object, as expected in correspondence of AGNs. The measured VHE gamma-ray emission from AGNs is produced in the very compact region around the central black hole; nevertheless, an extended component of radiation is expected to be created around the central source, due to interaction of primary TeV photons with the EBL (see §A.2 for a description on the mechanisms that lead to the creation of the extended halo and §B.2 for the an overview on AGNs). The detection of a faint halo in VHE gamma rays on top of the strong central object is a quite hard task and it can be further complicated by the presence of tails in the PSF.

In this section the effect of locating a compact central source on an extended halo is investigated. Simulations have been performed assuming a Gaussian spatial distribution for the central source, defined by Eq. [2.7], and exploiting the following function to describe the diffuse halo:

$$f(x, y) = A \cdot \frac{1}{2} \cdot \left(\tanh \left(\frac{r + R_{halo}}{\delta} \right) - \tanh \left(\frac{r - R_{halo}}{\delta} \right) \right) \quad (2.12)$$

with $r = \sqrt{(x - X_0)^2 + (y - Y_0)^2}$. This hyperbolic tangent function is a smooth approximation of a 2D circular Heaviside function and δ is a parameter that roughly controls the thickness of smooth transition zone. Here $\delta \rightarrow 0$

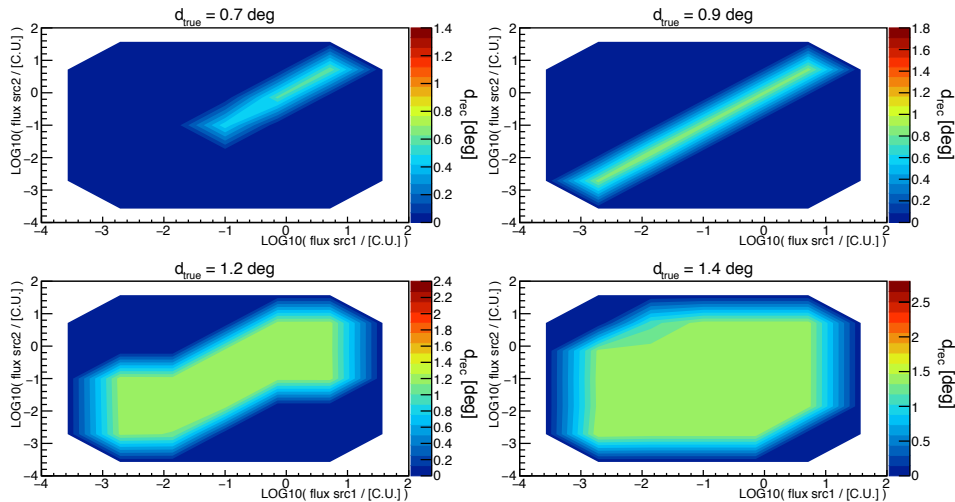


Figure 2.14: Same as in Fig. 2.13 but for the case of a non-Gaussian PSF with tails, calculated for $K = 0.3$ (Eq. [2.3]). The true distances used in the simulation, ranging from 0.7 deg to 1.4 deg, are shown on the top of each distribution.

is assumed. The halo has been centered at $(X_0, Y_0) = (0, 0)$ deg and its radius R_{halo} defined as:

$$R_{halo} = \sigma_{src} + m \cdot \sigma_{PSF} \quad (2.13)$$

with σ_{src} being the size of the central source, assumed to be a 0.1 deg size object, and m the multiplicative factor of the energy dependent σ_{PSF} (Eq. [2.1]) taking the values: 1, 2, 5, 10 and 30. The factor A in Eq. [2.12] defines the intensity of the halo flux, expressed in units of the flux strength of the central bright source which is kept at 0.1 C.U. The spectrum in Eq. [2.8] is used for the two objects and the energy integrated flux is uniformly spread all over the extension of the sources. An example of this scenario is shown in Fig. 2.12.

The two sources are efficiently separated when both the halo and the central source are individually well reconstructed. In Fig. 2.15 the reconstructed angular size of the central source (on the top) and the reconstructed radius of the halo (on the bottom) are shown as a function of the halo flux strength. The Gaussian PSF is assumed and the energy range from 1 to 10 TeV is considered, where the average value of the angular resolution is $\sigma_{PSF} = 0.042$ deg.

When the flux level of the halo is small enough, i.e. $\leq 10\%$ of the central source flux, the weak emission from the halo doesn't compromise the observation of the central source and the reconstruction of the angular size of the compact object is well performed, regardless the actual size of the halo. On the other hand, when the two fluxes start to be of the same of magnitude, the reconstructed σ_{src} is not properly estimated: for $R_{halo} > 2\sigma_{src}$ the central source size is overestimated due to the additional emission from the halo in the region surrounding the central object⁴. Otherwise, when the halo emission

⁴Note that the central object is defined by Eq. [2.7] and therefore the 95% of its spatial distribution is comprised in 2 standard deviations from the peak value, i.e. $2\sigma_{src}$.

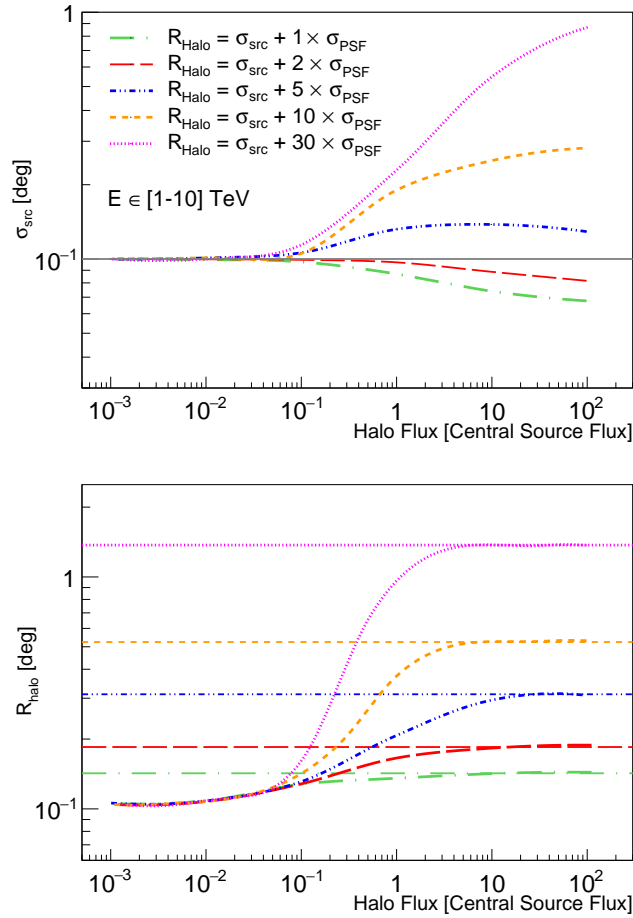


Figure 2.15: Top: reconstructed angular size of the central source as a function of the halo flux, which is expressed as a fraction of the compact object flux and kept at 0.1 C.U. The solid line is for the real value of the source size, *i.e.* $\sigma_{src} = 0.1$ deg. Different curves are for different values of the halo radius. Bottom: reconstructed radius of the halo as a function of the halo flux. The horizontal lines indicate the expected values; different line styles are for the different input radius used in the simulation and listed in the legend on the left. The energy range considered here is from 1 to 10 TeV where $\sigma_{PSF} = 0.042$ deg and the best sensitivity of the instrument is expected. The observation time is 50 hours and the Gaussian PSF is assumed (Eq. [2.2]).

is limited in space ($R_{halo} < 2\sigma_{src}$), the reconstructed source size is underestimated, due to the high photon density induced by the halo emission in the inner region of the compact object.

Inversely, for what concerns the reconstruction of the halo radius, the estimation of R_{halo} saturates to a threshold value roughly given by σ_{src} in case of faint halo emission. In this configuration, the strong emission from the central object at 0.1 C.U. prevents the isolation of the diffuse halo and makes the reconstruction of the halo morphology unreliable. When the halo flux is of the same order of the central source flux, a proper estimation of the halo structure is achieved. Given the assumption of a 0.1 C.U. central

source, the requirement on the halo brightness translates into an halo flux of the same order of magnitude. This result is in agreement with upper limits set by existing IACT arrays on the flux of the extended emission expected to be formed around detected AGNs: the no detection of halo-like structures around known extragalactic compact objects implies halo fluxes at the level of (or even weaker) a few per cent of the Crab Nebula flux [10, 59, 108], making the detection of such a diffuse emission challenging also for future IACT instrument, thus requiring more sophisticated analysis for the extraction of its faint signal.

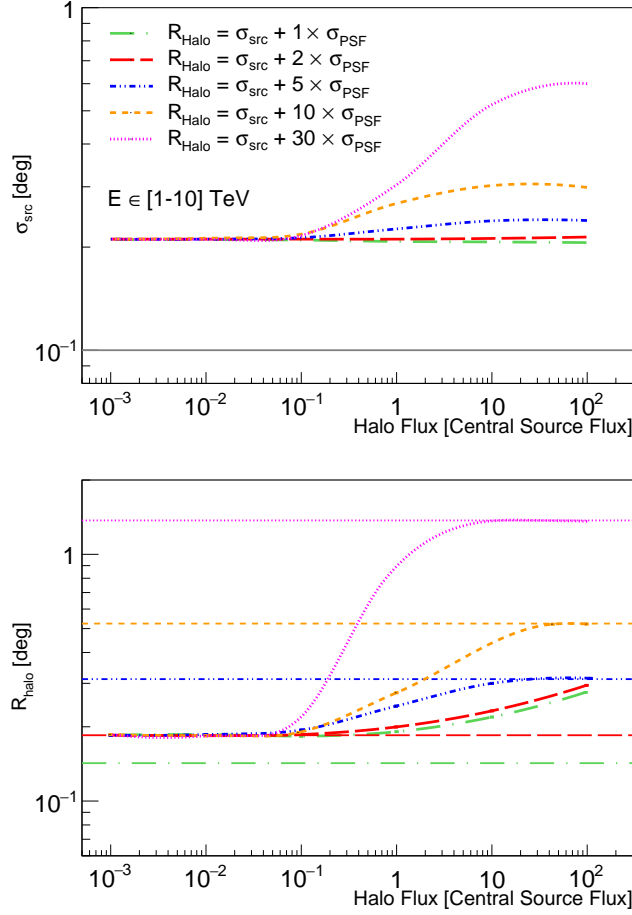


Figure 2.16: Same as in fig. 2.15 but in the case of a non-Gaussian PSF with tails defined by eq. 2.3 and calculated for $K = 0.3$. Note that the simulated size of the tails is $\sigma_{PSFtails} = 0.2$ deg.

In Fig. 2.16 the same study is shown for the non-Gaussian PSF response. As expected, the reconstructed σ_{src} is limited by the tails of the PSF ($\sigma_{PSFtails} = 0.2$ deg) which represents the minimum size one can aim to reconstruct. As a consequence, a proper reconstruction of the source morphology is not achievable, even for very faint halos. Moreover, when the flux strength of the halo is $\geq 10\%$ of the central source flux, σ_{src} is further overestimated: the more extended the halo, the more significant the overestimation of σ_{src} , since the bright emission from the halo adds to the fake emission from

the tails and to the central source emission itself. Similarly, in case of weak halos the estimated radius is a constant value ($\sim \sigma_{PSFtails}$). The only way to ensure a proper reconstruction of the halo morphology in case of tails in the PSF is to look at extended objects ($R_{halo} > \sigma_{PSFtails}$) brighter than the central compact source.

3

Sensitivity studies

As described in §1.5, CTA foresees to improve the sensitivity of current ground-based high-energy gamma-ray instruments by an order of magnitude. This factor concerns the observations of a single point-like object, isolated from any other source. However, this physical scenario is not easily guaranteed when performing real observations, especially in the case of very high energy phenomena in our Galaxy. For Galactic objects, the probability to find more than one source in the same FoV is very likely. Moreover, most of the gamma-ray emitters lying in the Galactic plane are better described as extended objects rather than point-like sources. Starting from these considerations, an estimation of the expected CTA sensitivity is presented in this chapter (i) in the case of a not isolated point-like source, i.e. at the presence of a nearby TeV emitter (see §3.2), and (ii) in the case of an extended gamma-ray source (see §3.3).

3.1 Methodology

The sensitivity of the instrument is defined as the minimum flux for which a significant detection can be performed. In order to characterize the level of significance of the gamma-ray signal detection, a set of criteria has to be defined. The CTA recipe for the computation of the differential sensitivity curve exploits the following requirements for each energy bin [86]:

1. at least 5σ significance level, i.e. $N_\sigma \geq 5$;
2. the presence of at least 10 excess events, i.e. $S \geq 10$;
3. a signal of at least five times the background systematic uncertainty, that is assumed to correspond to the 1% of the remaining background events, i.e. $S/B \geq 0.05$.

where S and B denote the signal and background events in the source region, which in the Li & Ma notation correspond to $N_{on} = S + B$ and $N_{off} = B/\alpha$, with α being the ratio of the on-source time to the off-source time during which N_{on} and N_{off} photons are counted, respectively, and which also depends on the different integration regions used to estimate the two. Following the above criteria, the minimum detectable flux for 50 hours of observation has been estimated. The energy interval from 50 GeV to 100 TeV has been divided into

five independent logarithmic bins per decade of energy, as done also by CTA [86].

3.2 Two neighbor sources

In this section the case of a second gamma-ray emitter in the proximity of a main source under observation is studied and the effect on the instrument sensitivity evaluated under the hypothesis of both Gaussian (Eq. [2.2]) and non-Gaussian (Eq. [2.3]) PSF. The simulation of the two objects side by side has been performed following the approach described in §2.4.1, where the number of σ for the significant detection has been estimated according to formula 17 in ref. [148]. The simulation of the two gamma-ray emitters has been done as in §2.4.1, creating excess maps with the two objects placed apart. The response of the instrument has been described according to the analytical parameterizations reported in §2.1. In order to estimate the minimum detectable flux, a discrete set of flux bins has been simulated for the source under observation. This results in a sensitivity *range* instead of a single curve, defined by the edges of the flux bin in which the minimum flux is reached.

Hereafter we refer to the first source as *test source*, being the target of the observation, and to the other one as *background source*, since the gamma photons emitted by this nearby object represent an additional source of background for the *test source*. The Crab-like spectrum defined by Eq. [2.8] has been used both for the *test* and the *background source*. The shape of the two objects, simulated according to Eq. [2.7], is characterized by the angular sizes $\sigma_{testSrc}$ (for the *test source*) and σ_{bkgSrc} (for the *background source*). The *test source* has been assumed to be point-like while for the *background source* two different cases have been considered:

- $\sigma_{testSrc} = 0.03$ deg and $\sigma_{bkgSrc} = 0.03$ deg;
- $\sigma_{testSrc} = 0.03$ deg and $\sigma_{bkgSrc} = 0.2$ deg.

3.2.1 Event rate

Gamma-ray photons from the *background source* reaching the region of the observation limit the ability to resolve the main object. Therefore, the closer the *background source*, the higher the total amount of background. This effect is clearly seen in Fig. 3.1, where the total background rate $R_B = R_{CR} + R_{bkgSrc}$ is shown as a function of the distance between the two sources in the case of a Gaussian PSF. R_{bkgSrc} represents the additional noise due to the photons coming from the *background source*, while R_{CR} is the standard background rate due to the cosmic rays, shown as a constant black curve in the plots. Both R_{bkgSrc} and R_{CR} are computed as event rates expected in correspondence of the ROI of the point-like *test source*, defined as the circle centered at the *test source* position and with radius $R_{ROI} = 2\sigma_{PSF}$. The different colored curves are for different flux strengths of the *background source*. As expected, the brighter the *background source*, the more significant its contribution to total

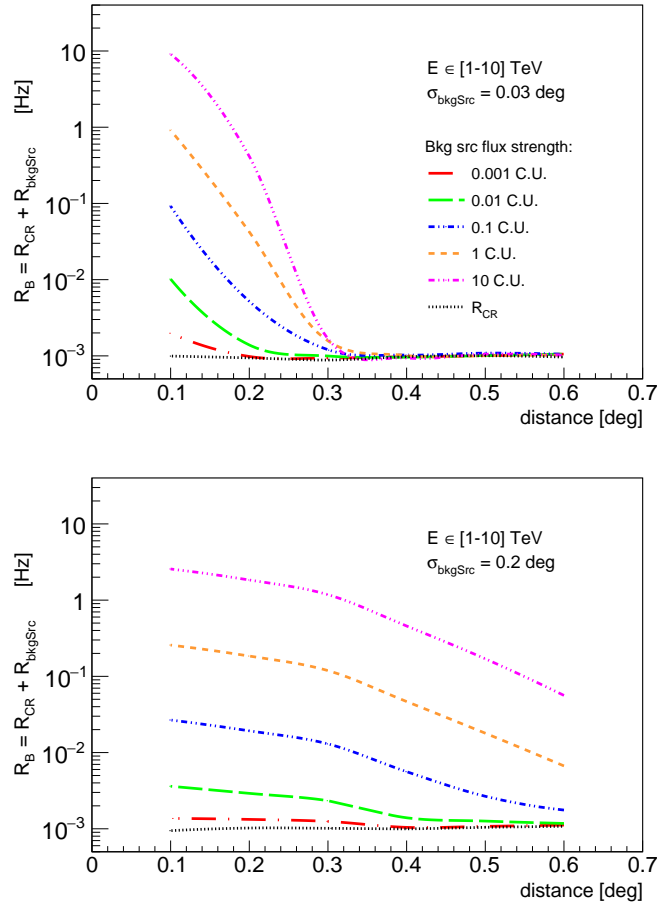


Figure 3.1: Total background rate as a function of the distance between the *test source* and the nearby gamma-ray *background source*, assuming a Gaussian PSF. The total background rate R_B is defined as the sum of the cosmic ray background, R_{CR} (black dotted line), and the additional noise due to the photons coming from the *background source*, R_{bkgSrc} . The calculations in the energy interval from 1 TeV to 10 TeV are conducted for different flux strengths and angular sizes of the *background source* indicated on the figures.

background. Comparing the two hypothesis for the size of the *background source*, the results in Fig. 3.1 show that for a point-like *background source* ($\sigma_{bkgSrc} = 0.03$ deg) the contamination of the cosmic ray background rate due to the nearby object disappears as soon as the distance between the two sources is larger than 0.3 deg, irrespective of the flux strength of the companion. On the other hand, in case of an extended *background source* ($\sigma_{bkgSrc} = 0.2$ deg) the contamination affects the observation even for larger separation distances and the brighter the *background source* the more significant the additional noise.

Similar calculations have been conducted under the assumption of a non-Gaussian PSF (Eq. [2.2] calculated for $K = 0.3$), as shown in Fig. 3.2. Apparently, the tails contribute significantly to the background, especially at large distances from the gamma-ray *background source*, further increasing the

total amount of background due to the fake emission induced by the presence of the tails. One can see that for the parameters used in these calculations, a significant contribution from the *background source* can extend up to 1 degree, i.e. an order of magnitude larger than the PSF. A comparison of Fig. 3.1 and Fig. 3.2 shows that this effect is apparently caused by the tails of the PSF.

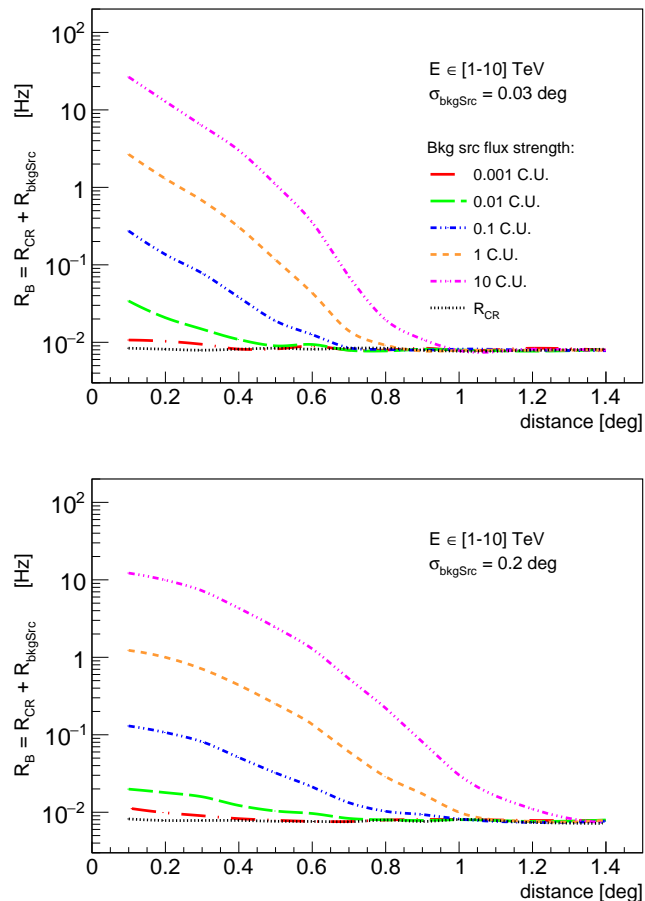


Figure 3.2: Same as Fig. 3.1 but assuming a non-Gaussian PSF with tails described by Eq. [2.3] for $K = 0.3$.

From these results it is clear that in case of a nearby *background source*, the detection rates and the background regimes depend not only on the flux strengths of the two objects, but also on their proximity and on their size. Distributions in Fig. 3.3 and 3.4 show the energy dependence of differential event rates for two different distances between the *test* and the *background* gamma-ray sources: 0.1 deg and 0.3 deg. On top of each figure the case of point-like *background source* is considered, on the bottom the extended *background source* hypothesis is shown. Solid lines are for the expectations related to the *test source* (S), dashed lines are for the total background (considering the effect of the *background source*) (B_{tot}) and the black one is for pure cosmic-ray noise (B_{CR}).

The curves in Fig. 3.3 are obtained for the pure Gaussian model of the PSF. As demonstrated in Fig. 3.1, in case of a point-like *background source*

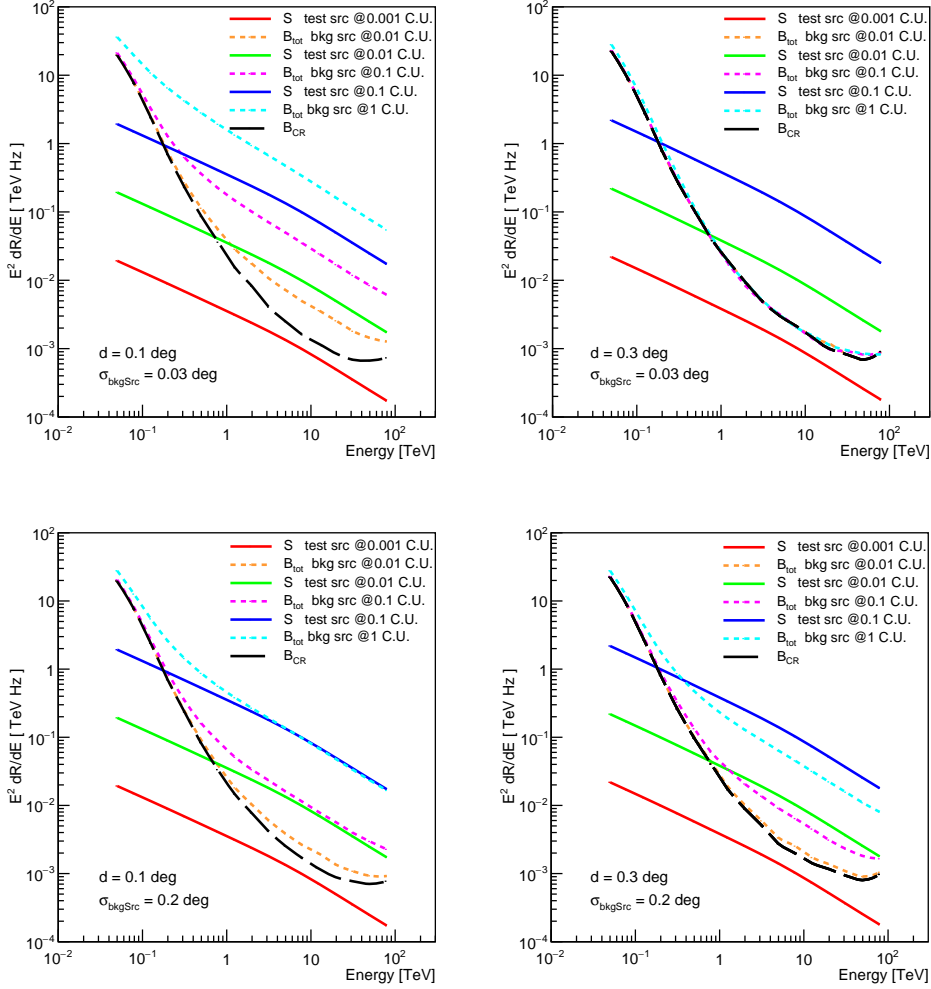


Figure 3.3: Differential event rates as a function of the energy, assuming a Gaussian PSF. Solid lines are for the gamma-ray signal from the *test source*. Dashed lines are for the total background (B_{tot}) which consists of the background induced by cosmic rays B_{CR} (black dashed curves) and background induced by gamma-rays from the neighbor gamma-ray *background source*. The calculations have been performed for different sizes of the *background source* (top panels for a point-like source, and the bottom panels for the second source with size 0.2 deg), for different distances between two sources (left panels: 0.1 deg; right panels: 0.3 deg), and for different fluxes of the *test* and *background* gamma-ray sources.

placed 0.3 deg apart, the background is reduced to the pure cosmic rays, regardless its flux strength. For an extended *background source* at the same distance, a contamination of the ROI takes place, especially when it is a very bright companion. Therefore, in this latter scenario, the background regimes depend also on the flux intensity of the *background source*. The same dependency can be observed in case of 0.1 deg separation, both for $\sigma_{bkgSrc} = 0.03$ deg and $\sigma_{bkgSrc} = 0.2$ deg: the weaker the *background source*, the sooner the background free regime is achieved in terms of energy.

In Fig. 3.4 the non-Gaussian PSF with tails (Eq. [2.2] for $K = 0.3$) is assumed. For distances as small as 0.1 deg and 0.3 deg, the effect of the nearby *background source* does not really depend on the actual size of the *background source* itself, since the size of the tails ($\sigma_{PSFtails} = 0.2$ deg) is the dominant feature size at play. The additional background induced by the presence of the tails in the PSF makes the realization of the background free regime more challenging and the presence of a bright *test source* with an intensity of at least 0.1 C.U. is needed in order to avoid observations in the background dominated mode.

All these considerations indicate that, in the presence of neighboring gamma-ray sources, the background for the *test source* can significantly exceed (depending on the flux of the *background source* and its distance from the *test source*) the rate of background events induced by cosmic rays. This would result in a significant reduction of the sensitivity of observations, specifically in regions rich in gamma-ray sources.

3.2.2 The sensitivity

The improvement in sensitivity foreseen by CTA will dramatically increase the number of known gamma-ray sources. Correspondingly, the average distance between sources will also be reduced. Although in extragalactic space the average angular distance between sources would be about 10 deg, in the case of the Galactic plane, one would always find multiple sources in a FoV. In this case the background for the *test source* caused by the surrounding gamma-ray sources can be comparable to, or even exceed, the background induced by cosmic rays. This implies that the sensitivity curves obtained under the assumption of only cosmic ray background may significantly overestimate the capability of the instrument to resolve weak sources.

Following the method described in §3.1, the flux sensitivity for 50 hours of observation of an object with a spectrum given by Eq. [2.8] and placed close to a companion described by the same spectrum has been estimated. The *background source* flux is fixed to 0.1 C.U. Such a flux intensity represents a good compromise in the contest of this study, given that a fraction of Galactic objects exhibits this flux strength (see e.g. ref. [100]) and the corresponding non-negligible effect on the *test source* which might significantly constrain the observations.

In Fig. 3.5, the differential sensitivity (shaded area) to detect a point-like source when located in proximity to a second point-like *background source*

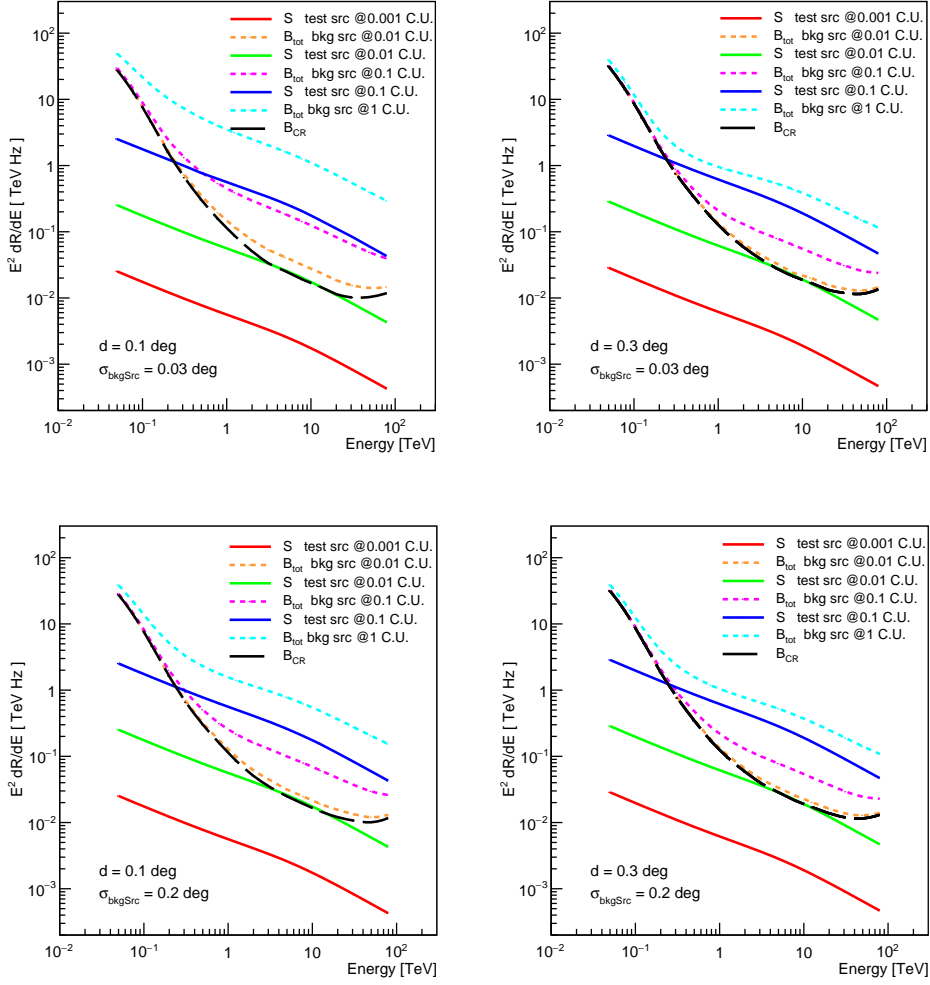


Figure 3.4: Same as in Fig. 3.3 but assuming a non-Gaussian PSF with tails described by Eq. [2.3] with $K = 0.3$.

($\sigma_{testSrc} = \sigma_{bkgSrc} = 0.03$ deg) is shown for a distance between the two objects of 0.1 deg, 0.3 deg and 0.5 deg (in green, red and blue respectively). The dashed-black line shows the publicly available sensitivity curve for a point-like source obtained by the CTA Consortium¹. The latest was calculated under the assumption that the background is caused only by cosmic rays, therefore it does not depend on the location of the *test source*.

Fig. 3.5 shows that the sensitivity to detect a point-like source in the presence of even a moderately strong source of 0.1 C.U. can be significantly (up to an order of magnitude) worse than in the case of an isolated one. As illustrated in §3.2.1, for $\sigma_{bkgSrc} = 0.03$ deg and distances larger than ~ 0.3 deg, the nearby *background source* does not affect significantly the observation of the *test source* while for distances as small as 0.1 deg, the background contamination in the ROI of the *test source* is not negligible and in therefore a significant deviation from the CTA expectation takes place. The effect cannot be ignored in environments densely populated by gamma-ray sources, as in the case of

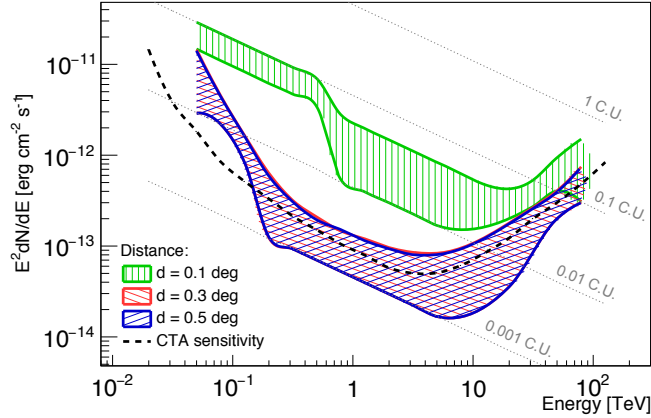


Figure 3.5: Differential flux sensitivities for a point-like *test source* corresponding to 50h observation time. The range of sensitivities are shown by shaded regions. The upper and lower edges of these regions indicate the uncertainties of simulations related to the discrete flux levels (see the text). The calculations are performed under the assumption of the existence of a neighbor point-like gamma-ray *background source* of strength 0.1 Crab. The green, red and blue regions correspond to the location of the neighbor source at distances of 0.1, 0.3 and 0.5 degrees, correspondingly. The no-difference between 0.3 deg and 0.5 deg is what expected from the background rate study in §3.2.1. In the calculations we assumed a pure Gaussian distribution for the PSF. The publicly available sensitivity expected by the CTA for a point-like source is also reported in the figure (black dashed curve)¹.

the Galactic plane. Since most of the Galactic sources are extended, in Fig. 3.6 we show the sensitivities in the regions around an extended gamma-ray source with angular size 0.2 deg, similar to the average size of the objects in the Galactic plane [100]. In this case the worsening of the sensitivity seems to

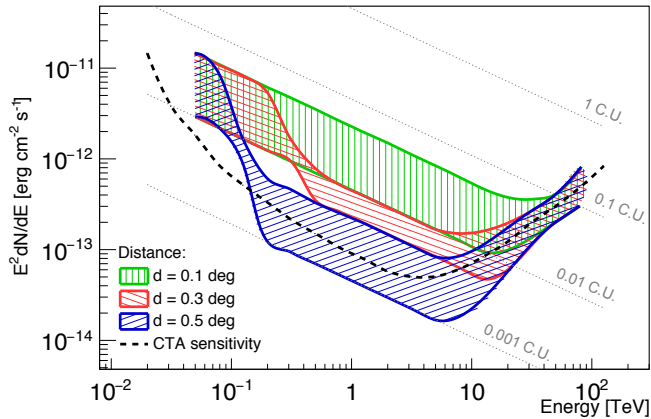


Figure 3.6: Same as in Fig. 3.5 but calculated for an extended *background gamma-ray source*.

be unavoidable also for distances larger than 0.1 deg, in agreement with results

in §3.2.1.

The sensitivities shown in Fig. 3.5 and 3.6 are obtained under the assumption that the PSF is described by a pure Gaussian distribution. However, in reality the PSF might be better represented by a broader distribution with long tails. In that case, the sensitivity around strong gamma-ray sources will be even more strongly reduced. The effect of the tails in the PSF on the sensitivity is shown in Figs. 3.7 and 3.8 (for point like and extended *background source*, respectively). It is seen that for the assumed shape of the non-Gaussian PSF with tails (calculated for $K = 0.3$) the zone of the reduced sensitivity extends up to ~ 1 deg in case of extended *background source*.

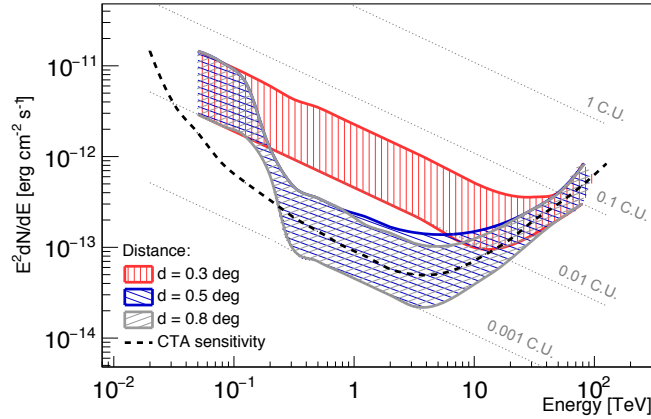


Figure 3.7: Same as Fig. 3.5, but for the case of non-Gaussian PSF with tails given by Eq. [2.3] with $K = 0.3$.

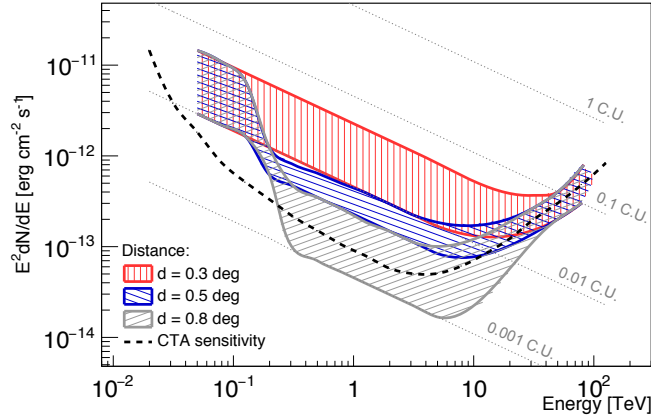


Figure 3.8: Same as Fig. 3.6, but for the case of non-Gaussian PSF with tails given by Eq. [2.3] with $K = 0.3$.

All these results demonstrate that the CTA expectations might be too optimistic in case of multiple objects in the same FoV, for which even an order of magnitude worsening with respect to the ideal CTA scenario can be observed. This would imply an increase of the required exposure time, up

to two orders of magnitude for a factor 10 worsening of the sensitivity. It is clear that such an effect needs to be seriously considered when planning the observations with the future IACT array.

3.3 Extended sources

The surveys of the Galaxy undertaken by the current ground-based gamma-ray telescopes have revealed different classes of astrophysical objects, like SNRs, PWNe and MCs. Many are observed as extended objects with respect to the angular resolution of the instruments. The improved PSF of CTA will resolve the spatial details of these galactic objects. Consequently the number of sources classified as extended is expected to increase. An important question to be addressed is therefore related to the capability of the next-generation IACT to detect these extended objects.

In this section the expected CTA sensitivity to extended VHE gamma-ray sources is estimated. The computation of the minimum flux is here achieved with an analytical approach and does not exploit the simulation of excess maps as previously done for point-like and moderately extended objects, for which the smearing of the source image induced by the PSF represented a relevant factor. In fact, given the larger size of the sources under study, the PSF and the possible presence of tails in its shape, is not anymore a crucial issue. On the other hand, the larger region observed implies a larger background rate, significantly limiting the telescope performance.

3.3.1 Event rates

The Crab-like spectrum defined by Eq. [2.8] has been used for the computation of the expected signal events. The energy integrated flux, convolved with the instrument effective area as defined in Eq. [2.4] and scaled by the observation time (i.e. 50 hours), has been assumed to be uniformly distributed over the source extension. Therefore, for a certain flux intensity, the larger the source extension the lower its photon density. Different assumption regarding the size of the spherical shaped gamma-ray source have been tested, with a radius R_{src} ranging from 0.2 deg to 2.0 deg. The largest radius has been fixed as a conservative threshold value for which the degradation of the PSF with the off-axis angle does not play any relevant effect (see e.g. ref. [171] for a study on the expected CTA off-axis performance). For a certain size of the object, the ROI used for the estimation of the background is: $R_{ROI} = \sqrt{R_{src}^2 + \sigma_{PSF}^2}$, so that an actual comparison between the size of the source and the PSF is always guaranteed (see Eq. [2.1] for the parametrization of the energy dependent PSF). The expected number of background events is therefore computed from Eq. [2.6], scaled by the exposure time and by the area of the ROI, that is $\pi(R_{src}^2 + \sigma_{PSF}^2) \simeq \pi R_{src}^2$. In Fig. 3.9 the differential rate of the background is shown for different hypothesis on the size of the gamma-ray emitter, as a function of the energy. Obviously, the larger the source extension, the large the total background contribution.

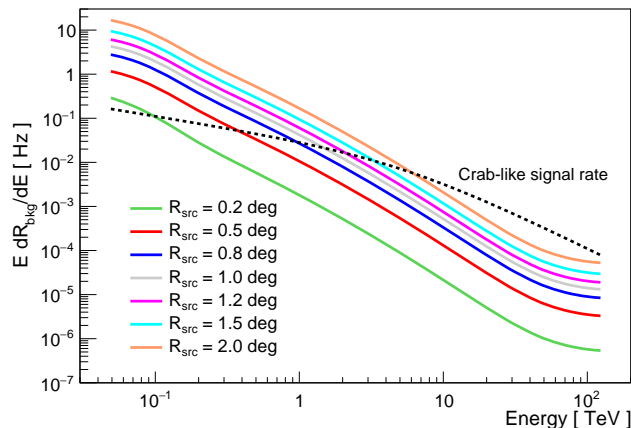


Figure 3.9: Differential background rate as a function of the energy for different hypothesis on the gamma-ray source size. The values indicated in the legend indicate the radius of the source. To account for the size of the energy dependent PSF (see Eq. [2.1]), the background is estimated over a total area given by $\pi(R_{src}^2 + \sigma_{PSF}^2)$, that is $\simeq \pi R_{src}^2$ given the large extension of the gamma-ray object. The differential signal rate for a Crab-like source is also reported in the figure as a black dotted curve.

The comparison of the background (B) with the signal from the source (S) is needed to discern whether the observation is carried out in the *background dominated*, i.e. $S/B < 1$, or in the *background free regime*, i.e. $S/B > 1$. In Fig. 3.10 the ratio S/B for 50h observation time is shown as a function of the energy for four different assumptions on the flux strength of the gamma-ray object: 1 C.U. (top-left), 0.1 C.U. (top-right), 0.01 C.U. (bottom-left) and 0.001 C.U. (bottom-right). Because of the large background rate for extended objects, even the strongest extended sources reported by IACTs, can be detected only in the background dominated regime.

3.3.2 The sensitivity

According to the methodology described in §3.1, the CTA sensitivity to extended sources has been estimated in the energy range from 50 GeV to 100 TeV, for 50 hours observation time. For a realistic estimation of the N_{on} and N_{off} counts, the background events have been randomized according to a Poissonian distribution, and then the results have been averaged over 100 realizations of the sensitivity estimation.

In Fig. 3.11 the sensitivity curves for the different assumptions on the source radius are shown. For a comparison with the CTA sensitivity for point-like objects, the same energy binning is here exploited, that is five logarithmic bins per energy decade (i.e. constant 0.2 bin width). As expected, the worsening of the sensitivity shows a dependence on the energy. At the highest energies (above few tens of TeV) the deviation from the point-like scenario is moderate, because in this energy domain the background is negligible and

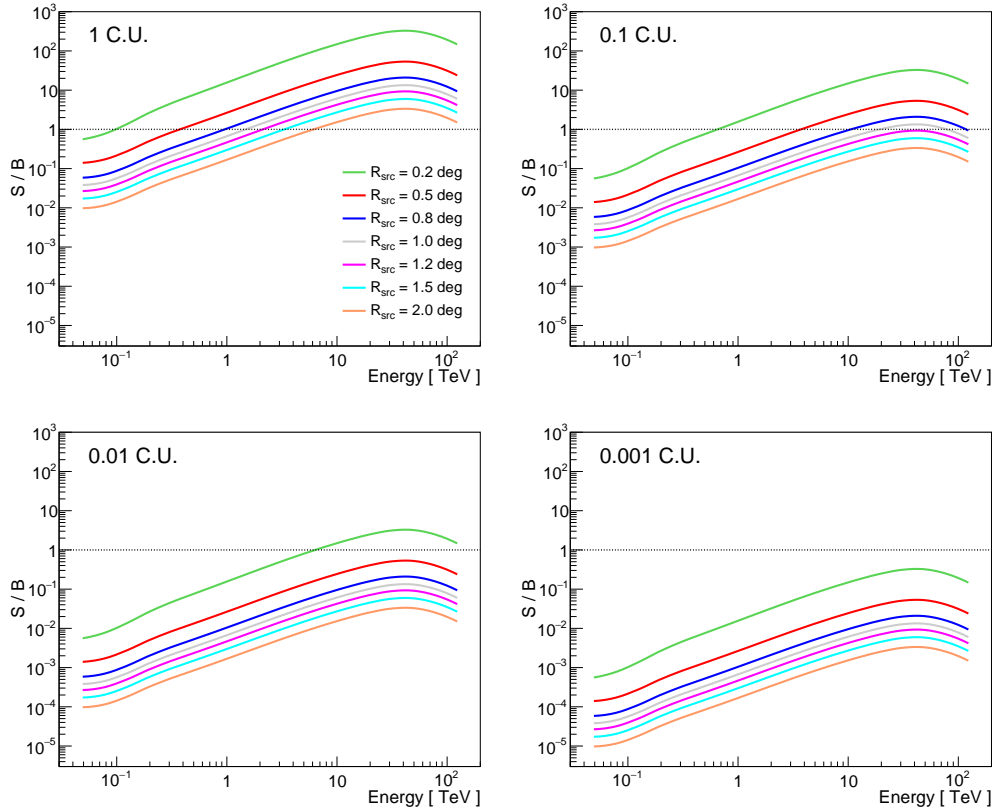


Figure 3.10: Ratio of the signal S to the background B for four different assumptions on the flux strength of the gamma-ray object: 1 C.U. (top-left), 0.1 C.U. (top-right), 0.01 C.U. (bottom-left) and 0.001 C.U. (bottom-right). In each plot, different extension of the source are considered. The horizontal black line indicate the level at which signal and background events are in equal amount, i.e. $S/B = 1$. The observation time here considered is 50 hours.

the sensitivity is limited by the photon statistics. On the other hand, the low energies suffer a significant worsening, due to the fact that below ~ 1 TeV the background dominates and the sensitivity of the Cherenkov telescopes is mainly systematics limited.

A multi-messenger application

The worsening of the sensitivity for sources with an extension of the order of ~ 1 deg significantly affects the performance of Cherenkov telescopes. However, other instruments with an intrinsic worse angular resolution are expected to suffer less the effect of observing large regions of the sky. This is the case for instance of neutrino telescopes, like KM3NeT, the next-generation neutrino telescope for which an extensive overview can be found in ref. [26]. The angular resolution of this instrument will be of the order of $\simeq 1$ deg around

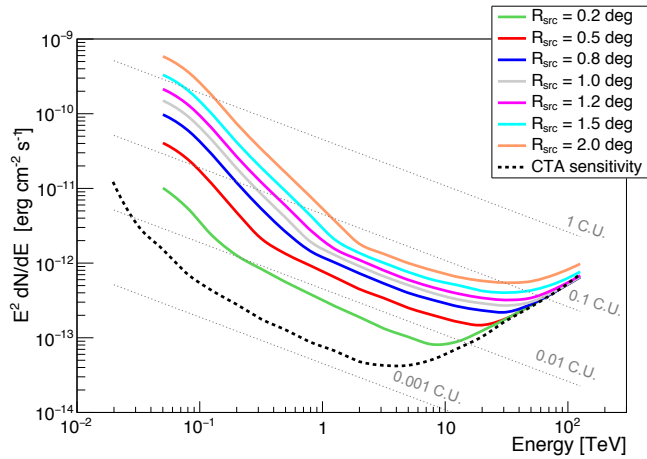


Figure 3.11: Differential flux sensitivity for extended sources corresponding to 50 h observation time. Different colors are for different hypothesis on the source radius. For each source extension, the total flux strength of the gamma-ray object is assumed to be uniformly spread all over the source area.

1 TeV, improving to ~ 0.2 deg above 10 TeV¹. Compared to the expected ~ 0.03 deg PSF of CTA above 10 TeV, it is clear that, for a neutrino telescope the observation of extended sources (≥ 0.2 deg) at VHE is not as worsening as for a CTA-like instrument.

The search for neutrino sources is generally driven by gamma-ray observations, assuming the source originating gamma-ray is of hadronic origin, from which neutrinos would naturally arise as by-products, and focusing on bright gamma-ray emitters in order to maximize the expectation on the neutrino signal. A considerable fraction of Galactic sources is observed as extended in gamma rays but only a fraction of them are characterized by very high fluxes, the majority being below the 0.1 C.U. flux level. Most likely some of these objects accelerate hadrons, resulting in gamma-ray emission through the decays of secondary π^0 mesons. Consequently, a neutrino signal might be expected as due to the decay of the charged pions (see §A for the production mechanisms of gamma rays and neutrinos in astrophysical objects). In case of extended sources with relatively weak fluxes, the reduced potential of Cherenkov telescope for extended objects might hide possible neutrino source candidates. Therefore, a comparison between the gamma-ray and the neutrino telescope sensitivities to extended sources represents a timely study to be investigated in the era of the upcoming next-generation instruments, i.e. CTA and KM3NeT.

Given the worse energy resolution of neutrino telescopes (of the order of 80% for KM3NeT [26]), the computation of the CTA sensitivity has been performed on larger energy bins. In particular, logarithmic bins with a constant width of 0.3 have been assumed, opting for a conservative approach with re-

¹The reported values for the KM3NeT angular resolution are referred to *track events*, i.e. events induced by muon neutrinos undergoing charged current interactions with the detector medium. The topology of these events is characterized by the Cherenkov light from the emerging muon that can travel long distances.

spect to the energy resolutions of both instruments. Moreover, for the sake of coherence and uniformity with the procedure used for the computation of the neutrino telescope sensitivity, here the significance level has been estimated as $\sigma = S/\sqrt{B}$. Then, in each energy bin the requirements summarized in §3.1 have been applied and the minimum gamma-ray flux estimated according to the procedure already explained in §3.3.2.

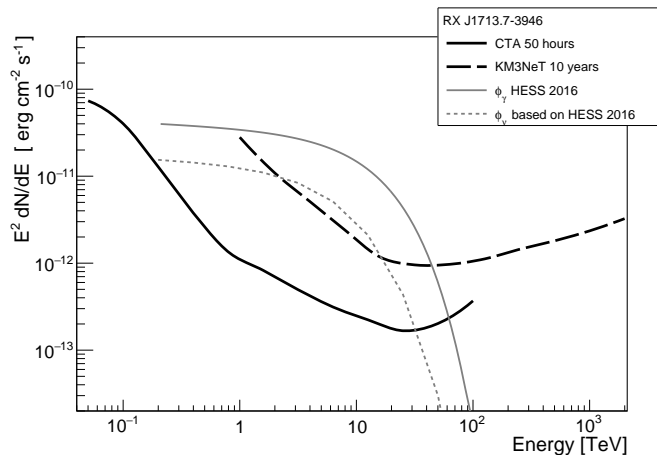


Figure 3.12: Differential flux sensitivity expected for CTA observing for 50 hours a source with a spatial extension as the one of the SNR RX J1713-3946. In the same plot the KM3NeT sensitivity (up-going muon neutrinos) to the same source is reported, as due to 10 years of data tacking with a detector made of 6 building blocks. On top of the two sensitivity curves, the RX J1713-3946 gamma-ray flux as measured in ref. [1] (best-fit exponential cutoff power-law mode) is shown. This reported gamma-ray flux has been used to calculate the expected neutrino flux from the same source. The criteria used in each energy bin for the estimation of the KM3NeT sensitivity are: (i) at least 3σ significance level and (ii) a minimum number of 3 neutrino events. S. Celli (private communication, 2017).

In Fig. 3.12 the case of the TeV shell-type SNR RX J1713-3946 is considered, which is characterized by a radius of 0.6 deg [1]. RX J1713-3946 is one of the most prominent of the young SNRs, for which so far neither the leptonic nor the hadronic model have been firmly ruled out. The intense flux (~ 0.6 C.U.) and the complex interpretation of the origin of its gamma-ray emission, makes this object a good candidate as neutrino source [137, 35, 180]. In Fig. 3.12 the CTA sensitivity for a 0.6 deg radius source is shown with the RX J1713-3946 gamma-ray flux (best-fit exponential cutoff power-law model in ref. [1]). In the same figure, the KM3NeT flux sensitivity for a 0.6 deg radius object is reported, as obtained for ten years of data acquisition with a detector made of 6 building blocks, that is three times the geometry of the

next phase detector (the so-called KM3Net 2.0, see [26])². The expected neutrino flux from RX J1713-3946 has been calculated according to the model in ref. [179] assuming a 100% hadronic origin of the measured gamma rays reported in [1] and that the measured spectrum coincides with the emitted one (i.e. no gamma-ray absorption). According to these results, around ~ 10 TeV a combined measure of gamma rays by CTA and neutrinos by KM3NeT in correspondence to RX J1713-3946 seems to be feasible. This would enable the neutrino-based astronomy to become a truly discipline and would imply a conclusive assessment on the nature of the primary particles responsible for the gamma-ray radiation from RX J1713-3946.

Another attractive object in the context of gamma rays with an hadronic origin is the Galactic center ridge. Recent observations performed by H.E.S.S. have revealed the presence of a diffuse emission which would imply the existence of a central proton accelerator up to PeV energies [11]. Here the estimation of the CTA sensitivity is done for the sky region observed by H.E.S.S. in 2006 [41], that is a box with longitudinal size of 1.6 deg (i.e. $|l| \leq 0.8$ deg) and latitudinal size of 0.6 deg (i.e. $|b| \leq 0.3$ deg). The results are shown in Fig. 3.13, together with the measured power-law spectrum of the diffuse gamma-ray emission as reported in ref. [41] and two hypothesis for an exponential cutoff on top of the same power-law, i.e. at 100 TeV and at 1 PeV in terms of gamma-ray energy. The same results obtained for the case of neutrinos are reported on the same figure. Only in the case of a 100 TeV cutoff (in gamma-ray energy) the observation of the neutrino counterpart would not be possible, being at the very threshold of the instrument sensitivity. In the other scenarios, the measurement of the neutrino and gamma-ray correlated spectra around ~ 10 TeV is foreseen. The putative presence of a cutoff in the gamma-ray spectrum around 100 TeV will be confirmed or discarded by CTA in the next future, thanks to its broad energy coverage and improved energy resolution (see §4.3 for an analysis of the CTA spectroscopic potential in case of exponential cutoff). In any case, it is clear that an important synergy between these next-generation instruments, CTA and KM3NeT, might play an effective role in the framework of multi-messenger astronomy. This synergy will be especially significant at energies beyond 10 TeV, where CTA will allow for the first time a systematic investigation of VHE gamma-ray emitters and the main contribution to the neutrino signal is expected [181].

This is evident also in Fig. 3.14, where the flux sensitivity of CTA and KM3NeT is tested for two extended objects detected by HAWC and reported in its recently published second catalog [8]: 2HWC J1825-134 (0.39 deg apart from the position of HESS J1826-130 reported in the TeVCat [73]) and 2HWC J1837-065 (0.37 deg apart from the position of HESS J1837-069 reported in the

²The response of the neutrino telescope is referred to triggered events induced by charged current muon neutrinos interactions (i.e. *track-like* events) characterized by a zenith angle larger than 80 deg (i.e. *up-going* events). For these up-going track-like events the main source of background is constituted by atmospheric neutrinos, composed of a conventional component (due to the decay of light mesons produced in atmospheric showers, estimated according to ref. [131]) and a prompt component (due to the decay of charmed mesons, important above 1 PeV and estimated according to ref. [105]). See [26] for the details.

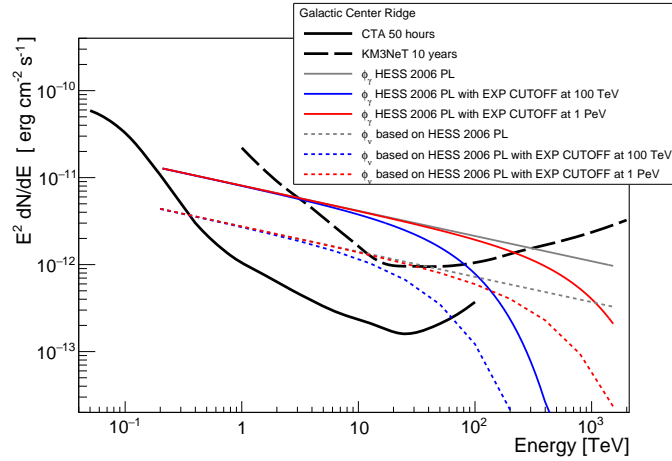


Figure 3.13: Differential flux sensitivity expected for CTA observing for 50 hours a source with a spatial extension equal to the one of the Galactic center ridge as measured by H.E.S.S. in 2006 [41]. The unbroken power-law spectrum of the diffuse gamma-ray emission as measured in ref. [41] is also reported, together with two hypothesis for a possible exponential cutoff on top of the same power-law, at 100 TeV and at 1 PeV. The KM3NeT sensitivity (up-going muon neutrinos) corresponds to the minimum detectable flux in 10 years of data tacking with a detector made of 6 building blocks. The criteria used in each energy bin for the estimation of the KM3NeT sensitivity are: (i) at least 3σ significance level and (ii) a minimum number of 3 neutrino events. S. Celli (private communication, 2017).

TeVcat [43]). The PSF of the HAWC detector is of the order of ~ 1 deg for low energy events (around few hundreds of GeV), reaching the level of less than 0.2 deg for the highest energy events (hundreds of TeV) [7]. Given the worse angular resolution of HAWC with respect to IACTs, a HAWC extended source is actually a sky region where more sources might be overlapping. The same consideration will hold also for neutrino detections, given the similar angular resolution of the instruments. Therefore, for a direct comparison among CTA and KM3NeT the fluxes reported in the HAWC catalog [8] are considered as coming from one single source. The two sources here considered correspond to the two brightest objects in the HAWC catalog, notably suitable in order to maximize the weak neutrino signal. Their radial extent is $R_{src} = 0.9$ deg for 2HWC J1825-134 and $R_{src} = 2.0$ deg for 2HWC J1837-065 (the spectral fit with the more extended source assumption is considered). Above tens of TeV, the multi-messenger detection of these extended sources seems to be feasible. Moreover, for energies around 100 TeV and for source radius as large as 2.0 deg, the cooperation between the two telescopes is especially matched. This is due to the fact that, at such VHE, the performance of the neutrino telescope does not significantly depend on the source size and the instrument angular resolution is improved; on the other hand, IACTs are strongly affected by the very large background rate and the poor photon statistics, which impoverish the gamma-ray telescope sensitivity.

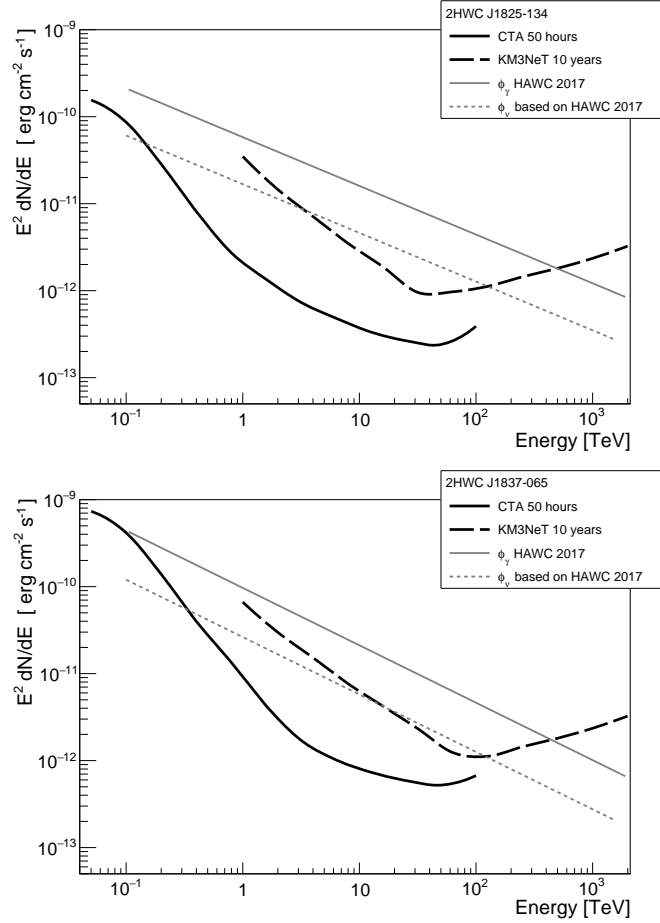


Figure 3.14: Differential flux sensitivity expected for 50 hours exposure time with CTA, observing the two brightest objects in the HAWC catalog [8]: 2HWC J1825-134 (source radius $R_{src} = 0.9$ deg) and 2HWC J1837-065 (source radius $R_{src} = 2.0$ deg). The KM3NeT sensitivity (up-going muon neutrinos) corresponds to the minimum detectable flux in 10 years of data tacking with a detector made of 6 building blocks. The criteria used in each energy bin for the estimation of the KM3NeT sensitivity are: (i) at least 3σ significance level and (ii) a minimum number of 3 neutrino events. S. Celli (private communication, 2017).

4

Spectrometric studies

The current generation of IACTs led to the detection of VHE gamma-ray sources down to flux levels as low as ~ 0.01 C.U. Their energy coverage, from a few tens of GeV [65, 130, 190] to a few tens of TeV, and their energy resolution, which can be as good as $\Delta E/E \sim 15\%$, allowed accurate spectroscopic studies and detailed reconstructions of spectral parameters and spectral features (see §1.4 for a summary on current IACTs, i.e. H.E.S.S. [117], MAGIC [67] and VERITAS [129]).

Deep observations performed to investigate the evolution of the spectra at the highest energies reached by these instruments have revealed a spectral shape that does not follow a simple power law with shape $dN/dE = I_0 (E/E_0)^{-\alpha}$ (where E_0 indicates the normalization energy and α is the photon index, see Fig. 4.1). At the highest energies a turn off of the spectrum is usually displayed, which can be generally parametrized as $dN/dE = I_0 (E/E_0)^{-\alpha} \exp \left[- (E/E_{cut})^\beta \right]$, where E_{cut} relates to the position of the cutoff energy and β determines the shape of the cutoff (see Fig. 4.1 for an illustrative example). The cutoff in the gamma-ray spectrum can be caused by several reasons. First of all, it is unavoidable because of the corresponding cutoff in the spectrum of accelerated parent particles and its shape depends on the specific acceleration mechanism of the underlying electron or nuclei population of relativistic particles (see §A.1). In addition to this intrinsic aspect, the original acceleration spectrum could be modified during the energy dependent propagation of the parent particles and this would consequently modify the gamma-ray spectrum. Moreover, sharp cutoffs could appear in the gamma-ray spectrum due to their absorption in magnetic and/or radiation fields (see §A.3 and §A.2). Gamma-ray absorption is a common phenomenon in different astrophysical environments, it could happen in compact objects, like e.g. accreting black holes, or during the propagation of the gamma rays through the intergalactic medium. Thus the cutoffs in gamma-ray spectra contain unique information about the mechanisms of acceleration of charged parent particles as well as about the astrophysical environment, like the diffusion coefficient of cosmic rays or the spectral energy distributions of the surrounding radiation fields.

Unfortunately, above a few TeVs, the reconstruction of the spectrum is hampered by the limited statistics resulting from the power-law nature of the non-thermal emission, which can result in photon indices as steep as 4

[53, 106] and the resulting fall-off in sensitivity. Beside the cutoffs, some other spectral features can be expected when observing TeV sources with improved energy resolution and enough sensitivity. For example, often the energy spectra of gamma rays can be described by a broken power-law function. The reason could be the energy losses (“cooling break”) of the parent particles or the superposition of two dominant radiation components with comparable contributions at the break energy. This function can be parametrized as $dN/dE = I_0 (E/E_b)^{-\alpha_1} (1 + (E/E_b)^{1/S})^{S(\alpha_1 - \alpha_2)}$, where E_b represents the characteristic energy for the transition from the photon index α_1 to the index α_2 , and S defines the width and the shape of the transition region (see Fig. 4.1). Spectral-morphological studies have proven to be a powerful tool to disentangle either several sources which were otherwise confused, e.g. [9], or different regions for which different acceleration, propagation or environment conditions are at play, e.g. [11].

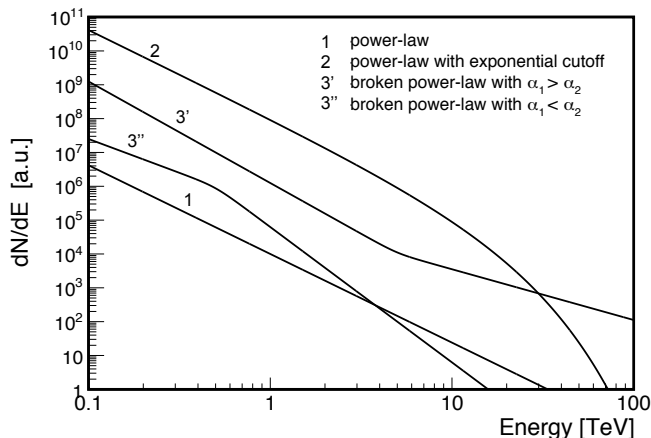


Figure 4.1: Illustration of the different spectra analyzed in this work: (i) simple power-law (see §4.2), (ii) power-law with an exponential cut-off (see §4.3) and (iii) broken power-law (see §4.4), both for $\alpha_1 > \alpha_2$ and $\alpha_1 < \alpha_2$, where α_i ($i = 1, 2$) is the photon index for different spectral components.

Although the current systems of IACTs have already demonstrated the spectrometric power of the technique by the detection of spectra of strong Galactic and extragalactic TeV gamma-ray emitters, precise spectroscopic measurements of the majority of TeV gamma-ray sources, namely the ones with energy flux less than 0.1 C.U. is still missing. To a large extent, this is true also for the strongest gamma-ray sources as long as it concerns the energies above 10 TeV. The next-generation IACT observatory, namely the CTA telescope, is expected to make a huge step towards the spectrometry of gamma-ray sources, thanks to its increased sensitivity, larger detection area, better angular and energy resolution and wider energy coverage from some tens of GeV to beyond 100 TeV [25]. In this chapter a study of the capabilities of this future instrument to disentangle spectral features is performed. Different sub-structures as well as sensitivities are expected at different energy ranges. In §4.2, the reconstruction potential for a simple power-law function

at three fiducial energy ranges (0.1 – 1 TeV, 1 – 10 TeV and 10 – 100 TeV) is firstly evaluated. Then, the capability of the instrument to reconstruct sharp features in the spectra is investigated considering two energy distributions with abrupt drops: in §4.3 the case of a power-law with an exponential cutoff is investigated and in §4.4 the response to a broken power-law spectrum is studied. For illustration, in Fig. 4.1 these different types of energy spectra are shown for arbitrarily chosen flux intensities.

4.1 Methodology

Simulations of point-like gamma-ray objects have been performed and convolved with the publicly available instrument response of the proposed Southern array of CTA¹, the so-called *2-Q* layout which has been described in §2.1. The simulation and the reconstruction of the spectra was performed with one of the officially released tools of CTA, i.e. *CTA macros* version 6¹. This tool is a C++ based routine created to simulate energy spectra that has been optimized for the specific goals of this work: the evaluation of the CTA potential to reconstruct peculiar spectral features.

The photon flux has been folded with the effective area of CTA and the specified observation time. The transition from true gamma-ray energy into the reconstructed energy, that accounts for the instrument energy resolution, has been done according to the migration matrix, which was re-weighted according to the spectral shape of the input energy distribution. The expected number of events has been calculated by summing up gamma rays from the source and the expected background events after the rejection cuts, as estimated by the CTA IRFs¹. Both signal and background event numbers have been randomized according to Poisson statistics. The number of excess events and its error have been calculated by assuming that the background level is estimated in a five times larger region than the signal region.

The energy interval from 100 GeV to 100 TeV has been considered, using 10 equally spaced logarithmic bins per energy decade. The error bars in each energy bin have been computed according to the formula 5 in ref. [148], following the Gaussian approximation of the Poissonian statistics, i.e. using the square root of the number of counts. In case of small number of reconstructed events (< 20), the uncertainties have been corrected to the actual 1σ Poissonian confidence interval, yielding to asymmetric error bars that reflect the asymmetry of the Poisson distribution. For all the spectra associated to the point-like object, the following requirements to accept a signal as statistically significant have been applied in each energy bin [86]:

1. a significance of at least three standard deviations calculated according to Li & Ma [148];
2. the presence of at least 7 excess events;

¹The *CTA macros* can be found at <https://github.com/cta-observatory/ctamacros>.

3. a minimum signal excess over the background level of 3%, corresponding to three times the assumed 1% systematic uncertainty on the background modeling.

For each of the spectral shapes studied, 100 realizations of the simulations were done to assess the statistical error of the spectral reconstruction, that is a good compromise between a truly sampling of the errors (i.e. errors are Gaussian distributed) and the computational time.

4.2 Power-law

The simplest spectral profile describing the gamma-ray energy distribution from astrophysical objects is the pure (featureless) power-law spectrum, as characteristic of non-thermal processes (see §A.1). In this work, the simulation of this featureless spectrum has been done according to the following formula:

$$\frac{dN}{dE} = k \cdot I_0 \left(\frac{E}{1 \text{ TeV}} \right)^{-\alpha}, \quad (4.1)$$

with $\alpha = 2.62$ which corresponds to the Crab Nebula power-law photon index as measured by HEGRA [38]. The flux is normalized at 1 TeV at the value $k \cdot I_0$, where $I_0 = 2.83 \cdot 10^{-11} \text{ TeV}^{-1} \text{ cm}^{-2} \text{ s}^{-1}$ is value of the Crab flux at 1 TeV [38] and the parameter k fixes the number of Crab Units (C.U.) to define the flux strength of the object. A χ^2 -fitting analysis has been performed to the above power law, which allowed the estimation of the parameter α and its error $\delta\alpha$. The fit to the simulated reconstructed spectra has been done for five separate exposures times, as reported in Fig. 4.2 and in Fig. 4.3, where the distribution of such errors $\delta\alpha$ is shown as a function of the flux strength. The error bands result from the statistical error derived as the root mean square deviation over the 100 iterations of the simulation. In Fig. 4.2, the reconstruction potential of the baseline power-law function is evaluated in three different energy intervals. As demonstrated in §2.3, the response of the instrument depends on the specific energy domain considered and, in general, different physics scenarios are expected at different energy domains. For these reasons the following differential energy ranges are investigated: [0.1 – 1] TeV, [1 – 10] TeV and [10 – 100] TeV. In each energy interval the curves show the limit for which the following conditions are fulfilled: (i) the relative error on the reconstructed photon index is less than 10%, i.e. $\delta\alpha/\alpha \leq 0.1$ and (ii) the estimated photon index is within 3σ from the simulated one.

Obviously, the larger the exposure time, the smaller the error on the spectral index and the weaker the flux that can be detected. Comparing the different energy domains shown in Fig. 4.2 one can easily verify that the low photon statistics at the highest energies ($E \in [10 - 100] \text{ TeV}$) does not allow an accuracy as good as the one that can be achieved in the other two energy intervals, i.e. from 0.1 TeV to 10 TeV, where the best performance in terms of sensitivity and energy resolution is expected [25] and the *background free* regime is already achieved for 0.001 – 0.01 C.U. objects (see §2.3.1). This is

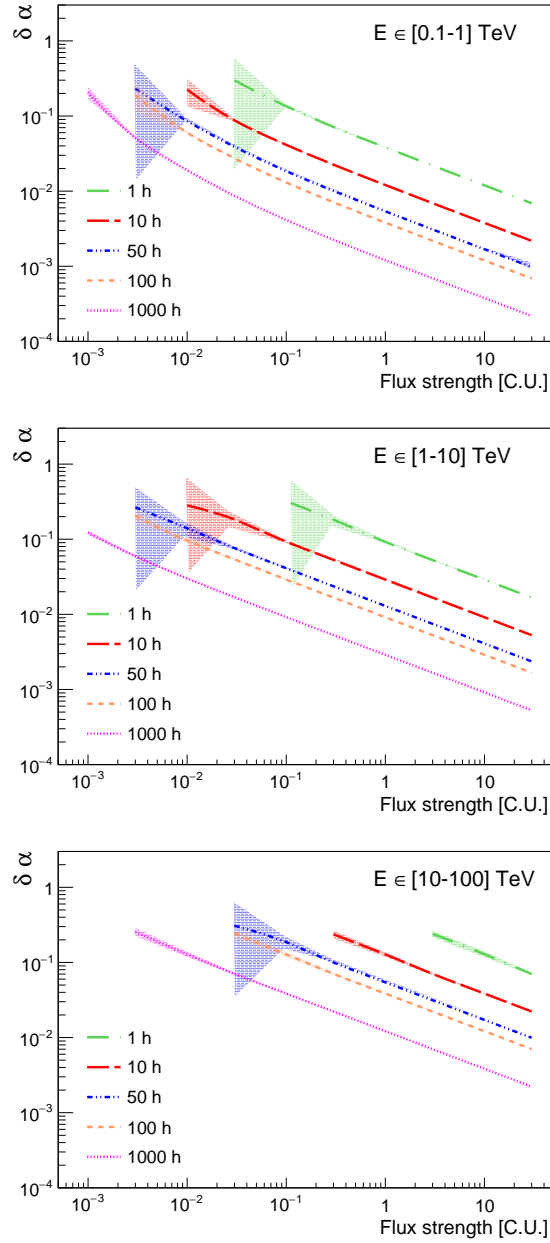


Figure 4.2: Distribution of the photon index errors $\delta\alpha$ as a function of the flux strength for five different observation times. Three energy intervals are shown: $[0.1 - 1] \text{ TeV}$, $[1 - 10] \text{ TeV}$ and $[10 - 100] \text{ TeV}$. For the selection criteria applied to the curves, please refer to the text.

a direct consequence of the factor 5 – 10 difference in differential sensitivity reached by CTA in the two different energy ranges, as shown in the previous chapter §3. For instance, for 50 hours observation time and a source flux strength of 0.1 C.U., in the interval from 0.1 TeV to 1 TeV, the estimated statistical error $\delta\alpha$ is of the order of 0.02, reaching a value as good as 0.005 for 1 C.U. object. On the other hand, between 10 TeV and 100 TeV these values are worsen by a factor ~ 10 . Above 10 TeV, to achieve a reconstruction precision of at least $\delta\alpha \leq 0.1$ with a 0.1 C.U. object, an exposure time ≥ 100 hours is needed. At the same energies ($E \geq 10$ TeV) a further reduction of the statistical error $\delta\alpha$ is expected whether very deep observations are performed: for 1000 hours exposure time, the photon index of a 0.1 C.U. source would be estimated with a statistical error of the order of 0.03. However, beside the difficulty to obtain such large exposure times in the CTA era, it should be noted that in these cases the homogeneity of the data sample is not easily guaranteed since many conditions might change (e.g. the weather, the instrumental performance, etc.) and additional uncertainties would be introduced.

Moreover, it is important to say that when considering single decades in energy, the lever arm of the reconstructed spectra is much poorer than in the case of a wide energy coverage, and this is even more true in the very high energy interval (above 10 TeV), due to the intrinsic lack of spectral points. In Fig. 4.3 the $\delta\alpha$ distribution is shown for the whole energy domain considered in this work, i.e. from 0.1 TeV to 100 TeV. For such a broad energy domain, 50 hours of observation of a 1 C.U. object permits to achieve a statistical error on the photon index as good as ~ 0.002 . This result represents a remarkable improvement of CTA with respect to the typical reconstruction accuracy of the current instruments. For a comparison, the current uncertainty on the Crab photon index estimated by MAGIC [65] would be improved by a factor 5 for a similar observation time (69 h in ref. [65]) and a wide energy coverage from 0.1 TeV to 100 TeV.

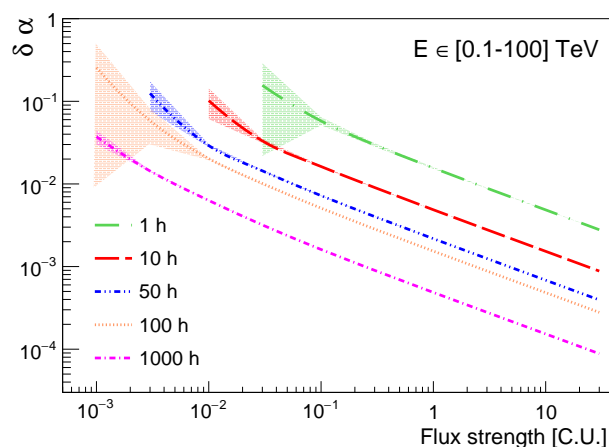


Figure 4.3: Distribution of the photon index errors $\delta\alpha$ as a function of the flux strength for five different observation times. The whole energy interval is considered, i.e. from 0.1 TeV to 100 TeV. For the selection criteria applied to the curves, please refer to the text.

These results demonstrate that excellent statistical uncertainties of the spectral parameters can be assessed with an appropriate exposure time. Nevertheless, the spectroscopic potential of the instrument may be limited by the systematic uncertainties, included in the simulations only for what concerns the accuracy on the background modeling, for which 1% systematic uncertainty has been assumed. CTA has defined high-level requirements on the allowed systematics, which will improve the overall systematic uncertainties with respect to those of the current instruments. The systematic error of both energy and effective area must be below 10% and 12%, respectively. This is a quite challenging result which requires methods and instruments beyond the current state-of-the-art [115]. However, although the systematics will be significantly reduced with CTA, they might still dominate over statistical errors when they reach extremely good values, as for $\delta\alpha < 0.01$ expected for 0.1 C.U. sources observed for more than tens of hours.

4.3 Power-law with exponential cutoff

On top of the main power-law component, at the highest energies the spectra of parent particles (electrons or protons) are expected to display a cutoff, that implies a corresponding cutoff in the gamma-ray spectra. Exponential cutoffs naturally arise in theoretical considerations, e.g. within the theory of diffuse shock acceleration, for which an exponential drop is predicted when the synchrotron energy losses are taken into account [185]. In general, the shape of the cutoff carries important information about the mechanisms acting at the source and the acceleration of the particles (see §A for a description of the production mechanisms of gamma rays in astrophysical environment). Therefore, the capability to detect and reconstruct spectra with cutoffs represents a key issue for CTA. With this in mind, simulations of power-law spectra with cutoffs at the energy E_{cut} have been performed and the corresponding CTA response evaluated. This kind of energy distribution is described by the following function:

$$\frac{dN}{dE} = k \cdot I_0 \left(\frac{E}{1 \text{ TeV}} \right)^{-\alpha} \exp \left[- \left(\frac{E}{E_{cut}} \right)^\beta \right] \quad (4.2)$$

with a power-law photon index $\alpha = 2.62$ and a differential flux normalization at 1 TeV of $k \cdot I_0$, with $I_0 = 2.83 \cdot 10^{-11} \text{ TeV}^{-1} \text{ cm}^{-2} \text{ s}^{-1}$ corresponding to the value of the Crab flux at 1 TeV [38] and k defining the number of C.U. which characterizes the flux strength of the object.

The reconstruction of the spectrum is mostly challenging in the region of the cutoff due to the strong correlation between the two parameters which define the shape of exponential drop, i.e. E_{cut} and β . An explicative example demonstrating the dependence of the two parameters is shown in Fig. 4.4. The cutoff energy E_{cut} characterizes the energy region of the drop, while the exponential index β defines the sharpness of the cutoff. Depending on β , the spectrum might show a *sub-exponential* ($\beta < 1$), *exponential* ($\beta = 1$) or *super-exponential* ($\beta > 1$) cutoff. The importance of distinguishing among these β -

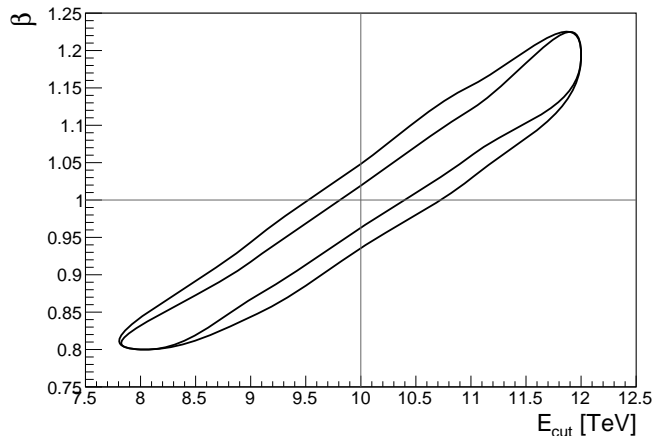


Figure 4.4: 1 and 2σ contours for the fit parameters β and E_{cut} in Eq. 4.2. The input values of the two parameters are $\beta = 1$ and $E_{cut} = 10$ TeV, reported as two gray lines in the figure. The exposure time here assumed is 50 hours and the flux strength corresponds to 1 C.U.

values is directly connected with the possibility of shedding light on the nature of the parent particles and the emission mechanisms. For instance, for an electron distribution with an exponential cutoff with index β , the shape of the synchrotron spectrum in the cutoff region exhibits a smoother cutoff with index $\beta/(\beta + 2)$ [192]. On the other hand, in case of electrons undergoing Inverse Compton scattering, the energy distribution of emitted gamma rays depends on the regime of the process, either Thomson or Klein-Nishina regime, and on the photon field. In the Klein-Nishina regime the up-scattered Compton spectrum exhibits the same exponential cutoff index β , while in the Thomson regime the shape of the gamma-ray spectrum is always smoother, as found in ref. [143]. Also in the case of neutral pion decay the energy spectrum of the highest energy gamma rays results to be smoother than the distribution of the parent protons in the cutoff region [138].

The high correlation between β and E_{cut} automatically prevents an absolute estimation of the two parameters simultaneously. Therefore, an *a priori* known value for E_{cut} (a theoretical maximum energy of the accelerated particles) has been assumed and a traditional but solid χ^2 -approach has been used to derive the other spectral parameters and to quantify the level of accuracy that can be achieved in the reconstruction of β .

In Fig. 4.5 (left side) the estimated error $\delta\beta$ is shown as a function of the flux strength of the object for three different assumptions on β ; the colored areas represent the spread of the results computed as the root mean square deviations over the 100 iterations of the simulation. In each plot, four cutoff energies are shown: $E_{cut} = 0.5, 1, 10, 50$ TeV. Lower energy cutoffs ($E_{cut} < 100$ GeV) relevant to pulsar physics are not treated here since they require a more specific treatment (see i.e. [91]). The distributions shown in Fig. 4.5 verify a set of conditions. In order to evaluate the instrument potential to measure sharp features in the spectral profile, only those events for which

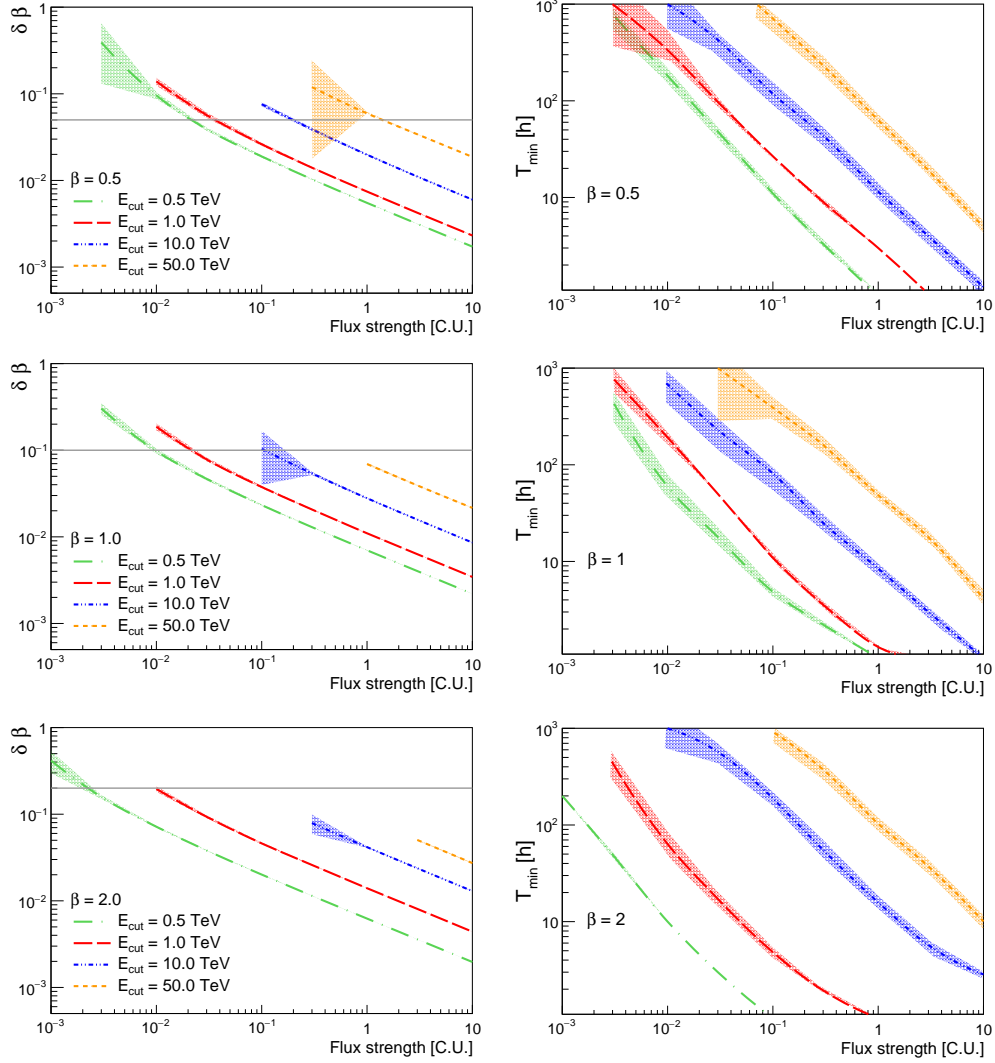


Figure 4.5: Left side: estimated error $\delta\beta$ as a function of the flux strength of the source. The gray lines indicate the level at which an accuracy on β of 10% is achieved. The observation time is 50 hours. Right side: minimum observation time needed to reconstruct the exponential profile with an absolute value of the estimated β within 3σ from the real one and a relative error $\delta\beta/\beta$ of at least 10%. On both sides, the energy interval from 0.1 to 100 TeV is considered and three different assumptions on β are shown: $\beta = 0.5$ on the top (*sub-exponential* cutoff), $\beta = 1$ in the center (*exponential* cutoff) and $\beta = 2$ on the bottom (*super-exponential* cutoff). For the selection criteria applied to the distributions refer to the text.

the reconstructed spectrum was better described by a spectral profile with an exponential cutoff instead of the featureless power-law model are selected. To quantify the goodness of the exponential fit, at least 3σ deviation of the power-law fit from the exponential hypothesis are required. This selection basically removes weak fluxes (i.e. few percentage of the Crab flux) with high energy cutoffs for which only the power-law part of the spectrum can be detected due to the extremely low flux of events expected at the highest energies. Furthermore, it is verified that such exponential-like spectra have a significance of at least 5σ (calculated according to Li & Ma [148]) in correspondence to the energy bin of the cutoff E_{cut} . For the cutoff energies under study, the lower the cutoff energy the better the accuracy of determination of the exponential index due to the large photon statistics which ensures the requested level of significance. In case of cutoffs at high energies, as for $E_{cut} = 10, 50$ TeV, the signal statistics is strongly reduced and brighter sources are needed in order to properly identify the exponential drop. For the same reason, soft cutoffs (i.e. $\beta = 0.5$) are more easily reconstructed than sharp ones (i.e. $\beta = 2$).

On the right side of the same Fig. 4.5, the minimum observation time needed to *properly* reconstruct the exponential profile is shown: in addition to the previous conditions, spectra with an absolute value of the reconstructed β within 3σ from the simulated one and a relative error $\delta\beta/\beta$ of at least 10% are selected. When the cutoff is placed in the low energy part of the spectrum, in few hours it will be possible to clearly distinguish the exponential profile for flux intensities of 0.1 C.U., while sources as faint as ≤ 0.01 C.U. will be properly identified increasing the exposure time to hundreds of hours. On the other hand, the reconstruction of 0.1 C.U. objects with high energy cutoffs around tens of TeV can be achieved in a reasonable exposure time (less than 100h) provided that E_{cut} does not exceed 10 TeV. For $E_{cut} = 50$ TeV, only very bright sources (≥ 1 C.U.) can be identified with observation times of less than hundreds of hours: the requested exposure time for a 1 C.U. object is ~ 50 h for $\beta = 0.5$ and $\beta = 1$, increasing to 100 h in case of very sharp cutoffs as for $\beta = 2$.

The other relevant issue in the reconstruction of spectra with cutoffs is the determination of the cutoff energy E_{cut} . The reconstructed spectral points may extend well beyond this energy and, in order to estimate the characteristic energy, enough statistics is needed both before it and in the region where the flux abruptly drops. In Fig. 4.6 the distribution of the maximum detectable cutoff-energy as a function of the source flux strength is shown, for four different hypothesis on the observation time. The case of an exponential cutoff profile is considered, defined as $dN/dE = I_0 \left(\frac{E}{E_0}\right)^{-\alpha} \exp\left[-\frac{E}{E_{cut}}\right]$. For such a spectral profile, the spectral parameters have been estimated without assuming an *a priori* known value for them. Moreover, for the estimation of E_{cut} the inverse cutoff energy has been used, i.e. $1/E_{cut}$, being a more stable fit parameter which does not suffer problems with singularities. To quantify the real CTA potential for the reconstruction of high energy cutoffs a wider energy coverage has been considered, from 0.1 TeV to 200 TeV, the upper bound being defined by the maximum energy considered in the publicly available CTA

IRFs¹. For each flux intensity reported in Fig. 4.6, the maximum detectable

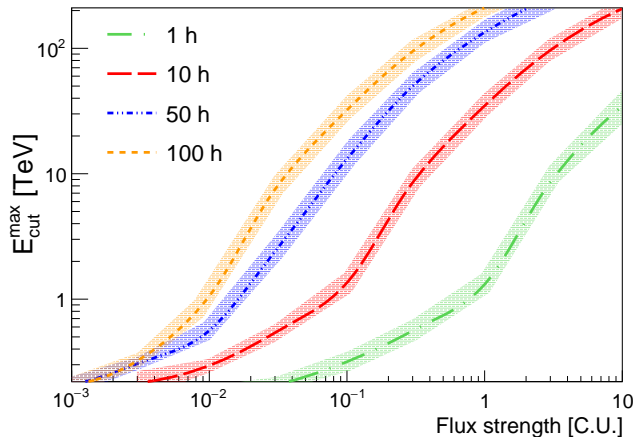


Figure 4.6: Maximum detectable cutoff-energy as a function of the source flux intensity. A spectral profile with an exponential cutoff is considered. For the selection criteria applied to the distributions the reader is encouraged to look at the text.

energy E_{cut}^{max} is defined as the highest energy for which: (i) the exponential fit deviates by $\geq 3\sigma$ from the simple power-law model, ensuring at the same time a good estimation of the photon index α (see §4.2 for a detailed treatment on the photon index reconstruction); (ii) the estimated cutoff energy is within 3σ from the simulated value and its relative error is reduced at least to 15%. The choice of the 15% level comes as a conservative approach with respect to the energy resolution of the instrument over the whole energy domain considered in this work, being of the order $\Delta E/E \simeq 0.15$ around 0.1 TeV. When large statistics are guaranteed, i.e. in case of very bright sources and/or large exposure times, the cutoff can be estimated up to energies of hundreds of TeV. In case of 0.1 C.U. objects, interesting in the framework of Galactic sources, the presence of cutoffs can be properly identified up to energies of few tens of TeVs, when an observation time ≥ 50 hours is available.

4.4 Broken power-law

The presence of two distinct spectral components can be expected either due to two different gamma-ray emitters which cannot be resolved because of a limited angular resolution (see e.g. ref. [53]), or due to a superposition of two different radiation components of the same source characterized by power-law distributions with different photon indices, as described e.g. in §A.2. In both of these scenarios, a broken power-law spectrum might be formed, which can be presented in the form:

$$\frac{dN}{dE} = k \cdot I_0 \left(\frac{E}{E_b} \right)^{-\alpha_1} \left(1 + \frac{E}{E_b} \right)^{S(\alpha_1 - \alpha_2)} \quad (4.3)$$

where E_b is the critical energy for which the transition from the photon index α_1 to the photon index α_2 takes place and S is a term which defines the width of the transition region. Here again, the flux is normalized at 1 TeV at the value $k \cdot I_0$, being $I_0 = 2.8 \cdot 10^{-11} \text{ TeV}^{-1} \text{ cm}^{-2} \text{ s}^{-1}$ the value of the Crab flux at 1 TeV [38] and k the number of C.U. defining the source flux strength. The simulation of the spectrum has been done for two different critical energies, $E_b = 0.5, 10 \text{ TeV}$, and for three different values for the first photon index $\alpha_1 = 2, 3, 4$. The reconstruction of the spectral parameters has been performed through the χ^2 fitting analysis, keeping the factor S in Eq. 4.3 fixed to the value 0.1, as down e.g. in [42].

To study the CTA potential to reconstruct sharp features in the spectra, the broken power-law spectrum has been compared to the featureless power-law hypothesis. To distinguish between the two spectral profiles, a quantity to evaluate the correct reconstruction of the two different photon indices has been defined. For that, only those events for which the reconstructed value of both α_1 and α_2 deviates no more than 3σ from the simulated values have been selected. Secondly, to test whether one can distinguish the spectral profiles, the degree of separation between the two reconstructed indices has been quantified as:

$$\Sigma = \frac{\alpha_1 - \alpha_2}{\sqrt{\delta\alpha_1^2 + \delta\alpha_2^2}} \quad (4.4)$$

where α_i and their error $\delta\alpha_i$ ($i = 1, 2$) are the reconstructed parameters. The distribution of this quantity Σ is shown for a wide range of values of α_2 as function of the flux strength in Fig. 4.7, 4.8 and 4.9 for $\alpha_1 = 2$, $\alpha_1 = 3$ and $\alpha_1 = 4$, respectively.

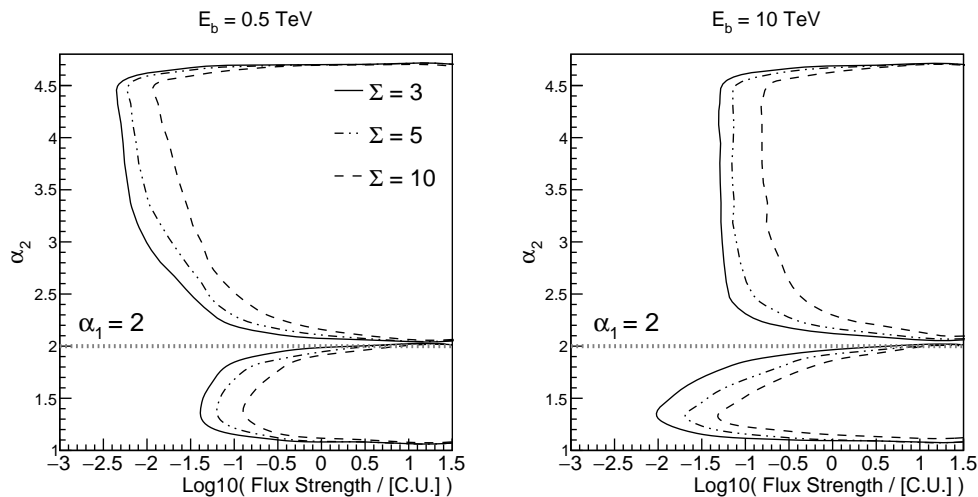


Figure 4.7: Distribution of the quantity Σ in Eq. 4.4 for different combinations of α_2 and flux strengths, in the case of $\alpha_1 = 2$. The contours $\Sigma = 3$ (solid line), $\Sigma = 5$ (dashed-dotted line) and $\Sigma = 10$ (dashed line) are shown. The simulated observation time is 50 hours. For the selection criteria applied to the curves, please refer to the text.

In each plot, the contours for $\Sigma = 3$, $\Sigma = 5$ and $\Sigma = 10$ are shown.

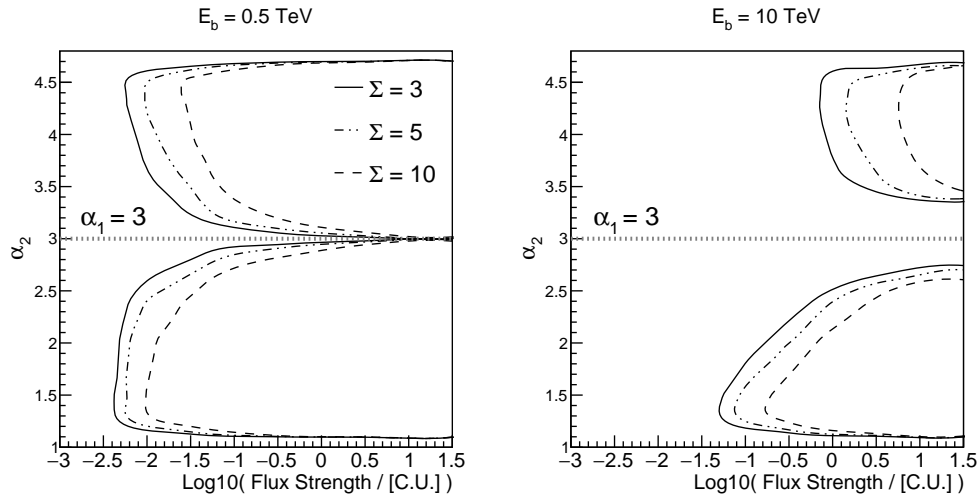


Figure 4.8: Same as in Fig. 4.7 but for the case $\alpha_1 = 3$.

Whenever the condition $\Sigma \geq 5$ is verified, one can safely state that the two spectral components are clearly separated at a high significance level. As expected, the best separation can be achieved when both the flux strength and the difference between the input value of α_1 and α_2 are large. When the breaking point is in the low energy part of the spectrum, as for $E_b = 0.5$ TeV, for flux strengths ≥ 0.1 C.U. the separation of the two profiles is guaranteed for a wide range of hypothesis on the value of the two photon indices, while for the detection of sources as weak as 0.01 C.U., in order to distinguish α_1 from α_2 at a significance level $\Sigma = 5$, a minimum difference between the two photon indices $\Delta\alpha = |\alpha_1 - \alpha_2| \geq 1$ is required. On the other hand, when the break

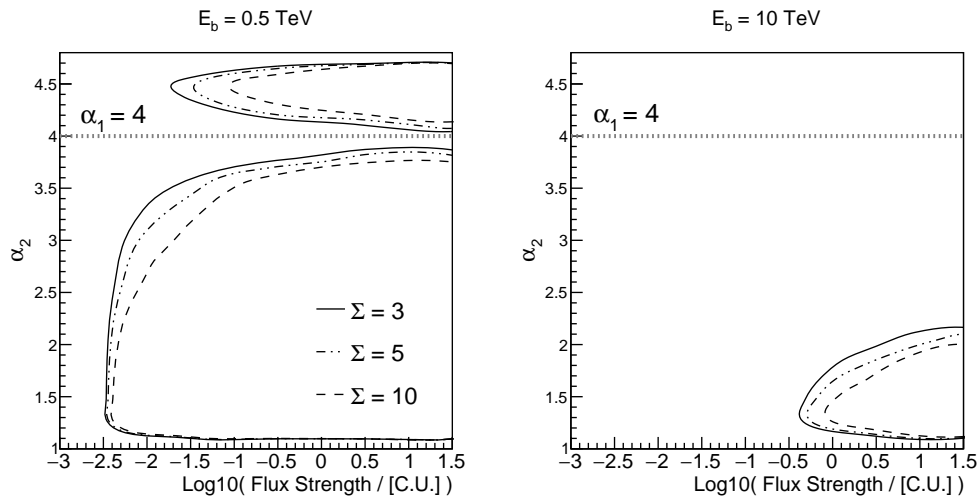


Figure 4.9: Same as in Fig. 4.7 but for the case $\alpha_1 = 4$.

energy is relatively high, as for $E_b = 10$ TeV, the main limitation comes from the low photon statistics. Therefore, the steeper the first spectrum defined by α_1 , the smaller the parameters space in terms of α_2 and flux intensity for which a proper separation can be ensured. For the same reason, the case $\alpha_1 > \alpha_2$ is

always favored with respect to the case $\alpha_1 < \alpha_2$.

5

Summary and conclusions

In this thesis I explored the potential of the next-generation IACT array for morphological and spectrometric studies of VHE gamma-ray sources. This study is important for understanding the capability of the upcoming CTA observatory, which is designed to achieve significant performance improvements with respect to the existing instruments (H.E.S.S. [117], MAGIC [67] and VERITAS [129]). The improvement concerns the larger effective area, wider energy coverage, and better angular and energy resolution. All these factors together are expected to improve the sensitivities of current detectors by an order of magnitude [25, 19, 86].

After an introduction on the specifics of the IACT technique and an overview on the CTA facility, I presented a detailed study aimed to understand the instrument potential to conduct morphological analysis of gamma-ray objects. The basic characteristics of the array of telescopes (i.e. its effective area, background rate, energy and angular resolution) have been parameterized using simple analytic representations based on the publicly available CTA instrument response functions. In addition to the ideal (Gaussian form) PSF, the impact of more realistic non-Gaussian PSFs with tails has been considered. Simulations of isolated point-like and extended sources have been used as a benchmark to test and understand the response of the instrument. The reconstruction of the source morphology has been performed through the estimation of its gravity center and its size and the minimum time needed for the estimation of such parameters within 3σ from their real value has been defined. In the energy interval from 0.1 to 10 TeV, the morphology of point-like objects with a flux of 0.1 C.U. will be reconstructed with only few hours of observation. For the same 0.1 C.U. class-objects, the exposure time needed to reconstruct the morphological parameters increases to tens of hours both in the low energy domain (0.05 – 0.1 TeV) and at very high energies (above 10 TeV), basically due to the large background rate and the poor photon statistics, respectively. The simulation of the isolated source has also been used to test the effect of the tails of the PSF on the capability to resolve the source morphology. When the contribution of the tails to the global PSF amounts to at least 5% of the Gaussian peak value, a significant misidentification of the source features emerges due to the artificial emission induced by the presence of the tails.

Then, I investigated the capability of the instrument to resolve multiple

sources in the same FoV. In particular, I analyzed (i) the effect of locating a compact source on top of a diffuse halo-type object, illustrating the case of Active Galactic Nuclei surrounded by extended emissions, and (ii) the case of two nearby sources, which could appear in densely populated environments. These studies confirm that the presence of the tails in the PSF compromises reliable assessments on the source morphology. The presence of the tails in the PSF limits the chance to disentangle the compact object from the extended halo, preventing the reconstruction of the extended emission when it is fainter than the central source. This worsening of the potential induced by the presence of the tails significantly reduces also the capability of the instrument to isolate multiple objects clustering in the same region. When the tails contribution is not-negligible, the separation of two close emitters is possible only for sources ≥ 1 deg apart, provided that none of the two source fluxes significantly exceeds the other, otherwise the weaker object turns out to be hidden by the brighter companion.

This latter scenario is of particular interest in the framework of Galactic objects, where the presence of more than one source in the same FoV is expected. Beside the noise due to the presence of the tails in the PSF, I found that a second gamma-ray emitter in the proximity of a test source represents an unavoidable source of additional background which can not be distinguished from the real gamma-ray signal coming from the test object. Consequently, the sensitivity of CTA reported in previous studies could be more modest if the test source is located in complex environments densely populated by gamma-ray emitters. I quantitatively studied this effect under the different assumptions for the shape of the PSF. It has been demonstrated that even for a relatively modest “background” source of strength 0.1 C.U., the background from this neighboring source can exceed the cosmic-ray background at distances up to 0.3 deg or even ~ 1 deg if the PSF is characterized by non-negligible tails. Depending on the PSF shape and on the distance to the test source, the minimum detectable flux is increased by a factor of a few or even by an order of magnitude. This implies an increase by one to two orders of magnitude of the required minimum observation time. This result should be taken into account when planning the observations with future IACT arrays for specific objects, especially in the Galactic plane. Generally, this statement concerns all energy intervals. However, one should note that the situation could be more optimistic at multi-TeV energies. In fact, above 10 TeV (i) the energy resolution becomes better, (ii) the tails of the PSF are predicted to be more compact thanks to the higher telescope multiplicity per event (which would reduce the fluctuations responsible for the tails), and (iii) a (relatively) small number of multi-TeV sources (PeVatrons) is expected.

A factor of 10 improvement in sensitivity foreseen by CTA [86] will be reduced also for extended object. Most of the gamma-ray emitters lying in the Galactic plane are better described as extended objects rather than point-like sources. Therefore, the ideal scenario for which the CTA sensitivity curves have been calculated, i.e. isolated point-like object, will not be easily guaranteed when conducting observations of the TeV Galactic sky. The level of

degradation of sensitivity for extended sources depends on energy. Above few tens of TeV the deviation from the point-like scenario is moderate, because the sensitivity is limited by the photon statistics. On the other hand, the low energies suffer a significant worsening, by a factor ≥ 10 around 50 GeV (depending on the source extension), due to the fact that below ~ 1 TeV the background dominates and the sensitivity of the Cherenkov telescopes is mainly systematics limited. The strong effect for sources with an extension of the order of ~ 1 deg is clear in the light of the CTA arcminute resolution. Less degradation is expected for instruments with worse angular resolution, like the neutrino telescopes [26]. In this regards, a comparison between the two next-generation telescopes is an important issue. The reduced effect in case neutrino telescope highlights the possibility to start an effective cooperation in the framework of multi-messenger astronomy, where the detection of the neutrino counterpart would provide a robust evidence for the presence of an hadronic accelerator. The synergy between the gamma-ray and the neutrino telescopes is found to be especially significant above 10 TeV, where CTA will provide the first systematic search of VHE gamma-ray emitters and the main contribution to the neutrino signal is expected.

Another import issue for the future gamma-ray telescopes is related to their capability to perform accurate spectrometric studies. In this regard, I conducted a spectrometric analysis of VHE point-like objects, testing the CTA potential to reconstruct different spectral profiles associated to the gamma-ray source. It has been demonstrated that the large photon statistics provided by the large detection area of CTA coupled with the (average) 10% energy resolution, will provide adequate spectrometry for gamma-ray sources in the interval from hundreds of GeV to 100 TeV for objects fainter than 0.01 C.U.

First, the case of a featureless power-law spectra has been studied, expressed as $dN/dE \propto E^{-\alpha}$. In the energy range between 0.1 and 10 TeV, where the IACT technique has been proven to have an optimal response, short flares (~ 1 h) exhibiting a featureless energy distribution can be reconstructed for fluxes as low as 0.1 C.U. In the same energy band (0.1 – 10 TeV), increasing the observation time to 50 hours allows the determination of the photon index with an error $\delta\alpha \leq 0.1$ for 0.01 C.U. objects and as precisely as $\delta\alpha \leq 0.01$ for very strong sources (≥ 1 C.U.). On the other hand, when limiting the observation to the PeVatron regime (energies above 10 TeV), with 50 hours of exposure time CTA will be able to reconstruct photon indices with statistical error $\delta\alpha \leq 0.1$ only for objects with a flux ≥ 0.1 C.U. For fainter sources (< 0.1 C.U.), the photon index could be estimated only with very deep observations lasting more than 100 hours. When the whole energy interval from 0.1 TeV to 100 TeV is considered, 100 hours of observation time would allow the reconstruction of objects as weak as 0.001 C.U. As a comparison, for a weak source like Tycho with a flux ~ 0.01 C.U., the statistical error of the photon index could improve from the current ~ 0.4 to 0.02 for comparable observation time (150 h) [161]. This result shows a significant improvement of the potential of CTA with respect to the current instruments.

Beside the simple power-law spectral profile, the CTA capability to re-

construct sharp spectral features has been estimated, considering the case of exponential cutoffs and spectral breaks. In case of spectra with exponential cutoffs, described as $dN/dE \propto E^{-\alpha} \exp \left[- (E/E_{cut})^\beta \right]$, it has been demonstrated that for moderately strong sources (flux > 0.1 C.U.), CTA will be able to derive with less than 100 h exposure time power-law energy profiles with super-exponential cutoffs as sharp as $\beta = 2$, provided that the characteristic energy of the cutoff E_{cut} does not significantly exceed 10 TeV. For cutoffs around 500 GeV the reconstruction of a super-exponential index $\beta = 2$ can be achieved with only 1 hour of observation. Unfortunately, for $E_{cut} = 50$ TeV, only very bright sources (≥ 1 C.U.) can be identified in a reasonable exposure time, i.e. less than hundreds of hours. Another important point to be addressed in the context of spectra with exponential cutoffs is related to the maximum energy of the cutoff, E_{cut} , that can be reconstructed. This problem has been studied for an exponential cutoff, $\beta = 1$. I found that CTA will detect cutoffs up to hundreds of TeVs. This result proves the detection potential of CTA in the PeVatron domain, as long as deep exposure are performed (more than 50 hours for objects above 0.3 C.U.). With ≥ 50 hours of observation, 0.1 C.U. objects with cutoffs around few tens of TeV will be reconstructed. A fraction of objects with such flux strength are found in the Galactic plane (see e.g. [100]), for which CTA will provide accurate spectrometric analysis.

The other scenario investigated in this thesis, entertains the possibility to measure a broken power-law spectrum, parametrized as $dN/dE \propto (E/E_b)^{-\alpha_1} (1 + (E/E_b)^{1/S})^{S(\alpha_1 - \alpha_2)}$, with E_b the characteristic energy of the break. When the transition takes place at the TeV scale, ≥ 0.1 C.U. objects will be reconstructed as long as the two photon indices α_1 and α_2 differ by a factor as small as $\simeq 0.4$ for moderately strong objects (0.1 C.U.) and down to $\simeq 0.1$ for strong sources (> 1 C.U.). Even for source flux (or fluxes) of the order of a few percentage of the Crab flux (~ 0.01 C.U.), the separation of the two components is achieved, provided a minimum separation between the photon indices $|\alpha_1 - \alpha_2| \geq 1$. On the other hand, when the transition takes place at higher energies (around 10 TeV), the reduced photons statistics represents the main limitation to resolve the two spectral profiles and very steep spectra are strongly disfavored. For a photon index α_1 as steep as 4, only bright (at least of the order of the Crab flux) and very hard ($\alpha_2 \leq 2$) second spectral components survive the dropping of sensitivity and can be reconstructed. The potential of CTA applied to the case of broken-power law spectra, is crucial for regions in which a high source confusion is expected, as the Galactic plane.

It is important to note that, the spectroscopic studies presented in this thesis might be hampered by the systematic uncertainties. Even though statistical errors will be reduced with a more sensitive instrument like CTA, they might be dominated by such systematics, despite the expected improvement with respect to the current instruments (see e.g. ref. [115] for the CTA requirements on the allowed systematics). On the other hand, the IRFs released by the CTA Collaboration and exploited in this work, are obtained under the assumption of discovery cuts aimed to maximize the differential sensitivity at each energy bin, which in turn do not optimize the telescope potential to

perform high precision analysis. Therefore, room for improvement when using cuts tailored to maximize the reconstruction accuracy is expected.

I am currently evaluating the spectrometric potential of the instrument to measure more peculiar substructures such as lines or narrow peaked emissions. Generally, the gamma-ray spectra at HE and VHE are characterized by continuous energy distributions, as those considered in this thesis. However, a narrow, line-type radiation is expected e.g. from Dark Matter (DM) annihilation. In this case the energy of the gamma-ray line contains direct information about the mass of the DM particles. Formation of narrow gamma-ray line emission can be realized also in astrophysical scenarios: VHE gamma-ray line features might arise due to unshocked electron/positron winds created by pulsars [48, 88]. Analogously to what done for the measure of sharp spectral features, the CTA capabilities to reconstruct photon line-like emissions is currently under investigation. The indirect detection of DM through secondary photons is one of the main key science project of the CTA Collaboration. Therefore, an estimation of the instrument potential to reveal such peculiar spectral signature emerging from DM annihilation is of prime importance for future DM searches.

As next steps I am planning to work on a real astrophysical application of the results achieved up to now, exploring the instrument potential for deep morphological and spectrometric studies of the diffuse background emission in the Galactic plane region. A proper treatment of the large-scale diffuse VHE gamma-ray emission, combined with a detailed analysis of extended sources in crowded environments, is a key issue to allow a deeper understanding of Galactic source populations and diffuse emission origins. This issue is one of the most crucial science projects of CTA. The challenge is to understand how to face the problem of source confusion, which unavoidably will show up when observing the densely populated Milky Way region. The results presented in this thesis on nearby emitters and extended objects will be extended to the specific astrophysical scenario of interest. Future research works will focus on the evaluation of the accuracy level at which the diffuse emission of interstellar origin can be detected and mapped with CTA, exploring morphological and spectrometric analysis of the different emission models.



Gamma-ray production and absorption mechanisms

The gamma-ray radiation is the only component of the electromagnetic spectrum that cannot be generated by the thermal motion of charged particles in matter since it is not possible to reach the required minimum temperature to produce gamma rays by thermal processes. For example, in case of a black-body following to the Wien's law, i.e. $\lambda_{max} \cdot T = 2.898 \cdot 10^{-3} \text{ [m} \cdot \text{K]}$, to produce one MeV gamma ray, a temperature of the order of 10^9 K would be needed. For a comparison, the nuclear fusion inside the Sun occurs at 10^7 K , corresponding to keV photons. The high energy gamma-ray electromagnetic radiation is therefore an indication that non-thermal processes are taking place. These processes relevant to the gamma-ray production imply the presence of relativistic charged particles (electrons, positrons, protons or nuclei) accelerated in energetic astrophysical environments. The interaction of these accelerated particles with interstellar ambient targets, in forms of *matter*, *radiation* and *magnetic fields*, generates the gamma rays.

There is a rather wide variety of non-thermal phenomena as the origin of gamma rays of different energies, the disentanglement of which is not always a straightforward task. In the following, first some basic concepts are explained and then the most relevant production and absorption mechanisms that operate effectively in the HE and VHE regimes are listed and described according to the specific target of interaction. More detailed descriptions can be found e.g. in [32, 30, 149].

A.1 Basic overview

The calculation of the expected spectrum of gamma-ray photons emitted by a population of particles through a certain process requires the knowledge of the cross section of the process σ and the energy distribution of the parent particles $N(E)$.

The cross sections of all electromagnetic processes are calculated with great accuracy within the quantum electrodynamics theory, see e.g. [122, 135, 51]. On the other hand, the hadronic processes are basically known from the accelerator data, where the cross sections have been measured with adequate accuracy for the aim of the astrophysical applications.

The population of the parent particle is described by its distribution in energy $N(E)$. Generally, $N(E)$ is time-dependent function and its calculation is not a trivial task. It requires the computation of the injection spectrum $Q(E, t)$, which depends on the acceleration mechanism acting at the source, as well as the transport of particles due to diffusion and convection [97]. A simplified equation describing the evolution of the particle distribution can be written in the form:

$$\frac{\partial N}{\partial t} = \frac{\partial}{\partial E}[PN] - \frac{N}{\tau_{esc}} + Q \quad (\text{A.1})$$

where $N = N(E, t)$ is the parent particle energy distribution, $P = P(E) = -dE/dt$ is the energy loss rate, $Q = Q(E, t)$ is the injection spectrum, and τ_{esc} is the escape time of particles from the source due to diffusion and convection, $\tau_{esc} = (1/\tau_{diff} + 1/\tau_{conv})^{-1}$. To solve this equation, one can assume that the total number of particles remains constant, i.e. $\partial N/\partial t = 0$. This solution is called *steady state particle distribution* since it describes a stationary distribution of the parent particles. Moreover, if one assumes that the escape time is much longer than the energy loss rate, the term proportional to τ_{esc}^{-1} can be neglected and Eq. [A.1] solved as:

$$N(E) = \frac{1}{dE/dt} \int_E^\infty Q(E')dE' \quad (\text{A.2})$$

where the energy loss rate is the sum of all the processes relevant in the emitter region. For each process at play, the characteristic energy loss rate can be estimated as $dE/dt = E/t_{cool}$, where

$$t_{cool} = (k\sigma nc)^{-1} \quad (\text{A.3})$$

is the so called *cooling time* for a process with an inelasticity k and a probability of interaction σ in a target medium with density n . This parameter t_{cool} is a useful mean to estimate the efficiency of a certain process: the gamma-ray production is effective when the cooling time does not excess (i) the age of the source and (ii) the cooling time of other competing radiation mechanisms.

The injection function is generally assumed to be a power-law $Q(E) \propto E^{-\alpha}$, as characteristic of the non-thermal processes. This statement is based (i) on the observational evidence of VHE spectra characterized by power-law profiles and (ii) on the theoretical prediction according to which stochastic acceleration produces power-law spectra. On top of this power-law, a high-energy cutoff might be expected, $Q(E) \propto E^{-\alpha} [\exp(-E/E_c)]^\beta$, where β defines the sharpness of the spectrum in the cutoff region. The cutoff energy E_c can be estimated through the comparison of the acceleration rate with the cooling rate, i.e. $t_{acc} = t_{cool}$. The acceleration time can be expressed as:

$$t_{acc} = \eta(E) \frac{E}{ec^2 B_\perp} \quad (\text{A.4})$$

where $\eta(E) \geq 1$ measures the efficiency of the acceleration. The term (E/ecB_\perp) corresponds the gyroradius of the charged particle in the presence of a uniform magnetic field, i.e. $r_g = mv/qB \rightarrow (E/c)(1/eB)$ with E the energy of the relativistic particle. For the case of diffusive shock acceleration in a

non-relativistic shock, the parameter $\eta(E)$ is related to the shock properties as:

$$\eta \simeq 10 \frac{D(E)}{r_g c} \left(\frac{c}{v_s} \right)^2 \sim \frac{10}{3} \left(\frac{c}{v_s} \right)^2 \quad (\text{A.5})$$

where v_s is the shock velocity and $D(E)$ is the diffusion coefficient which in the Bohm regime can be given by $D(E) = r_g c/3$ [97]. The cutoff energy E_c is then found from the balance of Eq. [A.4] and the cooling time of the dominant process.

As illustrated by Eq. [A.2], the energy losses of the parent particle population modify their spectrum and therefore the evolved particle energy distribution $N(E)$ is determined by the energy dependence of the energy loss term. For energy losses proportional to the particle energy, $dE/dt \propto E$, as for bremsstrahlung and adiabatic losses, the evolved spectrum will repeat the injection spectrum, $N(E) \propto E^{-\alpha}$. For $dE/dt \propto E^2$, as typical of synchrotron radiation and Inverse Compton scattering in non-relativistic regime, the steady state distribution will be steeper, $N(E) \propto E^{-(\alpha+1)}$. On the other hand, the stationary spectrum will be harder, $N(E) \propto E^{-(\alpha-2)}$, for energy loss rate with an inverse dependence on the particle energy $dE/dt \propto E^{-1}$, as for Inverse Compton interactions in relativistic regime.

Once the parent particle injection spectra and the cooling times are known, one can compute the total amount of energy in the volume V of the source:

$$W_{e,p} = \int_V \int_{E_{min}}^{E_{max}} E N_{e,p}(E) dE dV \quad (\text{A.6})$$

Once this energy budget is calculated, the emitted gamma-ray radiation through a certain process with cooling time t_{cool} can be estimated as:

$$F \simeq \frac{W_{e,p}}{4\pi d^2 t_{cool}} \quad (\text{A.7})$$

A.2 Interactions in radiation field

Production process: Inverse Compton

The Inverse Compton (IC) scattering is the process in which high-energy electrons scatter low energy photons and transfer part of their energy to the photons. IC is extremely important in high energy astrophysics since it provides a mechanism to transfer energy from accelerated ultra-relativistic electrons to the ambient photon field, giving rise to a VHE emission up to tens of TeV.

The total cross-section of the process depends only on the product κ of the interacting electron energy ε_e and the target photon energy ω , i.e. $\kappa = \varepsilon_e \omega$, with all the energies given in units of $m_e c^2$. For $\kappa \ll 1$, the process occurs in the non-relativistic regime, or *Thomson regime*, and the classical cross-section describes the process probability. On the other hand, for $\kappa \gg 1$ the ultra-relativistic regime, or *Klein-Nishina regime*, takes place and a modified

cross-section decreasing with κ holds. In particular:

$$\begin{aligned}\sigma_{IC} &\simeq \sigma_T(1 - \kappa) && \text{for } \kappa \ll 1 \\ \sigma_{IC} &\simeq \frac{3}{8}\sigma_T\frac{\ln(4\kappa)}{\kappa} && \text{for } \kappa \gg 1\end{aligned}\tag{A.8}$$

where $\sigma_T = (8\pi/3)(e^2/m_e c^2)^2$ is the Thomson cross section for the elastic scattering of an electromagnetic radiation by a free charged particle, as described by classical electromagnetism. In the two regimes, the energy-loss rate for the interaction of relativistic electrons with a mono-energetic photon field with energy ω_0 and number density n_{ph} , can be approximated as [32]:

$$\begin{aligned}-\frac{dE}{dt} &\simeq \frac{4}{3}\sigma_T c U_{rad} \varepsilon_e^2 && \text{for } \kappa \ll 1 \\ -\frac{dE}{dt} &\simeq \frac{3}{8}\frac{\sigma_T c n_{ph}}{\omega_0}(\ln 4\kappa - 11/6) && \text{for } \kappa \gg 1\end{aligned}\tag{A.9}$$

where $U_{rad} = \omega_0 n_{ph}$ is the radiation energy density. While in the Thomson regime the energy-loss rate is proportional to ε_e^2 , in the Klein-Nishima it is almost independent on the electron energy. This different dependence on the electron energy has an effect on the shape of the steady-state electron spectrum, yielding to a steeper electron spectrum for $\kappa \ll 1$, $dN/d\varepsilon_e \propto \varepsilon_e^{-(\Gamma+1)}$, and to a harder one in case of $\kappa \gg 1$, $dN/d\varepsilon_e \propto \varepsilon_e^{-(\Gamma-2)}$. Another consequence of the ε_e^2 dependence of the energy-loss rate, is that the Compton cooling time in Thomson regime decreases linearly with energy ($t_{cool} = E/(dE/dt)$). This means that, although the process proceeds with high efficiency over the whole gamma-ray energy domain thanks to the universal presence of the 2.7 K Cosmic Microwave Background (CMB, characterized by an energy density $U_{CMB} = 0.25 \text{ eV/cm}^{-3}$), it becomes especially effective at VHE.

In deep Klein-Nishima regime ($\kappa \gg 1$) a single interaction is sufficient to transfer a significant fraction of the electron energy to the photon. For a power-law energy spectrum of electrons with index Γ and an isotropic target photon distribution, the corresponding spectrum of the emitted gamma rays turns out to be steeper, i.e. $dN/d\varepsilon_\gamma \propto \varepsilon_\gamma^{-\alpha}(\ln(4\omega\varepsilon_\gamma) + \text{const})$ with $\alpha = \Gamma + 1$. In the Thomson regime ($\kappa \ll 1$) the average energy of the up-scattered photon is $\varepsilon_\gamma \simeq \omega\varepsilon_e^2$, thus only a fraction $\varepsilon_\gamma/\varepsilon_e \sim \kappa \ll 1$ of the primary electron is converted in photon energy. Assuming the electron power-law spectrum and the isotropic target radiation field, the resulting gamma-ray spectrum is still a power-law with photon index $\alpha = (\Gamma + 1)/2$ [32]. Therefore, in the Klein-Nishima regime the IC gamma-ray spectrum will be significantly steeper. Thus, even a power-law distribution of electrons will produce a gamma-ray spectrum with a break, due to the onset of the Klein-Nishima regime [111].

Absorption process: Photon-photon pair production

In this process, two photons produce an electron-positron pair, i.e. $\gamma\gamma \rightarrow e^+e^-$. The pair production process has a kinematic threshold given by:

$$\varepsilon_{\gamma 1}\varepsilon_{\gamma 2}(1 - \cos\theta) \geq 2\tag{A.10}$$

with $\varepsilon_{\gamma 1}$ and $\varepsilon_{\gamma 2}$ the energy of the two photons in units of $m_e c^2$ and θ the angle at which they collide (in the laboratory frame). It is an absorption process: it does not allow the escape of energetic gamma rays from compact objects and in this way it determines the *gamma-ray horizon* of the Universe. For example, the mean free path for a TeV gamma ray is of the order of several 100 Mpc, whereas for 1 PeV gamma ray it is only 8.5 kpc, which implies that all the objects beyond our Galaxy are not visible in PeV gamma rays. The parameter that characterizes gamma-ray absorption at photon-photon interactions in a source of size R is the so-called *optical depth*:

$$\tau(\varepsilon_\gamma) = \int_0^R \int_{\omega 1}^{\omega 2} \sigma_{\gamma\gamma}(\varepsilon_\gamma, \omega) N_{ph}(\omega, r) d\omega dr \quad \text{A.11}$$

where ω is the energy of the photon field, $\sigma_{\gamma\gamma}(\varepsilon_\gamma, \omega)$ the cross-section of the process and $N_{ph}(\omega, r)$ describes the spectral and spatial distribution of the target photon field in the source. As for the IC scattering, the cross-section $\sigma_{\gamma\gamma}$ depends only on the product of the primary photon energy ε_γ and ω , i.e. $s = \varepsilon_\gamma \omega$. It can be modeled as $\sigma_{\gamma\gamma} \simeq (2/3)\sigma_T \frac{\ln(s)}{s}$ for $s \gg 1$, while in the non-relativistic regime it can be approximated as $\sigma_{\gamma\gamma} \simeq (1/2)\sigma_T (s - 1)^{3/2}$, approaching zero as soon as $s \rightarrow 1$ [32].

This absorption process is significant in environments with dense radiation field but also when the photons travel long distances in a relatively faint ambient radiation field. Gamma rays travelling from remote extragalactic objects interact with the Extragalactic Background Light (EBL), the diffuse radiation field created during the star and galaxy formation history of the Universe. This background photon field, as well as the CMB, is a function of the red-shift z , resulting in more significant absorption for cosmologically distant objects, due to the denser ($n_{ph} \propto (1+z)^3$) and more energetic ($T \propto 1+z$) radiation fields. The energy dependent gamma-ray attenuation can be calculated as $\exp[-\tau(\varepsilon_\gamma, z)]$, where the red-shift dependent optical depth in Eq. [A.11] has to be scaled to the specific red-shift of the source z_{src} , according to the factor $(c/H_0) \int_0^{z_{src}} (1+z)^{-2} dz$, where H_0 is the Hubble constant [107]. The attenuation factor at different red-shifts is shown in Fig. A.1.

The absorption process is tightly coupled with IC scattering. If the radiation pressure dominates over the magnetic field pressure, the photon-photon pair production and the IC scattering work together, supporting the effective transport of high energy radiation via electromagnetic cascades. In particular, for an intergalactic magnetic field in the range $10^{-7} - 10^{-12}$ G, the synchrotron cooling of the electrons is negligible but at the same time these secondary electrons are isotropised before they interact with the ambient photons. Under these conditions, the development of the electromagnetic cascades initiated by the interaction of primary TeV photons with the EBL, lead to the formation of extended isotropic (not beamed) electron-positron halos around the powerful extragalactic object [107]. These giant structures are unavoidably formed around any extragalactic VHE source [36] and contain unique information about the flux of the EBL and its evolution in the past.

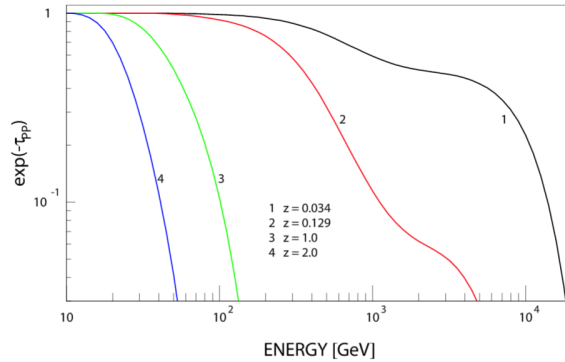


Figure A.1: The attenuation factor $\exp[-\tau_{pp}]$ ($\tau_{pp} \equiv \tau(\varepsilon_\gamma, z)$) for gamma rays emitted from sources at different redshifts as a function of energy and for the EBL model proposed in [163]. Extracted from [107].

A.3 Interactions in magnetic field

Production process: Synchrotron emission

Synchrotron emission is the radiation emitted by a charged accelerated particle placed in a magnetic field. This radiation may account for the non-thermal emission in many astrophysical sources, from radio up to gamma-ray energies.

High-energy charged particles gyrating along the magnetic field lines suffer a centripetal acceleration, giving rise to synchrotron radiation. The classical treatment of this mechanism provides an accurate description of the process, as long as the condition:

$$\chi = \frac{E}{m_e c^2} \frac{B}{B_{cr}} \ll 1 \quad (\text{A.12})$$

is verified, with $B_{cr} = m_e^2 c^3 / e \hbar \sim 10^{13}$ G the critical value of the magnetic field relevant to quantum effects, and m and E the mass and the energy of the charged particle in the magnetic field of strength B . Under this assumption, the synchrotron cooling time for this particle is:

$$t_{cool, sy} = 6\pi \left(\frac{m}{m_e} \right)^3 \frac{m_e c^2}{c \sigma_T B^2} \frac{m c^2}{E} \quad (\text{A.13})$$

and the characteristic energy of the synchrotron radiation due to the same charged particle can be written as:

$$E_c = h\nu_c = \frac{3}{4\pi} \frac{h e B \sin \alpha E^2}{m^3 c^5} \quad (\text{A.14})$$

where α is the so called pitch angle, i.e. the angle between the particle trajectory and the magnetic field line. The spectral distribution of photons radiated by a single particle of energy E in an isotropic magnetic field is given by:

$$P_{sy}(E, \varepsilon) = \frac{\sqrt{2}}{h} \frac{e^3 B}{m c^2} F(x) \quad (\text{A.15})$$

where $F(x) = x \int_x^\infty K_{5/3}(\xi) d\xi$ ($K_{5/3}$ the modified Bessel function of order 5/3), $x = \varepsilon/E_c$ and ε the energy of the emitted radiation. This synchrotron

emissivity $P_{sy}(E, \varepsilon)$ is characterized by a peak in correspondence of $\varepsilon \simeq 0.29E_c$, with a sharp drop at higher energies. The frequency of synchrotron radiation is directly related to the strength of the magnetic field and the energy of the charged particles affected by the field. Accordingly, the stronger the magnetic field and the higher the energy of the particles, the greater the frequency of the emitted radiation. Moreover, the dependence of E_c and $t_{cool, sy}$ on the charged particle mass m implies that the process is much more efficient for electrons than for heavier particles. For instance, in case of a proton, the characteristic energy would be $(m_p/m_e)^3 \simeq 6 \cdot 10^9$ times lower than for electrons and the cooling time $(m_p/m_e)^4 \simeq 10^{13}$ times slower.

The energy-loss rate of electrons emitting synchrotron radiation is given by:

$$-\frac{dE}{dt} = \frac{4}{3}\sigma_T c U_B \left(\frac{E}{m_e c^2}\right)^2 \quad \boxed{\text{A.16}}$$

where $U_B = B^2/(8\pi)$ is the magnetic field energy density. The comparison of Eq. [A.9] and Eq. [A.16] shows that the energy loss rate due to IC in Thomson regime and to synchrotron radiation differs only by the field density term, i.e. U_{rad} and U_B , respectively. In environments where the magnetic field energy density U_B is significantly larger than the energy density of the radiation field U_{rad} , synchrotron radiation is efficiently emitted the relativistic electron. Typically, such a synchrotron radiation does not extend beyond X-ray energies. However, in the so-called *extreme accelerators*, where the maximum rate allowed by classical electrodynamics [31] supports the particle acceleration, the synchrotron radiation can become the main channel of gamma-ray radiation. This effect is especially expected in highly magnetized environments moving at relativistic speed towards the observer [29], as in the case of blazars (see §B.2).

As for the IC in Thomson regime, the steady-state distribution of parent particles is steeper if the electrons are cooled by synchrotron losses: for an initial power-law energy distribution of electrons with index Γ , the cooled spectrum will exhibit an index $\Gamma + 1$. Also the emitted gamma-ray radiation will show a power-law energy distribution, with photon index $\alpha = (\Gamma + 1)/2$.

Production process: curvature radiation

Similar to the synchrotron radiation, is the curvature radiation, that is generated when relativistic charged particles move along curved magnetic field lines [158]. In general, the cooling of the accelerated particles in strong magnetic fields is determined by the the curvature of their trajectory. In case of curved magnetic field lines, the trajectories of the charged particles have a structure defined by the helicoidal motion around the magnetic field lines and the curvature of the field itself. If the main contributor is the curvature of the helix, the radiation is defined by the strength of the magnetic field and the synchrotron radiation is emitted, as described by Eq. [A.14]. On the other hand, if the helix is stretched, the main contribution to the radiation is due to the curvature of the field lines [139]. This is the case of the curvature radi-

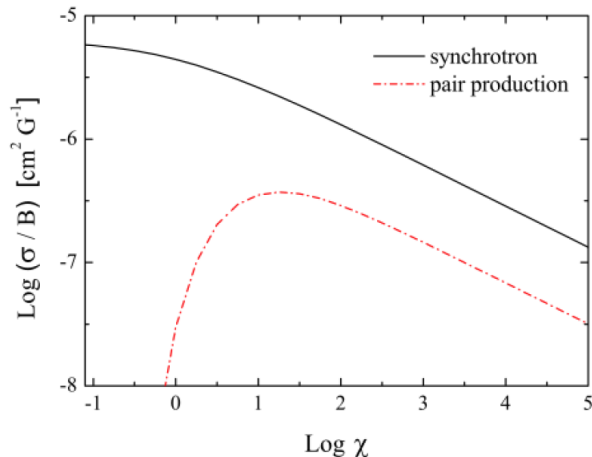


Figure A.2: Interaction probabilities of synchrotron radiation and magnetic pair production as a function of χ , defined in Eq. [A.12]. Extracted from [32].

ation. In this scenario, the particles radiate photons in the direction of their movement with energies of the order of $E_\gamma \simeq (3/2)(\hbar c \gamma^3 / \rho_c)$, where γ is the Lorentz factor of the charged relativistic particle and ρ_c is the curvature of the magnetic field lines. This emission mechanism is relevant in environments with extreme magnetic field intensities, such as in the vicinity of pulsars (see §B.1). In the pulsar magnetosphere the magnetic field is so strong that electrons and positrons are constrained to move parallel to the magnetic field lines with almost zero pitch angle.

Absorption process: Magnetic pair production

In certain astrophysical environments the synchrotron radiation can occur near the quantum thresholds. Whether the condition in Eq. [A.12] is not fulfilled, the quantum regime takes place and the production of electron-positron pairs by HE photons in the magnetic field B becomes important through the process $\gamma B \rightarrow e^+e^-$. In Fig. A.2 the interaction probability of the synchrotron radiation and magnetic pair production is shown as a function of χ , defined in Eq. [A.12]. For $\chi \ll 1$, when the classical regime holds, the synchrotron probability is almost constant while the pair production suddenly drops. For $\chi > 10$, the magnetic pair production starts to play a role, even though the synchrotron radiation is always several times larger. Under this latter condition, an electron-photon cascade can be generated by the combination of the two processes, as long as the surrounding magnetic field is very intense and the mean free paths of gamma-rays and electrons are smaller than the extension of the source.

A.4 Interactions in matter field

Production processes: Bremsstrahlung emission

Bremsstrahlung gamma-ray emission is produced as a charged particle interacts with an ion or a nucleus: the trajectory of the incident charged particle is changed by the electric field of the nucleus, and a photon is emitted. The emission probability is proportional to the inverse square of the particle mass, i.e. $\sigma_{br} \propto (e^2/m)^2$. Therefore, electron bremsstrahlung is strongly favored with respect to proton induced bremsstrahlung emission. At energies of a few MeV this process is still a relatively small factor. However, as the energy is increased, the probability of bremsstrahlung quickly shoots up, so that at a few tens of MeV the loss of energy by radiation starts to be greater than the collision-ionization loss, which dominates at lower energies [147]. Bremsstrahlung losses are basically catastrophic and the high energy electrons radiate almost all their energy in one or two photons, which mostly contributes to the gamma-ray radiation in the sub-TeV domain. Nevertheless, in order to calculate the evolution of the energy distribution of the parent population, it is convenient to introduce the so-called average energy-loss rate. For an electron with energy E interacting with the electric field of a proton having mass m_p in a gas with number density n , a continuous average energy loss may be computed as:

$$-\frac{dE}{dt} = \left(\frac{cm_p n}{X_0} \right) E \quad (\text{A.17})$$

where $X_0 = 7/9(1/n\sigma_{br})$ is the average distance over which the electron loses the main fraction of its energy due to bremsstrahlung. Correspondingly, the cooling time of the electrons is:

$$t_{cool,br} \simeq 4 \cdot 10^7 (n/\text{cm}^{-3}) \text{ yr} \quad (\text{A.18})$$

The fact that the cooling time is independent on energy, implies that bremsstrahlung losses do not change the original electron energy distribution. Therefore, for an initial power-law of the electrons with index Γ , the steady-state spectrum of the same electron population is still given by a power-law with index Γ . Also the shape of the gamma rays emitted as bremsstrahlung radiation is a power-law with the same photon index Γ . Thus, as long as the bremsstrahlung dominates over the ionization losses¹, the bremsstrahlung gamma rays simply reproduce the parent particle spectral profile.

Production processes: π^0 decay

The second mechanism that operates efficiently in dense and extended gaseous environments is related to hadronic interactions. Relativistic protons and nuclei generate gamma-ray photons through inelastic collisions with ambient gas and the subsequent production and decay of secondary particles:

$$pp \longrightarrow \pi^\pm, \pi^0, K^\pm, K^0, p, n, \dots \quad (\text{A.19})$$

¹In a hydrogen gas, the critical energy for the bremsstrahlung to dominate over ionization process is about 350 MeV.

The π^0 decay provide the main channel of conversion of the proton kinetic energy into high energy gamma rays. When the proton's kinetic energy exceeds a minimum energy $E_{th} = 2m_\pi c^2(1 + m_\pi/4m_p) \sim 280 \text{ MeV}$ (with $m_\pi = 134.97 \text{ MeV}$ mass of the neutral pion), then it may produce one π^0 which in turn generates two high energy photons: $\pi^0 \rightarrow \gamma\gamma$. The cooling time of relativistic protons due to inelastic proton-proton interactions in a medium with number density n can be approximated as:

$$t_{cool,pp} = \frac{1}{0.5n\sigma_{pp}c} \simeq 5 \cdot 10^7 (n/\text{cm}^{-3}) \text{ yr} \quad \text{(A.20)}$$

where σ_{pp} is the inelastic proton-proton cross section for which an average value of 40 mb can be assumed at VHE [30]. Cooling plays a relatively minor role in sources actively accelerating particles, since even in the case of a typical Galactic density ($n = 1 \text{ cm}^{-3}$) the cooling time is of the order of 10^7 years [111]. Moreover, this cooling time is almost energy-independent and therefore the steady-state spectrum of parent particles remains unchanged. Consequently, the gamma-ray spectrum essentially repeats the spectrum of the parent protons, scaled by a factor ~ 10 towards lower energies² and with a peculiar feature which uniquely identifies the gamma rays as originated from the π^0 decay: the so called *pion-decay bump*. This bump corresponds to the maximum in the gamma-ray spectrum at $E_\gamma = m_\pi c^2/2 \simeq 67.5 \text{ MeV}$. It results from the $\pi^0 \rightarrow \gamma\gamma$ decay kinematics and it does not depend on the energy distribution of π^0 mesons, and consequently of the parent protons. Therefore, the detection of this bump allows a direct measurement of the spectrum of cosmic protons at the source [170].

The π^0 decay is (almost) the only hadronic process relevant to gamma-ray production. Therefore it represents a unique channel to detect accelerated protons and nuclei, even though its identification might be difficult, due to the fact that its typical energy domain presents an overlap with the IC gamma-ray photons. Nevertheless, together with the π^0 decay, the decay of the charged pions π^\pm , produces neutrinos. For instance, for a π^- one would expect firstly the meson decay $\pi^- \rightarrow \mu^- \bar{\nu}_\mu$ and then the consequent muon decay $\mu^- \rightarrow e^- \bar{\nu}_e \nu_\mu$ (the charge-conjugate reaction holds for the π^+ meson). These neutrinos would exhibit spectra quite similar to the spectrum of the gamma rays produced at the π^0 decay [32]. The discovery of neutrino and gamma-ray correlated spectra would be the strongest indications of the presence of hadronic acceleration mechanisms.

Absorption process: Bethe-Heitler pair production

The counterpart process of the bremsstrahlung is the so called Bethe-Heitler pair production, in which an electron-positron pair is produced through photon interaction with matter field: $\gamma X \rightarrow e^+e^-X$, where X stands for an atom, an ion or a free electron. The pair production has many similarities with the bremsstrahlung process and an extensive treatment can be found

²On average, a proton with energy E would produce a gamma-ray photon with energy $E/10$.

e.g. in [122]. The process becomes important only in specific astrophysical environments, e.g. very dense shell surrounding particle accelerators, while the bremsstrahlung mechanism has many applications in several astrophysical scenarios, especially at intermediate energies. Nevertheless, the two processes together become interesting in the context of electromagnetic cascade development in optically thick environments [30].

An interesting astrophysical scenario where the Bethe-Heitler pair production plays an important role is in the context of distant extragalactic gamma-ray emitters where cosmic protons with energies above 10^{19} eV are expected to be produced and accelerated. Especially at high red-shifts, due to the denser and more energetic photon field, the interaction of protons with the CMB via Bethe-Heitler pair production starts to be important and a considerable fraction of the proton energy is converted in electrons. This results in a dense halo of Bethe-Heitler electrons around the source and, for a intergalactic magnetic field of the order of $B \sim 10^{-6}$ G (comparable to the field of galaxy clusters), in the consequent production of X-ray synchrotron radiation [164].

A.5 Dark Matter annihilation

Another possible production mechanism of gamma-ray photons is related to dark matter (DM) annihilation processes. The DM existence in the Universe was first proposed by Zwicky in the 30's to explain the dynamics of the Coma galaxy cluster where the observed matter emitting electromagnetic radiation was insufficient to provide gravitational stability [194]. Evidence of DM now exists on many scales; nevertheless, the DM nature is still unknown. The most widely accepted hypothesis on the form of DM is that it is composed of weakly interacting massive particles (WIMPs), left as a relic component by the thermal free-out of the early Universe. After the freeze-out the DM particles became too diluted to annihilate in appreciable numbers and the thermal energies were too low to produce them. Nevertheless, in regions with high DM densities (as the center of the galaxies or the galaxy clusters), the DM particles can eventually self-annihilate and produce standard model particles. Gamma-ray photons are expected to be part of the annihilation products and their flux within a solid angle $\Delta\Omega$ can be quantitatively described as:

$$\frac{d\Phi_\gamma(\Delta\Omega, E_\gamma)}{dE_\gamma} = B_F \frac{1}{4\pi} \underbrace{\frac{\langle \sigma_{ann}\nu \rangle}{2m_{WIMP}^2} \sum_i BR_i \frac{dN_\gamma^i}{dE_\gamma}}_{\text{Particle Physics}} \cdot \underbrace{J(\Delta\Omega)}_{\text{Astrophysics}} \quad (\text{A.21})$$

where, in the *particle physics* term, $\langle \sigma_{ann}\nu \rangle$ is the velocity-averaged annihilation cross-section, m_{WIMP} is the mass of the DM particle and $\sum_i BR_i (dN_\gamma^i/dE_\gamma)$ is the sum over all the annihilation processes of each individual photon flux i multiplied by the corresponding branching-ratio BR_i . The *astrophysics* term J corresponds to the line-of-sight integral of the square of the DM density. The boost factor B_F accounts for all the possible contributions which could increase the gamma-ray flux, such as inhomogeneities in the DM profile density [101].

The indirect DM detection through a gamma-ray emission is basically expected in two ways: (i) a continuum signal from annihilation into other particles that eventually produce gamma rays; (ii) a line signal from DM annihilating directly to γX , being X another neutral particle. The line-like emission is especially important due its unique “smoking gun” signature. However, this production channel is loop-suppressed by a factor α_e^2 (α_e the fine structure constant), since the electrically neutral DM particle does not directly couple to photons. The continuum signal, characterized by a smooth spectrum with an exponential cutoff at the mass of the DM particle, is therefore expected to be more significant [110].

B

Very high energy gamma-ray sources

Gamma-ray astronomy has revealed several categories of objects whose emission is dominated by non-thermal processes. In the following, the main categories are described, divided in two major classes: galactic and extragalactic gamma-ray emitters.

B.1 Galactic sources

B.1.1 Pulsars and pulsar wind nebula

Pulsars are rapidly rotating, magnetized neutron stars emitting a beam of electromagnetic radiation that can be observed only when the beam of emission is pointing towards the Earth. The rotation period, and thus the interval between observed pulses, is very regular (from milliseconds up to few seconds) and it slows down over time as electromagnetic radiation is emitted. Pulsars can emit in the whole electromagnetic spectrum; the first discovered pulsar (PSR 1919+21) was observed by a radio detector in 1967 by Hewish and Bell. A large collection of pulsars has been detected in the HE domain (~ 150 [18]), but only for one of them, the Crab pulsar [69, 74, 62], a TeV radiation component has been observed¹.

The HE and VHE gamma-ray radiation is thought to be produced in three physically separated regions: the pulsar magnetosphere, the unshocked relativistic wind, and the synchrotron nebula, as schematically illustrated in Fig. B.1. The pulsar magnetosphere is limited by the light cylinder, the radius of which corresponds to the distance at which the pulsar co-rotating velocity equals the speed of light. In this region, primary gamma rays are thought to be produced as curvature radiation of high energy electrons in the extremely intense magnetic field of the pulsar. These photons generate through pair production processes a dense electron-positron plasma streaming along the magnetic field lines and initiate an electromagnetic cascade. Close to the light cylinder, a relativistic outflow of a dense electron-positron plasma is originated. This electron-positron wind carries away much of the rotational energy lost

¹Recently, the H.E.S.S. telescope has revealed a regular pulsed signal also from the Vela pulsar, but no TeV component has been observed, since the reconstructed energies of the gamma rays are in the range of 30 GeV. The press release of newly announcement is available here: <http://www.nanowerk.com/news2/space/newsid=36373.php>

Radiation from a **Pulsar-wind-nebula** complex

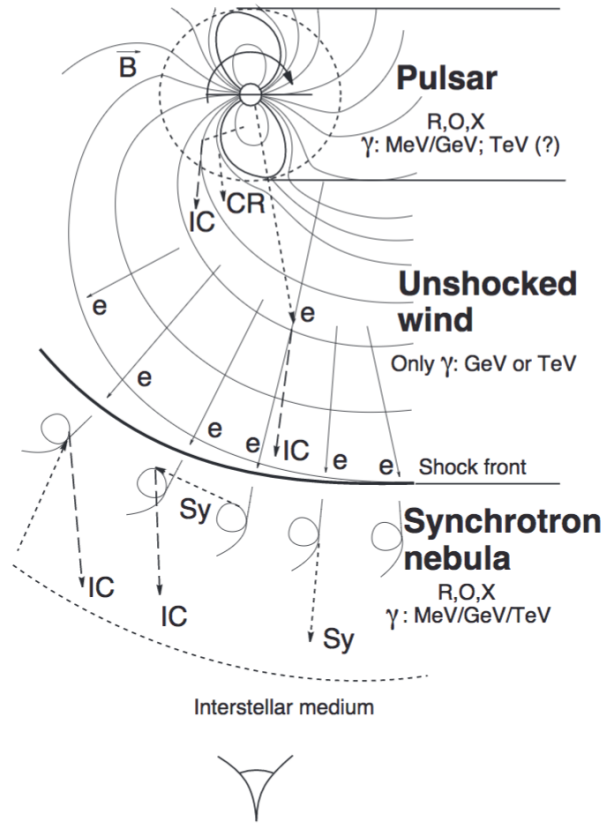


Figure B.1: Schematic illustration of the three regions that can emit non-thermal HE and VHE gamma rays in the proximity of a pulsar: (i) the pulsar magnetosphere, where the gamma rays are thought to be produced mainly through curvature radiation of high energy electrons, (ii) the wind of cold relativistic plasma which emits gamma rays through the IC mechanism, and (iii) the extended non-thermal nebula surrounding the pulsar (the pulsar wind nebula (PWN) or *plerion*) where relativistic particles are subsequently accelerated and cooled down through synchrotron and IC processes. Extracted from [33].

by the pulsar. The termination of the pulsar wind in the interstellar medium results in strong shocks which lead to the formation of synchrotron and IC nebula around the pulsar [33]. This outer extended region of non-thermal emission is called pulsar wind nebula (PWN) or *plerion*.

One of the open questions in the theory of gamma-ray pulsars is where exactly the primary gamma rays are originated. It is not yet clear if the emission occurs close to the neutron star (*polar cap model* [75, 94]) or farther in the magnetosphere (*slot-gap* [76] and *outer gap* models [92, 165, 127]). The detection of the pulsed signal above 25 GeV from the Crab performed by the MAGIC telescope [68] indicates that the emission happens far out in the magnetosphere and excludes the polar cap model, which predicts very sharp cutoff around 10 GeV. However, the pulsar magnetosphere is not the

only region of the pulsar from which we should expect pulsed emission: recent models explain the VHE pulsed emission from the Crab as produced in the cold ultra-relativistic wind [34].

The hardship of observed pulsars in the TeV sky is compensated by the wealth of PWN detected in this energy domain: at TeV energies, the largest number of detected galactic sources are PWN (see Fig. 1.1). The brightest persistent point-like TeV gamma-ray source in the sky, the Crab Nebula [38, 42, 65, 152], is a PWN and it has become the standard candle for cross-calibration of different detectors [35].

B.1.2 Supernova remnants

The catastrophic explosion of a star is known as supernova. The structure resulting from the explosion of the dying star is called supernova remnant (SNR). SNRs can be classified into three broad categories: *plerionic* (that are the PWN explained in previous section), *shell-like* and *composite*. The third type of SNR is a mixture of the other two classes, with a pulsar powered PWN surrounded by an expanding shell. For example, SNR G 0.9+0.1 is a representative of the *composite* class [40]. Here the *shell-like* type of SNR will be discussed.

The energy liberated in the supernova explosion is deposited in the envelope of the star which is ejected and heated to a very high temperature. This expanding structure is highly supersonic and a shock front is formed ahead. The shock wave heats any interstellar material it encounters, thus producing a big shell of hot material. For decades, these objects have been believed to be the principal factories of galactic cosmic rays (see e.g. [118]), producing HE and VHE gamma rays through hadronic interactions. The first *phenomenological* argument in support of this theory is based on the fact that SNRs are energetically suitable candidates for the acceleration of cosmic rays. The required power to sustain the observed density of galactic cosmic rays at the level of 1 eV/cm^{-3} corresponds to about the 10% of the total mechanical energy released by supernova explosions in our Galaxy. The second *theoretical* argument relies on the diffuse shock acceleration (DSA) theory (see e.g. [150]) applied to SNRs [35]. Within DSA framework, it is possible to demonstrate that the strong shocks in SNRs can provide acceleration efficiencies (i.e. the fraction of mechanical energy of the shock transferred to the non-thermal particles) as large as 10% and, once the propagation effects in the Galaxy are properly taken into account, can explain the observed slope of cosmic ray spectrum up to $\sim 1 \text{ PeV}$, the so called *knee* of the galactic cosmic-ray energy distribution. Nevertheless, the particle acceleration in diffusive shocks has to be fast in order to achieve PeV energies before the SNR enters the *Sedov phase*. This phase corresponds to the moment when the mass of the swept-up matter becomes comparable with the mass of the ejecta. Consequently the shock slows down, becoming unable to confine the highest energy cosmic rays [103], and it is not possible to further increase the maximum energy. For this reason, even if the SNR visibility in TeV gamma rays covers a large fraction

of the source lifetime ($\sim 10^4$ years), the useful time to observe the PeV particle before their escape from the SNR is much shorter, of the order of several hundreds years.

The escape of the high energy particles might explain the spectral break around 20 GeV in the energy distribution of the mid-age ($> 10^4$ years) SNR IC 443. For this remnant the characteristic *pion-bump* in the HE domain has been detected [22], demonstrating that the gamma-ray radiation in the GeV range is due to the π^0 decay and therefore proving the remnant as effective cosmic protons accelerator. Nevertheless, the observations in the TeV band show a soft spectral profile with a maximum energy far from the knee of the cosmic-ray spectrum [54, 13]. In this respect young SNRs are much more important, being the best candidates as effective source of VHE gamma rays.

The most prominent of the young SNRs (< 1000 years) are RX J1713.7-3946 [44], Tycho's SNR [14], and Cas A [55]. While Tycho and Cas A seem to match the expectations from an hadronic scenario, the underlying nature of the accelerated particles in case of RX J1713.7-394 is matter of active debate. RX J1713.7-394 is the brightest object of its class at TeV energies and its spectral shape does not exclude a leptonic origin for the gamma-ray radiation, due to the lack of thermal X-ray emission and to the rather hard photon index in the GeV band (see e.g. [111] for a complete discussion on this topic). In order to justify the hadronic model, a complex environment around the remnant has to be assumed, with a non-uniform (clumpy) structure of gas density around it [193].

B.1.3 Supernova remnants interacting with molecular clouds

In general, the gamma-ray emission produced at the interaction of accelerated particles with diffuse gas, clumps, and clouds surrounding a central engine offers a close-up view of the process of cosmic ray acceleration at shocks (see §A.4 for the details about the π^0 decay production mechanism). This is especially true in case of SNRs interacting with interstellar molecular clouds (MC): due to their large masses, MC should appear as discrete gamma-ray sources, the morphology of which should be resolvable with current systems of IACT telescopes. The study of the SNR/MC associations is of primary importance in order to understand the acceleration of particles at SNR shocks, their escape from the acceleration site, and their propagation in the interstellar medium. These studies are extremely attractive in order to test the SNR paradigm for the origin of Galactic cosmic rays, verifying whether or not SNRs are proton PeVatron and placing constraints on the cosmic-ray diffusion coefficient [112, 113].

The old-age SNR W28, surrounded by gamma-ray bright MCs constitutes an ideal system for this kind of studies. Gamma rays from the vicinity of this SNR have been detected by the H.E.S.S. and Fermi collaborations [45, 6]. The VHE gamma-ray emission positionally coincide well with molecular clouds and this VHE/MC association could indicate a hadronic origin for the VHE sources in the W 28 field.

B.1.4 Compact binary systems

Binary systems are found very often in astrophysical environments: a majority of 70% of all stars in our galaxy are part of binary systems [95]. They consist of a compact object, like a neutron star or a black hole, orbiting a gravitationally bound massive star. Many questions on gamma-ray emission from these systems are still unanswered. Particle acceleration can be linked either to the termination shocks of the pulsar wind or to the collimated jet of plasma created by the accretion of material into the black hole. In these conditions, the production of gamma rays can be very effective, due to the dense target of material in form of optical photons or gas provided by the companion star [35]. In this sense, these systems can offer a unique chance to explore cosmic accelerators.

The so called *gamma-ray binary systems* are those binary systems whose non-thermal radiative output is dominated by gamma rays. They consist of a compact object, e.g. young pulsars in high radiation field environment, and a massive O- or B-type star. They exhibit flux variability and often periodicity at all wavelengths. A well established examples of this kind of binary system is LS I +61 30 [50, 58, 12], a regular (~ 26.5 days of periodicity) gamma-ray emitter in the Northern sky.

Systems in which the compact object is formed by a (few solar masses) black hole are usually called *micro-quasar*. The physics of micro-quasar in our own Galaxy resembles the physics of super-massive black holes in distant active galaxies, but on much smaller time scales [155]. The formation, the internal structure, and the evolution of collimated streams of relativistic plasma are still not fully understood and micro-quasars can provide an insight into the mechanisms at play in these relativistic outflows. HE gamma-ray emission has been reported from at least two such systems, Cyg X-1 [57, 162, 166] and Cyg X-3 [4, 172]. However, a detection of VHE gamma-ray emission at the 5σ level is still lacking [90].

B.1.5 The Galactic Center and the Galactic ridge

The Galactic Center (GC) is the closest example of a galactic nucleus, representing an attractive laboratory for fundamental astrophysics. It has been observed in VHE gamma rays by all the current IACT experiments: VERITAS [141], MAGIC [52] and H.E.S.S. [39]. All these gamma-ray observations revealed a bright and complex gamma-ray morphology. At the center of the GC region, a strong point-like VHE gamma-ray source (HESS J1745-290) is observed. Despite the unprecedented level of accuracy achieved in the measurement of the source position, HESS J1745-290 remains unidentified [15]: within the error (a circle of radius $13''$), its position results coincident both with position of the $3 \cdot 10^6 M_{\odot}$ supermassive black hole (SMBH) Srg A* [49] and with the PWN G359.96-0.04 [184]. Among other possibilities considered, it has been suggested that the TeV signal from the inner 10 pc of our Galaxy might correspond to a spike of annihilating dark matter [83] or that it might have a diffuse origin, peaking towards the direction of the GC due

to the larger concentration of gas and accelerated particles [49]. Further observations performed by H.E.S.S. led to the discovery of a *ridge* of diffuse gamma-ray emission extending along the Galactic plane for about 2 deg in Galactic longitude. This extended gamma-ray component turned out to be spatially correlated with a complex of giant molecular clouds in the central 200 pc of the Milky Way [41]. The close correlation between the morphology of gamma-ray ridge and the density of target molecular clouds emerged as a strong indication for the origin of this VHE emission, suggesting the presence of a powerful cosmic-ray accelerator in the GC. In this scenario, the gamma rays would be the product of the interaction of the accelerated protons with the molecular gas, leading to the creation of neutral pions.

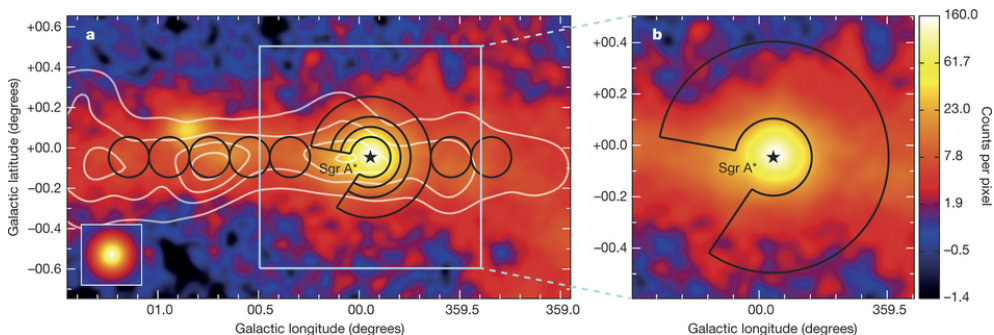


Figure B.2: Excess counts map of the diffuse VHE gamma-ray in the GC region. The black star indicates the position of the SMBH Srg A*. The white contours show the density distribution of the molecular gas, as traced by the CS line emission. The black contours correspond to the regions used to extract the profile of the energy density of the cosmic rays along the Galactic plane. Extracted from [11].

In general, the central 200 pc of the Milky-Way is a very rich environment and therefore the acceleration and the gamma-ray production is expected to be abundant in this region. The VHE emission is dominated by the strong HESS J1745-290 source and by HESS J1747-281, associated with the composite SNR G0.9+0.1 [40]. The large photon statistics accumulated by H.E.S.S. during over a decade of observations, recently led to the detection of a new gamma-ray source (HESS J1746-285) in the inner 50 pc region [144], positionally consistent with the PWN G0.13-0.13 [183]. Moreover, this huge data sample, made possible to study in more depth the nature and behavior of the ridge emission, in order to extract information about the proton accelerator into the central molecular zone [11]. In Fig. B.2 the excess counts map of the ridge emission is shown, together with the position of Srg A* (black star), the density distribution of the molecular gas (white contours) and the regions used to infer the cosmic rays energy density throughout the central molecular zone (black contours). The obtained cosmic-ray profile follows a $1/r$ dependence, which indicates a continuous injection (lasting for $\sim 10^4$ years) of cosmic protons into the central molecular zone due to the presence of a central accelerator. Moreover, the gamma-ray spectrum of the diffuse emission around the GC shows a power-law spectrum of index 2.3 and extends up to 50 TeV with

no evidence of a spectral cutoff. The derivation of such hard power-law spectrum of gamma rays produced through hadronic interactions, implies that the spectrum of the parent protons should extend up to and beyond PeV energies, corresponding to the first detection of a Galactic PeVatron [11].

B.2 Extragalactic sources

B.2.1 Active galactic nuclei

Active galactic nuclei (AGN) are compact extragalactic objects that emit time-variable radiation across the entire electromagnetic spectrum up to multi-TeV energies, with fluctuations on time-scales from many years down to a few minutes. They are divided in two types: those that have intense radio emission, so-called *radio-loud* AGNs, and those that don't have it, called *radio-quiet* AGNs. The radio-loud AGNs are the ones that also emit VHE gamma rays. For both types, the presently accepted picture of AGNs considers a SMBH ($\sim 10^6 M_\odot - 10^{10} M_\odot$) located in the center of the host galaxy, whose gravitational potential energy is the ultimate source of the AGN luminosity. An accretion disk is formed around the SMBH, where the galaxy gas and star-like objects are pulled. The hot plasma accretion disk is surrounded by a dusty torus which is created in the equatorial plane that, depending on the viewing angle, might prevent the observation of the central region. Whether

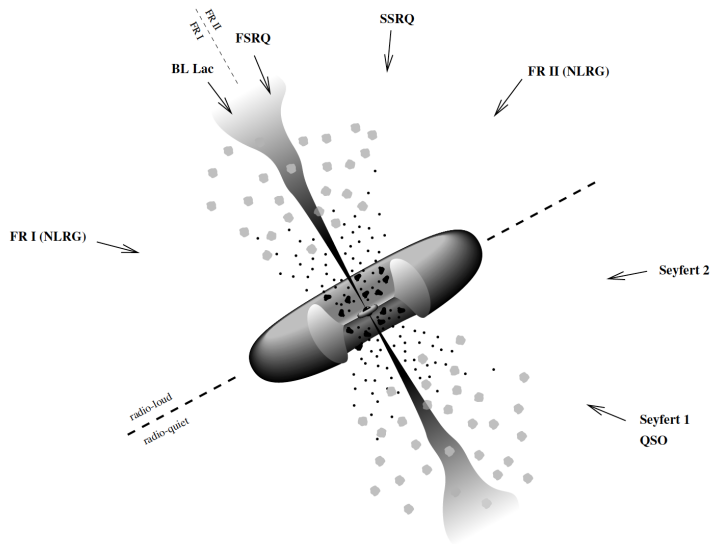


Figure B.3: Schematic illustration of the unified scheme of the AGNs. At the center, the SMBH works as a powerful engine and accretes matter forming a disk of hot plasma. Particle acceleration takes place throughout the entire jets extending up to thousands of kpc, i.e. well beyond the host galaxy. The majority of the gamma-ray emitting AGNs are the blazars, which are AGNs with jets pointing close to the line of sight. Extracted from [177].

the accretion rates are high enough, a pair of opposite jets of ultra-relativistic

moving plasma emerge from the polar regions of the system. Sometimes large radio lobes are seen close to the outer end of the jet. Particles in the jets stream outward at very high velocities, relativistically beaming the radiation produced inside in the forward direction. The relativistic beaming has an effect that the observed flux density is Doppler-boosted by a factor δ^4 with respect to the emitted one, i.e. $\mathcal{F}^{obs} = \delta^4 \mathcal{F}$, where $\delta = [\gamma(1 - \beta \cos \theta)]^{-1}$ is the Doppler factor, with β the bulk velocity in units of the speed of light, γ the corresponding Lorentz factor and θ the angle between the velocity vector and the line of sight.

The current classification of this source population is based on the pointing direction of the object rather than by intrinsic physical properties [177], as schematically illustrated in Fig. B.3. When the relativistic jet-axis are close to the line of sight (so-called *blazar*), the Doppler enhancement of the flux combined with the fortunate orientation of the beams towards the observer, makes these objects efficient emitters of multi-wavelength electromagnetic radiation, from radio to gamma rays. Blazars are divided in two sub-populations: the *flat-spectrum radio quasars* (FSRQ), with broad strong optical emission lines, and the *BL Lacertae* (BL Lac), with weaker emission lines. Two well established examples of BL Lac objects emitting in the TeV domain are: Markarian 501 (redshift $z = 0.034$) [66, 132] and Markarian 421 (redshift $z = 0.031$), the latter being characterized by a highly variable flux, showing flares with a flux up to an order of magnitude larger than the Crab Nebula flux [114, 56]. A recently discovered FSRQ object is PKS 1441+25 [156]. This detection is extremely interesting since PKS 1441+25 is the most distant blazar detected by TeV experiments, with its redshift of $z = 0.939$, providing competitive constraints on the EBL models. At present, the detection of TeV gamma rays from blazars with redshift $z \geq 1$ is lacking, due to the severe absorption by the background radiation field. Nevertheless, in principle, a TeV signal might be detected even from sources beyond $z = 1$ if the observed gamma rays are secondary photons produced by protons with energies $10^{17} - 10^{19}$ eV originating in the blazar jet and propagating over cosmological distances almost rectilinearly. These very energetic protons can effectively generate secondary gamma rays along the line of sight through interactions with CMB and EBL, therefore opening an interesting scenario for the detection extremely distant ($z \geq 1$) blazars [37].

Blazars are not the only extragalactic objects capable of VHE emission. With the detection of nearby *radio galaxies* (RG), e.g. M 87 [84, 61], Centaurus A [46], IC 310 [64], a new population of AGNs is now emerging as an effective class of VHE gamma-ray emitters [145]. RGs are AGNs with relativistic jets oriented at intermediate to larger angles with respect to the line of sight, therefore their radiation is not amplified by relativistic beaming. Their observations may reveal non-standard processes able to produce high energy particles within the central active engine and the extended lobes.

B.2.2 Gamma-ray bursts

Gamma-ray bursts (GRBs) are the brightest explosions in the detectable Universe, visible to high redshift, and thought to be the signature of black hole birth. These highly-relativistic bursts are transient events, occurring a few times per day in the distant extragalactic sky. They may be generated during the collapse of a massive star (*long GRBs*, lasting few minutes) or via a merger event (*short GRBs*, lasting few seconds) [116]. Although the two families of GRBs are known to have different progenitors, the acceleration mechanism that produces the relativistic particles is most likely independent of the progenitor of the event. The leading paradigm for the current understanding of GRBs is the so-called *fireball model* (see e.g. [153]). This model describes the physics of the GRBs as due to a central compact engine (either a collapsing massive star or the merger of two compact objects) which releases a large amount of energy ($\sim 10^{51} - 10^{54}$ erg) on very short timescales (tens of seconds or less). This sudden and extremely intense energy release would result in a relativistic blast wave (the *fireball*) consisting of e^\pm , gamma-rays and baryons moving outwards with two opposite jets at the poles of the accretion disk. Internal shocks within the relativistic outflow generate the *prompt* gamma-ray emission, which is followed by an *afterglow*. The afterglow is due to the interaction of the shocks with the surrounding medium and produce a lower energy and longer lasting radiation: X-ray, ultraviolet, optical, infrared, microwave and radio photons are emitted at temporally decreasing energies [154].

Within this model the prompt gamma-ray emission, as well as the afterglow emission, is thought to be produced through synchrotron emission of shock-accelerated electrons. These synchrotron photons might be subsequently up-scattered by the same electrons via IC, in the so-called synchrotron self-Compton (SSC) mechanism, eventually giving rise to a higher energy component, up to TeV energies. If so, even though no GRB has been detected in the VHE domain so far, next-generation VHE gamma-ray telescopes might be able to observe GRBs produced by bright and nearby systems (those with redshift $z < 0.25$, to prevent severe absorption due to interactions with background photons [189]). A recent Fermi-LAT observation measured a 95.3 GeV (emitted at 128 GeV in the rest frame of the burst at redshift $z = 0.34$) photon from GRB 130427A [191]. This is a promising indication for future detection in the VHE regime.

B.2.3 Starburst galaxies

Starburst galaxies are galaxies with very high star formation rate. The enhanced supernova rate, and the consequent creation of SNRs, combined with enhanced densities of gas and radiation fields, make these objects perfect candidates for the acceleration of protons and the subsequent production of gamma rays through neutral pion decay. Also primary and secondary electrons can produce gamma-ray radiation by bremsstrahlung processes and IC scattering of low energy photons in the ambient radiation field. For these reasons, starburst galaxies are very promising sources of gamma-ray emission.

Indeed, several starburst galaxies have been detected in the VHE range and confirmed by Fermi-LAT. NGC 253, for instance, is a spiral galaxy with an overall star formation rate similar to the Milky Way's one. However, this galaxy has a starburst nucleus characterized by a small spatial extension (few hundred pc) with extremely enhanced star formation rate, leading to a large production of supernova explosions [16, 5].

B.2.4 Galaxy clusters

Galaxy clusters are the largest gravitationally bound structures in the Universe consisting of hundreds or even thousands of galaxies. These clusters are expected to be luminous gamma-ray emitters. They are formed through the merger of smaller galaxy groups, assembling masses up to $\sim 10^{15} M_{\odot}$. The merging processes release a large amount of energy through collisionless shocks and turbulence. If only a fraction of the liberated energy is converted into population of non-thermal particles, then a gamma-ray emission from the cluster should be detectable. So far, no galaxy cluster has been observed in gamma rays, and only upper limits have been calculated, e.g. [60].

Bibliography

- [1] H. Abdalla et al. H.E.S.S. observations of RX J1713.7-3946 with improved angular and spectral resolution; evidence for gamma-ray emission extending beyond the X-ray emitting shell. 2016. [arXiv:1609.08671](#), [doi:10.1051/0004-6361/201629790](#). (Cited on pages 64 and 65.)
- [2] A. A. Abdo et al. TeV Gamma-Ray Sources from a Survey of the Galactic Plane with Milagro. *The Astrophysical Journal*, 664:L91–L94, 2007. [arXiv:0705.0707](#), [doi:10.1086/520717](#). (Cited on page 6.)
- [3] A. A. Abdo et al. Gamma-Ray emission from the shell of supernova remnant W44 revealed by the Fermi LAT. *Science*, 327:1103–1106, 2009. [doi:10.1126/science.1182787](#). (Cited on page 25.)
- [4] A. A. Abdo et al. Modulated High-Energy Gamma-Ray Emission from the Microquasar Cygnus X-3. *Science*, 326(5959):1512–1516, 2009. [doi:10.1126/science.1182174](#). (Cited on page 105.)
- [5] A. A. Abdo et al. Detection of Gamma-Ray Emission from the Starburst Galaxies M82 and NGC 253 with the Large Area Telescope on Fermi. *The Astrophysical Journal*, 709:L152–L157, 2010. [arXiv:0911.5327](#), [doi:10.1088/2041-8205/709/2/L152](#). (Cited on page 110.)
- [6] A. A. Abdo et al. Fermi LAT Observations of the Supernova Remnant W28 (G6.4-0.1). *The Astrophysical Journal*, 718:348–356, 2010. [arXiv:1005.4474](#), [doi:10.1088/0004-637X/718/1/348](#). (Cited on page 104.)
- [7] A. U. Abeysekara et al. Observation of the Crab Nebula with the HAWC Gamma-Ray Observatory. 2017. [arXiv:1701.01778](#). (Cited on pages 6 and 66.)
- [8] A. U. Abeysekara et al. The 2HWC HAWC Observatory Gamma Ray Catalog. 2017. [arXiv:1702.02992](#). (Cited on pages 6, 65, 66, and 67.)
- [9] A. Abramowski et al. Discovery of the hard spectrum VHE gamma-ray source HESS J1641-463. *The Astrophysical Journal Letters*, 794:L1–L6, 2014. [arXiv:1408.5280](#), [doi:10.1088/2041-8205/794/1/L1](#). (Cited on page 70.)
- [10] A. Abramowski et al. Search for Extended gamma-ray Emission around AGN with H.E.S.S. and Fermi-LAT. *Astronomy & Astrophysics*, 562:A145, 2014. [arXiv:1401.2915](#), [doi:10.1051/0004-6361/201322510](#). (Cited on page 49.)
- [11] A. Abramowski et al. Acceleration of petaelectronvolt protons in the Galactic Centre. *Nature*, 531:476, 2016. [arXiv:1603.07730](#), [doi:10.1038/nature17147](#). (Cited on pages 19, 65, 70, 106, and 107.)
- [12] V. A. Acciari et al. VERITAS Observations of the gamma-Ray Binary LS I +61 303. *The Astrophysical Journal*, 679:1427, 2008. [arXiv:0802.2363](#), [doi:10.1086/587736](#). (Cited on page 105.)

- [13] V. A. Acciari et al. Observation of Extended VHE Emission from the Supernova Remnant IC 443 with VERITAS. *The Astrophysical Journal*, 698:L133–L137, 2009. arXiv:0905.3291, doi:10.1088/0004-637X/698/2/L133. (Cited on page 104.)
- [14] V. A. Acciari et al. Discovery of TeV Gamma Ray Emission from Tycho’s Supernova Remnant. *The Astrophysical Journal*, 730:L20, 2011. arXiv:1102.3871, doi:10.1088/2041-8205/730/2/L20. (Cited on page 104.)
- [15] F. Acero. Localising the VHE gamma-ray source at the Galactic Centre. *Monthly Notices of the Royal Astronomical Society*, 402:1877–1882, 2010. arXiv:0911.1912, doi:10.1111/j.1365-2966.2009.16014.x. (Cited on page 105.)
- [16] F. Acero et al. Detection of Gamma Rays From a Starburst Galaxy. *Science*, 326(5956):1080–1082, 2009. arXiv:0909.4651, doi:10.1126/science.1178826. (Cited on page 110.)
- [17] F. Acero et al. Gamma-ray signatures of cosmic ray acceleration, propagation, and confinement in the era of CTA. *Astroparticle Physics*, 43:276–286, 2013. arXiv:1209.0582, doi:10.1016/j.astropartphys.2012.05.024. (Cited on pages 25 and 27.)
- [18] F. Acero et al. Fermi Large Area Telescope Third Source Catalog. *The Astrophysical Journal Supplement Series*, 218(2):23, 2015. arXiv:1501.02003, doi:10.1088/0067-0049/218/2/23. (Cited on pages 4, 26, and 101.)
- [19] B. S. Acharya et al. Introducing the CTA concept. *Astroparticle Physics*, 43:3–18, 2013. doi:10.1016/j.astropartphys.2013.01.007. (Cited on pages 21, 24, 25, and 83.)
- [20] M. Ackermann et al. Fermi LAT observations of cosmic-ray electrons from 7 GeV to 1 TeV. *Physics Review*, D82:092004, 2010. arXiv:1008.3999, doi:10.1103/PhysRevD.82.092004. (Cited on page 34.)
- [21] M. Ackermann et al. The Fermi Large Area Telescope On Orbit: Event Classification, Instrument Response Functions, and Calibration. *The Astrophysical Journal Supplement Series*, 203:4, 2012. arXiv:1206.1896, doi:10.1088/0067-0049/203/1/4. (Cited on page 4.)
- [22] M. Ackermann et al. Detection of the Characteristic Pion-Decay Signature in Supernova Remnants. *Science*, 339:807–811, 2013. arXiv:1302.3307, doi:10.1126/science.1231160. (Cited on pages 4, 25, and 104.)
- [23] M. Ackermann et al. The Spectrum and Morphology of the Fermi Bubbles. *The Astrophysical Journal*, 793(1):64, 2014. arXiv:1407.7905, doi:10.1088/0004-637X/793/1/64. (Cited on page 4.)

- [24] M. Ackermann et al. Search for extended sources in the Galactic Plane using 6 years of Fermi-Large Area Telescope Pass 8 data above 10 GeV. 2017. [arXiv:1702.00476](#). (Cited on page 4.)
- [25] M. Actis et al. Design concepts for the Cherenkov Telescope Array CTA: An advanced facility for ground-based high-energy gamma-ray astronomy. *Experimental Astronomy*, 32:193–316, 2011. [arXiv:1008.3703](#), [doi:10.1007/s10686-011-9247-0](#). (Cited on pages 22, 37, 45, 70, 72, and 83.)
- [26] S. Adrian-Martinez et al. Letter of intent for KM3NeT 2.0. *Journal of Physics*, G43(8):084001, 2016. [arXiv:1601.07459](#), [doi:10.1088/0954-3899/43/8/084001](#). (Cited on pages 62, 63, 65, and 85.)
- [27] O. Adriani et al. The cosmic-ray electron flux measured by the PAMELA experiment between 1 and 625 GeV. *Physics Review Letter*, 106:201101, 2011. [arXiv:1103.2880](#), [doi:10.1103/PhysRevLett.106.201101](#). (Cited on page 34.)
- [28] F. Aharonian et al. The energy spectrum of cosmic-ray electrons at TeV energies. *Physics Review Letter*, 101:261104, 2008. [arXiv:0811.3894](#), [doi:10.1103/PhysRevLett.101.261104](#). (Cited on page 15.)
- [29] F. A. Aharonian. TeV gamma rays from BL Lac objects due to synchrotron radiation of extremely high energy protons. *New Astronomy*, 5:377–395, 2000. [arXiv:astro-ph/0003159](#), [doi:10.1016/S1384-1076\(00\)00039-7](#). (Cited on page 95.)
- [30] F. A. Aharonian. *Very high energy cosmic gamma radiation: A crucial window on the extreme universe*. World Scientific Publishing Co., 2004. [doi:10.1142/4657](#). (Cited on pages 1, 89, 98, and 99.)
- [31] F. A. Aharonian, A. A. Belyanin, E. V. Derishev, V. V. Kocharovskiy, and V. V. Kocharovskiy. Constraints on the extremely high-energy cosmic ray accelerators from classical electrodynamics. *Physical Review D*, 66(2):023005, 2002. [arXiv:astro-ph/0202229](#), [doi:10.1103/PhysRevD.66.023005](#). (Cited on page 95.)
- [32] F. A. Aharonian, L. Bergström, and C. Dermer. *Gamma Rays at Very High Energies*, volume 40 of *Astrophysics and Astronomy*. Springer-Verlag Berlin Heidelberg, 2013. [doi:10.1007/978-3-642-36134-0](#). (Cited on pages 2, 89, 92, 93, 96, and 98.)
- [33] F. A. Aharonian and S. V. Bogovalov. Exploring physics of rotation powered pulsars with sub-10 GeV imaging atmospheric Cherenkov telescopes. *New Astronomy*, 8:85–103, 2002. [arXiv:astro-ph/0208036](#), [doi:10.1016/S1384-1076\(02\)00200-2](#). (Cited on page 102.)
- [34] F. A. Aharonian, S. V. Bogovalov, and D. Khangulyan. Abrupt acceleration of a 'cold' ultrarelativistic wind from the Crab pulsar. *Nature*, 482:507–509, 2012. [doi:10.1038/nature10793](#). (Cited on page 103.)

- [35] F. A. Aharonian, J. Buckley, T. Kifune, and G. Sinnis. High energy astrophysics with ground-based gamma ray detectors. *Reports on Progress in Physics*, 71(9):096901, 2008. doi:10.1088/0034-4885/71/9/096901. (Cited on pages 3, 5, 8, 10, 11, 12, 13, 14, 64, 103, and 105.)
- [36] F. A. Aharonian, P. S. Coppi, and H. J. Völk. Very high-energy gamma-rays from AGN: Cascading on the cosmic background radiation fields and the formation of pair halos. *The Astrophysical Journal*, 423:L5–L8, 1994. arXiv:astro-ph/9312045, doi:10.1086/187222. (Cited on page 93.)
- [37] F. A. Aharonian, W. Essey, A. Kusenko, and A. Prosekin. TeV gamma rays from blazars beyond $z=1$? *Physics Review*, D87(6):063002, 2013. arXiv:1206.6715, doi:10.1103/PhysRevD.87.063002. (Cited on page 108.)
- [38] F. A. Aharonian et al. The Crab nebula and pulsar between 500-GeV and 80-TeV. Observations with the HEGRA stereoscopic air Cerenkov telescopes. *The Astrophysics Journal*, 614:897–913, 2004. arXiv:astro-ph/0407118, doi:10.1086/423931. (Cited on pages 3, 16, 36, 72, 75, 80, and 103.)
- [39] F. A. Aharonian et al. Very high-energy gamma rays from the direction of Sagittarius A*. *Astronomy & Astrophysics*, 425:L13–L17, 2004. arXiv:astro-ph/0408145, doi:10.1051/0004-6361:200400055. (Cited on page 105.)
- [40] F. A. Aharonian et al. Very high energy gamma rays from the composite SNR G0.9+0.1. *Astron. Astrophys.*, 432:L25–L29, 2005. arXiv:astro-ph/0501265, doi:10.1051/0004-6361:200500022. (Cited on pages 103 and 106.)
- [41] F. A. Aharonian et al. Discovery of very-high-energy gamma-rays from the galactic centre ridge. *Nature*, 439:695–698, 2006. arXiv:astro-ph/0603021, doi:10.1038/nature04467. (Cited on pages 19, 65, 66, and 106.)
- [42] F. A. Aharonian et al. Observations of the Crab Nebula with H.E.S.S. *Astronomy & Astrophysics*, 457:899–915, 2006. arXiv:astro-ph/0607333, doi:10.1051/0004-6361:20065351. (Cited on pages 31, 32, 80, and 103.)
- [43] F. A. Aharonian et al. The H.E.S.S. survey of the inner galaxy in very high-energy gamma-rays. *The Astrophysical Journal*, 636:777–797, 2006. arXiv:astro-ph/0510397, doi:10.1086/498013. (Cited on page 66.)
- [44] F. A. Aharonian et al. Primary particle acceleration above 100 TeV in the shell-type Supernova Remnant RX J1713.7-3946 with deep H.E.S.S. observations. *Astronomy & Astrophysics*, 464:235–243, 2007. arXiv:astro-ph/0611813, doi:10.1051/0004-6361:20066381. (Cited on page 104.)

- [45] F. A. Aharonian et al. Discovery of very high energy gamma-ray emission coincident with molecular clouds in the W28 (G6.4-0.1) field. *Astronomy & Astrophysics*, 481:401, 2008. [arXiv:0801.3555](#), [doi:10.1051/0004-6361:20077765](#). (Cited on page 104.)
- [46] F. A. Aharonian et al. Discovery of very high energy gamma-ray emission from Centaurus A with H.E.S.S. *The Astrophysical Journal*, 695:L40–L44, 2009. [arXiv:0903.1582](#), [doi:10.1088/0004-637X/695/1/L40](#). (Cited on page 108.)
- [47] F. A. Aharonian, W. Hofmann, A. K. Konopelko, and Völk H. J. The potential of ground based arrays of imaging atmospheric Cherenkov telescopes. I. Determination of shower parameters. *Astroparticle Physics*, 6(324):343–368. [doi:10.1016/S0927-6505\(96\)00069-2](#). (Cited on page 33.)
- [48] F. A. Aharonian, D. Khangulyan, and D. Malyshev. Cold ultra-relativistic pulsar winds as potential sources of galactic gamma-ray lines above 100 GeV. *Astronomy & Astrophysics*, 547:A114, 2012. [arXiv:1207.0458](#), [doi:10.1051/0004-6361/201220092](#). (Cited on page 87.)
- [49] F. A. Aharonian and A. Neronov. High energy gamma rays from the massive black hole in the Galactic center. *The Astrophysical Journal*, 619:306–313, 2005. [arXiv:astro-ph/0408303](#), [doi:10.1086/426426](#). (Cited on pages 105 and 106.)
- [50] M. L. Ahnen et al. Super-orbital variability of LS I+61 303 at TeV energies. *Astronomy & Astrophysics*, 591:A76, 2016. [arXiv:1603.06973](#), [doi:10.1051/0004-6361/201527964](#). (Cited on page 105.)
- [51] A. I. Akhiezer and V. B. Berestetskii. *Quantum electrodynamics, vol XI of interscience monographs and texts in physics and astronomy*. Interscience Publishers, New York, 1965. (Cited on page 89.)
- [52] J. Albert et al. Observation of gamma-rays from the galactic center with the MAGIC telescope. *The Astrophysical Journal*, 638:L101–L104, 2006. [arXiv:astro-ph/0512469](#), [doi:10.1086/501164](#). (Cited on page 105.)
- [53] J. Albert et al. Discovery of Very High Energy γ -Rays from 1ES 1011+496 at $z=0.212$. *The Astrophysical Journal Letters*, 667:L21–L24, 2007. [arXiv:0706.4435](#), [doi:10.1086/521982](#). (Cited on pages 70 and 79.)
- [54] J. Albert et al. Discovery of VHE Gamma Radiation from IC443 with the MAGIC Telescope. *The Astrophysical Journal*, 664:L87–L90, 2007. [arXiv:0705.3119](#), [doi:10.1086/520957](#). (Cited on page 104.)
- [55] J. Albert et al. Observation of VHE gamma-rays from Cassiopeia A with the MAGIC telescope. *Astronomy & Astrophysics*, 474:937–940, 2007. [arXiv:0706.4065](#), [doi:10.1051/0004-6361:20078168](#). (Cited on page 104.)

- [56] J. Albert et al. Observations of mkn 421 with the MAGIC telescope. *The Astrophysical Journal*, 663:125–138, 2007. [arXiv:astro-ph/0603478](#), [doi:10.1086/518221](#). (Cited on page 108.)
- [57] J. Albert et al. Very High Energy Gamma-ray Radiation from the Stellar-mass Black Hole Cygnus X-1. *The Astrophysical Journal*, 665:L51–L54, 2007. [arXiv:0706.1505](#), [doi:10.1086/521145](#). (Cited on page 105.)
- [58] J. Albert et al. Periodic very high energy gamma-ray emission from LS I +61 303 observed with the MAGIC telescope. *The Astrophysical Journal*, 693:303–310, 2009. [arXiv:0806.1865](#), [doi:10.1088/0004-637X/693/1/303](#). (Cited on page 105.)
- [59] J. Aleksic et al. Search for an extended VHE gamma-ray emission from Mrk 421 and Mrk 501 with the MAGIC Telescope. *Astronomy & Astrophysics*, 524:A77, 2010. [arXiv:1004.1093](#), [doi:10.1051/0004-6361/201014747](#). (Cited on page 49.)
- [60] J. Aleksić et al. Constraining Cosmic Rays and Magnetic Fields in the Perseus Galaxy Cluster with TeV observations by the MAGIC telescopes. *Astronomy & Astrophysics*, 541:A99, 2012. [arXiv:1111.5544](#), [doi:10.1051/0004-6361/201118502](#). (Cited on page 110.)
- [61] J. Aleksić et al. MAGIC observations of the giant radio galaxy M87 in a low-emission state between 2005 and 2007. *Astronomy & Astrophysics*, 544:A96, 2012. [arXiv:1207.2147](#), [doi:10.1051/0004-6361/201117827](#). (Cited on page 108.)
- [62] J. Aleksić et al. Phase-resolved energy spectra of the Crab Pulsar in the range of 50-400 GeV measured with the MAGIC Telescopes. *Astronomy & Astrophysics*, 540:A69, 2012. [arXiv:1109.6124](#), [doi:10.1051/0004-6361/201118166](#). (Cited on page 101.)
- [63] J. Aleksić et al. Black hole lightning due to particle acceleration at subhorizon scales. *Science*, 346:1080–1084, 2014. [arXiv:1412.4936](#), [doi:10.1126/science.1256183](#). (Cited on page 24.)
- [64] J. Aleksić et al. Rapid and multiband variability of the TeV bright active nucleus of the galaxy IC 310. *Astronomy & Astrophysics*, 563:A91, 2014. [arXiv:1305.5147](#), [doi:10.1051/0004-6361/201321938](#). (Cited on page 108.)
- [65] J. Aleksić et al. Measurement of the Crab Nebula spectrum over three decades in energy with the MAGIC telescopes. *Journal of High Energy Astrophysics*, 5-6:30–38, 2015. [arXiv:1406.6892](#), [doi:10.1016/j.jheap.2015.01.002](#). (Cited on pages 69, 74, and 103.)
- [66] J. Aleksić et al. Multiwavelength observations of Mrk 501 in 2008. *Astronomy & Astrophysics*, 573:A50, 2015. [arXiv:1410.6391](#), [doi:10.1051/0004-6361/201322906](#). (Cited on page 108.)

- [67] J. Aleksić et al. The major upgrade of the MAGIC telescopes, Part II: A performance study using observations of the Crab Nebula. *Astroparticle Physics*, 72:76–94, 2016. [arXiv:1409.5594](#), [doi:10.1016/j.astropartphys.2015.02.005](#). (Cited on pages 20, 69, and 83.)
- [68] E. Aliu et al. Observation of pulsed gamma-rays above 25 GeV from the Crab pulsar with MAGIC. *Science*, 322:1221–1224, 2008. [arXiv:0809.2998](#), [doi:10.1126/science.1164718](#). (Cited on page 102.)
- [69] E. Aliu et al. Detection of Pulsed Gamma Rays Above 100 GeV from the Crab Pulsar. *Science*, 334:69–72, 2011. [arXiv:1108.3797](#), [doi:10.1126/science.1208192](#). (Cited on page 101.)
- [70] L. Ambrogio. Morphological studies of gamma-ray sources with IACT arrays. *Nuovo Cimento C*, 39(2):283, 2016. [doi:10.1393/ncc/i2016-16283-0](#). (Cited on page VI.)
- [71] L. Ambrogio, E. De Oña Wilhelmi, and F. A. Aharonian. On the potential of atmospheric Cherenkov telescope arrays for resolving TeV gamma-ray sources in the Galactic Plane. *Astroparticle Physics*, 80:22–33, 2016. [arXiv:1603.04365](#), [doi:10.1016/j.astropartphys.2016.03.004](#). (Cited on page VI.)
- [72] M. Amenomori et al. Observation of multi TeV gamma-rays from the Crab Nebula using the Tibet Air Shower Array. *The Astrophysical Journal*, 525:L93, 1999. [arXiv:astro-ph/9909172](#), [doi:10.1086/312342](#). (Cited on page 5.)
- [73] E. O. Anguner, F. A. Aharonian, P. Bordas, S. Casanova, C. Hoischen, I. Oya, and A. Ziegler. HESS J1826130: A very hard gamma-ray spectrum source in the galactic plane. *AIP Conf. Proc.*, 1792(1):040024, 2017. [arXiv:1701.07002](#), [doi:10.1063/1.4968928](#). (Cited on page 65.)
- [74] S. Ansoldi et al. Teraelectronvolt pulsed emission from the Crab pulsar detected by MAGIC. *Astronomy & Astrophysics*, 585:A133, 2016. [arXiv:1510.07048](#), [doi:10.1051/0004-6361/201526853](#). (Cited on page 101.)
- [75] J. Arons. Pair creation above pulsar polar caps-Steady flow in the surface acceleration zone and polar CAP X-ray emission. *The Astrophysical Journal*, 248:1099–1116, 1981. [doi:10.1086/159239](#). (Cited on page 102.)
- [76] J. Arons and E. T. Scharlemann. Pair formation above pulsar polar caps-Structure of the low altitude acceleration zone. *The Astrophysical Journal*, 231:854–879, 1979. [doi:10.1086/157250](#). (Cited on page 102.)
- [77] R. Atkins et al. Evidence for TeV gamma-ray emission from the galactic plane. *Physical Review Letters*, 95:251103, 2005.

arXiv:astro-ph/0502303, doi:10.1103/PhysRevLett.95.251103.
(Cited on page 6.)

- [78] R. W. Atkins et al. Observation of TeV gamma-rays from the Crab nebula with MILAGRO using a new background rejection technique. *The Astrophysical Journal*, 595:803–811, 2003. arXiv:astro-ph/0305308, doi:10.1086/377498. (Cited on page 5.)
- [79] W. B. Atwood et al. The Large Area Telescope on the Fermi Gamma-ray Space Telescope Mission. *Astrophysics Journal*, 697:1071–1102, 2009. arXiv:0902.1089, doi:10.1088/0004-637X/697/2/1071. (Cited on page 3.)
- [80] L. Baldini. The Large Area Telescope in the context of the extended Fermi mission. *Nuclear Physics B - Proceedings Supplements*, 243-244:125–130, 2013. doi:10.1016/j.nuclphysbps.2013.09.001. (Cited on page 4.)
- [81] Y. Becherini, A. Djannati-Atai, V. Marandon, M. Punch, and S. Pita. A new analysis strategy for detection of faint gamma-ray sources with Imaging Atmospheric Cherenkov Telescopes. *Astroparticle Physics*, 34:858–870, 2011. arXiv:1104.5359, doi:10.1016/j.astropartphys.2011.03.005. (Cited on page 17.)
- [82] Y. Becherini, B. Khelifi, S. Pita, and M. Punch. Advanced analysis and event reconstruction for the CTA Observatory. *AIP Conf. Proc.*, 1505:769–772, 2012. arXiv:1211.5997, doi:10.1063/1.4772373. (Cited on pages 14 and 17.)
- [83] A. V. Belikov, G. Zaharijas, and J. Silk. Study of the Gamma-ray Spectrum from the Galactic Center in view of Multi-TeV Dark Matter Candidates. *Physics Review*, D86:083516, 2012. arXiv:1207.2412, doi:10.1103/PhysRevD.86.083516. (Cited on page 105.)
- [84] D. Berge et al. Fast variability of TeV gamma-rays from the radio galaxy M87. *Science*, 314:1424, 2006. arXiv:astro-ph/0612016, doi:10.1126/SCIENCE.1134408. (Cited on page 108.)
- [85] J. Beringer et al. Review of Particle Physics (RPP). *Physics Review*, D86:010001, 2012. doi:10.1103/PhysRevD.86.010001. (Cited on page 34.)
- [86] K. Bernlöhr et al. Monte Carlo design studies for the Cherenkov Telescope Array. *Astroparticle Physics*, 43:171–188, 2013. arXiv:1210.3503, doi:10.1016/j.astropartphys.2012.10.002. (Cited on pages 5, 17, 30, 34, 51, 52, 71, 83, and 84.)
- [87] G. F. Bignami, G. Boella, J. J. Burger, B. G. Taylor, P. Keirle, J. A. Paul, H. A. Mayer-Hasselwander, E. Pfeffermann, L. Scarsi, and B. N. Swanenburg. The COS-B experiment for gamma-ray astronomy. *Space Science Instrumentation*, 1:245–268, 1975. (Cited on page 4.)

- [88] S. V. Bogovalov and F. A. Aharonian. Very high-energy gamma radiation associated with the unshocked wind of the Crab pulsar. *Monthly Notices of the Royal Astronomical Society*, 313:504, 2000. arXiv:astro-ph/0003157, doi:10.1046/j.1365-8711.2000.03250.x. (Cited on page 87.)
- [89] B. M. Bolotovskii and E. M. Leikin. J.V. JELLEY, CHERENKOV RADIATION AND ITS APPLICATIONS. *Soviet Physics Uspekhi*, 2(6):987, 1960. (Cited on pages 10 and 11.)
- [90] P. Bordas et al. Observations of Binary Systems with the H.E.S.S. Telescopes. *AIP Conf. Proc.*, 1792(1):040017, 2017. arXiv:1610.03264, doi:10.1063/1.4968921. (Cited on page 105.)
- [91] A. Burtovoi and L. Zampieri. Simulated Gamma-Ray Pulse Profile of the Crab Pulsar with the Cherenkov Telescope Array. *Monthly Notices of the Royal Astronomical Society*, 459(4):3783–3791, 2016. arXiv:1604.04066, doi:10.1093/mnras/stw883. (Cited on page 76.)
- [92] K. S. Cheng, C. Ho, and M. Ruderman. Energetic radiation from rapidly spinning pulsars. I-Outer magnetosphere gaps. II-VELA and Crab. *The Astrophysical Journal*, 300:500–539, 1986. (Cited on page 102.)
- [93] G. W. Clark, G. P. Garmire, and W. L. Kraushaar. Observation of high-energy cosmic gamma rays. *The Astrophysical Journal*, 153:L203, 1968. doi:10.1086/180252. (Cited on page 4.)
- [94] J. K. Daugherty and A. K. Harding. Electromagnetic cascades in pulsars. *The Astrophysical Journal*, 252:337–347, 1982. (Cited on page 102.)
- [95] M. de Naurois. *Very High Energy astronomy from H.E.S.S. to CTA. Opening of a new astronomical window on the non-thermal Universe*. PhD thesis, Ecole Polytechnique, 2012. URL: <http://tel.archives-ouvertes.fr/tel-00687872>. (Cited on page 105.)
- [96] E. De Oña Wilhelmi et al. Prospects for Observations of Pulsars and Pulsar Wind Nebulae with CTA. *Astroparticle Physics*, 43:287–300, 2013. arXiv:1209.0357, doi:10.1016/j.astropartphys.2012.08.009. (Cited on page 26.)
- [97] V. Z. De Torres. *The keV-TeV connection in gamma-ray binaries*. PhD thesis, Universitat de Barcelona, 2011. URL: http://tdx.cat/bitstream/handle/10803/33649/VZdT_THESIS.pdf?sequence=1. (Cited on pages 90 and 91.)
- [98] G. Di Sciacio. ARGO-YBJ: Status and Highlights. In *Proceedings, Vulcano Workshop 2012: Frontier Objects in Astrophysics and Particle Physics: Vulcano, Italy, May 28-June 2, 2012*, 2012. arXiv:1210.2635. (Cited on page 5.)

- [99] G. Di Sciascio. The LHAASO experiment: from Gamma-Ray Astronomy to Cosmic Rays. *Nuclear and Particle Physics Proceedings*, 279-281:166–173, 2016. arXiv:1602.07600, doi:10.1016/j.nuclphysbps.2016.10.024. (Cited on page 7.)
- [100] A. Donath, F. Brun, R. C. G. Chaves, C. Deil, V. Marandon, and R. Terrier. The H.E.S.S. galactic plane survey. *AIP Conf. Proc.*, 1792(1):040001, 2017. doi:10.1063/1.4968905. (Cited on pages 19, 56, 58, and 86.)
- [101] M. Doro et al. Dark Matter and Fundamental Physics with the Cherenkov Telescope Array. *Astroparticle Physics*, 43:189–214, 2013. arXiv:1208.5356, doi:10.1016/j.astropartphys.2012.08.002. (Cited on pages 22, 26, 27, and 99.)
- [102] J.-L. Dournaux, J.-M. Huet, D. Dumas, J.-P. Amans, G. Fasola, P. Laporte, J.-J. Bousquet, and H. Sol. Performance of the Mechanical Structure of the SST-2M GCT Telescope for the Cherenkov Telescope Array. *PoS, ICRC2015:946*, 2016. arXiv:1508.06415. (Cited on page 22.)
- [103] L. O’C. Drury, F. A. Aharonian, and H. J. Völk. The Gamma-ray visibility of supernova remnants: A Test of cosmic ray origin. *Astronomy & Astrophysics*, 287:959–971, 1994. arXiv:astro-ph/9305037. (Cited on page 103.)
- [104] G. Dubus et al. Surveys with the Cherenkov Telescope Array. *Astroparticle Physics*, 43:317–330, 2013. arXiv:1208.5686, doi:10.1016/j.astropartphys.2012.05.020. (Cited on pages 21 and 26.)
- [105] R. Enberg, M. H. Reno, and I. Sarcevic. Prompt neutrino fluxes from atmospheric charm. *Physics Review*, D78:043005, 2008. arXiv:0806.0418, doi:10.1103/PhysRevD.78.043005. (Cited on page 65.)
- [106] M. Errando et al. Discovery of very high energy gamma-rays from the flat spectrum radio quasar 3C 279 with the MAGIC telescope. *AIP Conf. Proc.*, 1085:423–426, 2009. arXiv:0901.3275, doi:10.1063/1.3076698. (Cited on page 70.)
- [107] A. Eungwanichayapant and F. Aharonian. Very High Energy gamma-rays from electron/positron Pair Halos. *International Journal of Modern Physics*, D18:911–927, 2009. arXiv:0907.2971, doi:10.1142/S0218271809014832. (Cited on pages 93 and 94.)
- [108] A. M. Fernandez. Search for extended gamma ray emission in Markarian 421 using VERITAS observations. 2014. arXiv:1406.4764. (Cited on page 49.)
- [109] C. E. Fichtel, R. C. Hartman, D. A. Kniffen, D. J. Thompson, H. Ogelman, M. E. Ozel, T. Tumer, and G. F. Bignami. High-energy gamma-ray results from the second small astronomy satellite. *The Astrophysical Journal*, 198:163–182, 1975. doi:10.1086/153590. (Cited on page 4.)

- [110] S. Funk. Indirect Detection of Dark Matter with gamma rays. 2013. [arXiv:1310.2695](#), [doi:10.1073/pnas.1308728111](#). (Cited on page 100.)
- [111] S. Funk. Ground- and Space-Based Gamma-Ray Astronomy. *Annual Review of Nuclear and Particle Science*, 65:245–277, 2015. [arXiv:1508.05190](#), [doi:10.1146/annurev-nucl-102014-022036](#). (Cited on pages 92, 98, and 104.)
- [112] S. Gabici. Cosmic rays and molecular clouds. *Astrophysics and Space Science Proceedings*, 34:221–247, 2013. [arXiv:1208.4979](#), [doi:10.1007/978-3-642-35410-6_16](#). (Cited on page 104.)
- [113] S. Gabici. Gamma-Ray Emission from Supernova Remnants and Surrounding Molecular Clouds. *AIP Conf. Proc.*, 1792(1):020002, 2017. [arXiv:1610.06234](#), [doi:10.1063/1.4968887](#). (Cited on page 104.)
- [114] N. Galante. VERITAS observation of Mrk421 flaring activity. In *Proceedings, 32nd International Cosmic Ray Conference (ICRC 2011): Beijing, China, August 11-18, 2011*, volume 8, pages 63–66, 2011. [arXiv:1109.6059](#), [doi:10.7529/ICRC2011/V08/0782](#). (Cited on page 108.)
- [115] M. Gaug, M. Daniel, D. Berge, R. De Los Reyes, M. Doro, A. Forster, M. C. Maccarone, D. Parsons, and C. Van Eldik. Calibration of the Cherenkov Telescope Array. *PoS, ICRC2015:929*, 2016. [arXiv:1508.07225](#). (Cited on pages 75 and 86.)
- [116] G. Ghisellini. Gamma Ray Bursts: basic facts and ideas. *IAU Symposia*, 275:335, 2011. [arXiv:1010.3015](#), [doi:10.1017/S1743921310016364](#). (Cited on page 109.)
- [117] B. Giebels. Status and recent results from H.E.S.S. In *Proceedings, 4th International Fermi Symposium: Monterey, California, USA, October 28-November 2, 2012*, 2013. [arXiv:1303.2850](#). (Cited on pages 19, 69, and 83.)
- [118] V. L. Ginzburg and S. I. Syrovatskii. *The Origin of Cosmic Rays*. Pergamon, 1964. [doi:10.1016/B978-0-08-013526-7.50003-7](#). (Cited on page 103.)
- [119] K. Greisen. Cosmic ray showers. *Annual Review of Nuclear Science*, 10(1):63–108, 1960. (Cited on page 8.)
- [120] R. C. Hartman et al. The Third EGRET catalog of high-energy gamma-ray sources. *The Astrophysical Journal Supplement Series*, 123:79, 1999. [doi:10.1086/313231](#). (Cited on page 4.)
- [121] T. Hassan, L. Arrabito, K. Bernlör, J. Bregeon, J. Hinton, T. Jogler, G. Maier, A. Moralejo, F. Di Pierro, and M. Wood. Second large-scale Monte Carlo study for the Cherenkov Telescope Array. *PoS*,

- ICRC2015:971, 2016. [arXiv:1508.06075](#). (Cited on pages 29, 34, and 45.)
- [122] W. Heitler. *The Quantum Theory of Radiation*. Dover Books on Physics and Chemistry. Dover Publications, 1954. (Cited on pages 7, 89, and 99.)
- [123] M. Heller et al. The Single Mirror Small Sized Telescope For The Cherenkov Telescope Array. *AIP Conf. Proc.*, 1792(1):080003, 2017. [arXiv:1610.01867](#), [doi:10.1063/1.4969024](#). (Cited on page 22.)
- [124] A. M. Hillas. Cerenkov light images of EAS produced by primary gamma. 3:445–448, 1985. (Cited on page 13.)
- [125] A. M. Hillas. Evolution of ground-based gamma-ray astronomy from the early days to the Cherenkov Telescope Arrays. *Astroparticle Physics*, 43:19–43, 2013. [doi:10.1016/j.astropartphys.2012.06.002](#). (Cited on pages 14 and 15.)
- [126] J. A. Hinton and W. Hofmann. Teraelectronvolt astronomy. *Annual Review of Astronomy and Astrophysics*, 47:523–565, 2009. [arXiv:1006.5210](#), [doi:10.1146/annurev-astro-082708-101816](#). (Cited on page 3.)
- [127] K. Hirotani and S. Shibata. One-dimensional electric field structure of an outer gap accelerator - I. γ -ray production resulting from curvature radiation. *Monthly Notices of the Royal Astronomical Society*, 308(1):54–66, 1999. [doi:10.1046/j.1365-8711.1999.02696.x](#). (Cited on page 102.)
- [128] W. Hofmann, I. Jung, A. Konopelko, H. Krawczynski, H. Lampeitl, and G. Puehlhofer. Comparison of techniques to reconstruct the gamma-ray showers from multiple stereoscopic Cherenkov images. *Astroparticle Physics*, 122:135–143, 1999. [arXiv:astro-ph/9904234](#), [doi:10.1016/S0927-6505\(99\)00084-5](#). (Cited on page 17.)
- [129] J. Holder. Latest Results from VERITAS: Gamma 2016. *AIP Conf. Proc.*, 1792(1):020013, 2017. [arXiv:1609.02881](#), [doi:10.1063/1.4968898](#). (Cited on pages 20, 69, and 83.)
- [130] M. Holler, D. Berge, C. Van Eldik, J.-P. Lenain, V. Marandon, T. Murač, R. D. De Naurois, M. and Parsons, H. Prokoph, and D. Zaborov. Observations of the Crab Nebula with H.E.S.S. Phase II. *PoS*, ICRC2015:847, 2016. [arXiv:1509.02902](#). (Cited on page 69.)
- [131] M. Honda. Atmospheric Neutrino Flux Calculation with NRLMSISE-00 Atmosphere Model and New Cosmic Ray Observations. *JPS Conf. Proc.*, 12:010008, 2016. [doi:10.7566/JPSCP.12.010008](#). (Cited on page 65.)
- [132] D. Huang and A. Konopelko. VERITAS Observations of Mkn 501 in 2009. 2009. [arXiv:0912.3772](#). (Cited on page 108.)
- [133] S. Inoue et al. Gamma-Ray Burst Science in the Era of the Cherenkov Telescope Array. *Astroparticle Physics*, 43:252–275, 2013.

arXiv:1301.3014, doi:10.1016/j.astropartphys.2013.01.004.
(Cited on page 26.)

- [134] M. Iori, P. Majumdar, F. De Persio, A. Chatterjee, F. Ferrarotto, B. K. Nagesh, L. Saha, and B. B. Singh. Design of a prototype device to calibrate the Large Size Telescope camera of the Cherenkov Telescope Array. *PoS, ICRC2015:954*, 2016. arXiv:1508.06752. (Cited on page 22.)
- [135] J. M. Jauch and F. Rohrlich. *The Theory of Photons and Electrons; the Relativistic Quantum Field Theory of Charged Particles with Spin One-half*. Addison-Wesley, 1955. (Cited on page 89.)
- [136] K.-H. Kampert and M. Unger. Measurements of the Cosmic Ray Composition with Air Shower Experiments. *Astroparticle Physics*, 35:660–678, 2012. arXiv:1201.0018, doi:10.1016/j.astropartphys.2012.02.004. (Cited on page 9.)
- [137] A. Kappes, J. Hinton, C. Stegmann, and F. A. Aharonian. Potential Neutrino Signals from Galactic Gamma-Ray Sources. *The Astrophysical Journal*, 656:870–896, 2007. [Erratum: *Astrophys. J.*661,1348(2007)]. arXiv:astro-ph/0607286, doi:10.1086/508936, 10.1086/518161. (Cited on page 64.)
- [138] S. R. Kelner and F. A. Aharonian. Energy spectra of gamma-rays, electrons and neutrinos produced at interactions of relativistic protons with low energy radiation. *Physics Review*, D78:034013, 2008. [Erratum: *Phys. Rev.*D82,099901(2010)]. arXiv:0803.0688, doi:10.1103/PhysRevD.82.099901, 10.1103/PhysRevD.78.034013. (Cited on page 76.)
- [139] S. R. Kelner, A. Y. Prosekin, and F. A. Aharonian. Synchro-curvature radiation of charged particles in the strong curved magnetic fields. *The Astronomical Journal*, 149:33, 2015. arXiv:1501.04994, doi:10.1088/0004-6256/149/1/33. (Cited on page 95.)
- [140] A. Kohnle et al. Stereoscopic imaging of air showers with the first two HEGRA Cherenkov telescopes. *Astroparticle Physics*, 5:119–131, 1996. doi:10.1016/0927-6505(96)00011-4. (Cited on page 16.)
- [141] K. Kosack et al. TeV gamma-ray observations of the galactic center. *The Astrophysical Journal*, 608:L97–L100, 2004. arXiv:astro-ph/0403422, doi:10.1086/422469. (Cited on page 105.)
- [142] W. L. Kraushaar and G. W. Clark. Search for Primary Cosmic Gamma Rays with the Satellite Explorer XI. *Physical Review Letters*, 8:106–109, 1962. doi:10.1103/PhysRevLett.8.106. (Cited on page 3.)
- [143] E. Lefa, S. R. Kelner, and F. A. Aharonian. On the spectral shape of radiation due to Inverse Compton Scattering close to the maximum cut-off. *The Astrophysical Journal*, 753:176, 2012. arXiv:1205.2929, doi:10.1088/0004-637X/753/2/176. (Cited on page 76.)

- [144] A. Lemièrre, R. Terrier, L. Jouvin, V. Marandon, and B. Khelifi. Study of the VHE diffuse emission in the central 200 pc of our Galaxy with H.E.S.S. *PoS, ICRC2015:838*, 2016. [arXiv:1510.04518](#). (Cited on page 106.)
- [145] M. Lemoine-Goumard. Status of ground-based gamma-ray astronomy. In *Proceedings, 34th International Cosmic Ray Conference (ICRC 2015)*, 2015. [arXiv:1510.01373](#). (Cited on page 108.)
- [146] M. Lemoine-Goumard, B. Degrangé, and M. Tluczykont. Selection and 3D-Reconstruction of Gamma-Ray-induced Air Showers with a Stereoscopic System of Atmospheric Cherenkov Telescopes. *Astroparticle Physics*, 25:195–211, 2006. [arXiv:astro-ph/0601373](#), [doi:10.1016/j.astropartphys.2006.01.005](#). (Cited on pages 14 and 17.)
- [147] R. W. Leo. *Techniques for Nuclear and Particle Physics Experiments*. Springer, 1987. (Cited on page 97.)
- [148] T.-P. Li and Y.-Q. Ma. Analysis methods for results in gamma-ray astronomy. *The Astrophysical Journal*, 272:317–324, 1983. [doi:10.1086/161295](#). (Cited on pages 35, 52, 71, and 78.)
- [149] M. S. Longair. *High Energy Astrophysics*. Cambridge University Press, 2011. (Cited on page 89.)
- [150] M. A. Malkov and L. O’C. Drury. Nonlinear theory of diffusive acceleration of particles by shock waves. *Reports on Progress in Physics*, 64(4):429–481, 2001. [doi:10.1088/0034-4885/64/4/201](#). (Cited on page 103.)
- [151] D. Mazin, M. Raue, B. Behera, S. Inoue, Y. Inoue, T. Nakamori, and T. Totani. Potential of EBL and cosmology studies with the Cherenkov Telescope Array. *Astroparticle Physics*, 43:241–251, 2013. [arXiv:1303.7124](#), [doi:10.1016/j.astropartphys.2012.09.002](#). (Cited on page 26.)
- [152] K. Meagher. Six years of VERITAS observations of the Crab Nebula. *PoS, ICRC2015:792*, 2016. [arXiv:1508.06442](#). (Cited on page 103.)
- [153] P. Meszaros. Gamma-Ray Bursts. *Reports on Progress in Physics*, 69:2259–2322, 2006. [arXiv:astro-ph/0605208](#), [doi:10.1088/0034-4885/69/8/R01](#). (Cited on page 109.)
- [154] P. Meszaros and M. J. Rees. Optical and long wavelength afterglow from gamma-ray bursts. *The Astrophysical Journal*, 476:232–237, 1997. [arXiv:astro-ph/9606043](#), [doi:10.1086/303625](#). (Cited on page 109.)
- [155] I. F. Mirabel and L. F. Rodríguez. A superluminal source in the Galaxy. *Nature*, 371:46–48, 1994. [doi:10.1038/371046a0](#). (Cited on page 105.)

- [156] R. Mirzoyan. Discovery of Very High Energy Gamma-Ray Emission from the distant FSRQ PKS 1441+25 with the MAGIC telescopes. *The Astronomer's Telegram*, 7416, 2015. (Cited on pages 20 and 108.)
- [157] A. Moralejo, M. Gaug, E. Carmona, P. Colin, C. Delgado, S. Lombardi, D. Mazin, V. Scalzotto, J. Sitarek, and D. Tescaro. MARS, the MAGIC Analysis and Reconstruction Software. 2009. [arXiv:0907.0943](https://arxiv.org/abs/0907.0943). (Cited on pages 14 and 17.)
- [158] Y. P. Ochelkov and V. V. Usov. Curvature radiation of relativistic particles in the magnetosphere of pulsars. *Astrophysics and Space Science*, 69(2):439–460, 1980. doi:10.1007/BF00661929. (Cited on page 95.)
- [159] J. M. Paredes et al. Binaries with the eyes of CTA. *Astroparticle Physics*, 43:301–316, 2013. [arXiv:1210.3215](https://arxiv.org/abs/1210.3215), doi:10.1016/j.astropartphys.2012.09.004. (Cited on page 26.)
- [160] G. Pareschi. The ASTRI SST-2M prototype and mini-array for the Cherenkov Telescope Array (CTA). *Proc. SPIE Int. Soc. Opt. Eng.*, 9906:99065T, 2016. doi:10.1117/12.2232275. (Cited on page 22.)
- [161] N. for the VERITAS Collaboration Park. Study of high-energy particle acceleration in Tycho with gamma-ray observations. 2015. [arXiv:1508.07068](https://arxiv.org/abs/1508.07068). (Cited on page 85.)
- [162] C. Pittori. AGILE Data Center and AGILE science highlights. *Nuclear Physics B - Proceedings Supplements*, 239-240:104–108, 2013. doi:10.1016/j.nuclphysbps.2013.05.017. (Cited on page 105.)
- [163] J. R. Primack. Probing galaxy formation with high-energy gamma-rays. In *Astroparticle and gamma-ray physics in space. Proceedings, International School of space science, ISSS 2001, L'Aquila, Italy, August 30-September 7, 2001*, pages 559–580, 2002. [arXiv:astro-ph/0201119](https://arxiv.org/abs/astro-ph/0201119). (Cited on page 94.)
- [164] A. Y. Prosekin, S. R. Kelner, and F. A. Aharonian. Non-variable cosmologically distant gamma-ray emitters as an imprint of propagation of ultra-high-energy protons. *Astronomy & Astrophysics*, 536:A30, 2011. [arXiv:1105.1947](https://arxiv.org/abs/1105.1947), doi:10.1051/0004-6361/201117231. (Cited on page 99.)
- [165] R. W. Romani. Gamma-ray pulsars: radiation processes in the outer magnetosphere. *The Astrophysical Journal*, 470:469, 1996. doi:10.1086/177878. (Cited on page 102.)
- [166] S. Sabatini et al. Episodic Transient Gamma-Ray Emission from the Microquasar Cygnus X-1. *The Astrophysical Journal*, 712:L10–L15, 2010. [arXiv:1002.4967](https://arxiv.org/abs/1002.4967), doi:10.1088/2041-8205/712/1/L10. (Cited on page 105.)

- [167] V. Sahakian, F. Aharonian, and A. Akhperdzhanian. Cherenkov light in electron-induced air showers. *Astroparticle Physics*, 25:233–241, 2006. doi:10.1016/j.astropartphys.2006.02.003. (Cited on page 15.)
- [168] Y. Shikaze et al. Measurements of 0.2 to 20-GeV/n cosmic-ray proton and helium spectra from 1997 through 2002 with the BESS spectrometer. *Astroparticle Physics*, 28:154–167, 2007. arXiv:astro-ph/0611388, doi:10.1016/j.astropartphys.2007.05.001. (Cited on page 34.)
- [169] H. Sol et al. Active Galactic Nuclei under the scrutiny of CTA. *Astroparticle Physics*, 43:215–240, 2013. arXiv:1304.3024, doi:10.1016/j.astropartphys.2012.12.005. (Cited on pages 25 and 26.)
- [170] M. Spurio. *Particles and Astrophysics: A Multi-Messenger Approach*. Astronomy and Astrophysics Library. Springer International Publishing, 2014. (Cited on pages 8, 9, 10, 12, and 98.)
- [171] M. Szanecki, D. Sobczyńska, A. Niedźwiecki, J. Sitarek, and W. Bednarek. Monte Carlo simulations of alternative sky observation modes with the Cherenkov Telescope Array. *Astroparticle Physics*, 67:33–46, 2015. arXiv:1501.02586, doi:10.1016/j.astropartphys.2015.01.008. (Cited on pages 31 and 60.)
- [172] M. Tavani et al. Extreme particle acceleration in the microquasar Cygnus X-3. *Nature*, 462:620–623, 2009. arXiv:0910.5344, doi:10.1038/nature08578. (Cited on page 105.)
- [173] M. Tavani et al. The AGILE Mission. *Astronomy & Astrophysics*, 502:995–1013, 2009. arXiv:0807.4254, doi:10.1051/0004-6361/200810527. (Cited on page 3.)
- [174] M. Tavani et al. Direct Evidence for Hadronic Cosmic-Ray Acceleration in the Supernova Remnant IC 443. *Astrophysics Journal*, 710:L151–L155, 2010. arXiv:1001.5150, doi:10.1088/2041-8205/710/2/L151. (Cited on page 25.)
- [175] D. J. Thompson. Gamma ray astrophysics: the EGRET results. *Reports on Progress in Physics*, 71:116901, 2008. arXiv:0811.0738, doi:10.1088/0034-4885/71/11/116901. (Cited on page 4.)
- [176] D. J. Thompson et al. Calibration of the Energetic Gamma-Ray Experiment Telescope (EGRET) for the Compton Gamma-Ray Observatory. *The Astrophysical Journal Supplement Series*, 86:629–656, 1993. doi:10.1086/191793. (Cited on page 4.)
- [177] C. M. Urry and P. Padovani. Unified schemes for radio-loud active galactic nuclei. *Publications of the Astronomical Society of the Pacific*, 107:803, 1995. arXiv:astro-ph/9506063, doi:10.1086/133630. (Cited on pages 107 and 108.)

- [178] V. V. Vassiliev, S. Fegan, and P. Brousseau. Schwarzschild-Couder two-mirror telescope for ground-based γ -ray astronomy. In *Proceedings, 30th International Cosmic Ray Conference (ICRC 2007): Merida, Yucatan, Mexico, July 3-11, 2007*, volume 3, pages 1445–1448, 2007. [arXiv:0708.2741](#). (Cited on pages 18 and 22.)
- [179] F. L. Villante and F. Vissani. How precisely neutrino emission from supernova remnants can be constrained by gamma ray observations? *Physics Review*, D78:103007, 2008. [arXiv:0807.4151](#), [doi:10.1103/PhysRevD.78.103007](#). (Cited on page 65.)
- [180] F. Vissani and A. F. Aharonian. Galactic Sources of High-Energy Neutrinos: Highlights. *Nuclear Instruments and Methods in Physics*, A692:5–12, 2012. [arXiv:1112.3911](#), [doi:10.1016/j.nima.2011.12.079](#). (Cited on page 64.)
- [181] F. Vissani, F. A. Aharonian, and N. Sahakyan. On the Detectability of High-Energy Galactic Neutrino Sources. *Astroparticle Physics*, 34:778–783, 2011. [arXiv:1101.4842](#), [doi:10.1016/j.astropartphys.2011.01.011](#). (Cited on page 65.)
- [182] H. J. Voelk and K. Bernloehr. Imaging Very High Energy Gamma-Ray Telescopes. *Experimental Astronomy*, 25:173–191, 2009. [arXiv:0812.4198](#), [doi:10.1007/s10686-009-9151-z](#). (Cited on pages 15 and 16.)
- [183] Q. D. Wang, F.-J. Lu, and C. C. Lang. X-ray thread G0.13-0.11: a Pulsar wind nebula? *The Astrophysical Journal*, 581:1148–1153, 2002. [arXiv:astro-ph/0208371](#), [doi:10.1086/344401](#). (Cited on page 106.)
- [184] Q. Daniel Wang, F. J. Lu, and E. V. Gotthelf. G359.95-0.04: pulsar candidate near Sgr A*. *Monthly Notices of the Royal Astronomical Society*, 367:937–944, 2006. [arXiv:astro-ph/0512643](#), [doi:10.1111/j.1365-2966.2006.09998.x](#). (Cited on page 105.)
- [185] G. M. Webb, L. O’C. Drury, and P. Biermann. Diffusive shock acceleration of energetic electrons subject to synchrotron losses. *Astronomy & Astrophysics*, 137:185–201, 1984. (Cited on page 75.)
- [186] T. C. Weekes. *Very high energy gamma-ray astronomy*. Astronomy and Astrophysics. IOP, Philadelphia, PA, 2003. (Cited on pages 2, 7, 8, and 10.)
- [187] T. C. Weekes et al. Observation of TeV gamma rays from the Crab nebula using the Atmospheric Cerenkov Imaging Yechnique. *Astrophysics Journal*, 342:379–395, 1989. [doi:10.1086/167599](#). (Cited on page 1.)
- [188] B. Wiebel-Sooth, P. L. Biermann, and H. Meyer. Cosmic rays vii. individual element spectra: prediction and data. *Astronomy & Astrophysics*, 330:389, 1998. [arXiv:astro-ph/9709253](#). (Cited on page 34.)

- [189] R. R. Xue, P. H. Tam, S. J. Wagner, B. Behera, Y. Z. Fan, and D. M. Wei. Very High Energy γ - Ray Afterglow Emission of Nearby Gamma-ray Bursts. *The Astrophysical Journal*, 703:60–67, 2009. arXiv:0907.4014, doi:10.1088/0004-637X/703/1/60. (Cited on page 109.)
- [190] D. Zaborov, C. Romoli, A. M. Taylor, J. Lenain, D. Sanchez, and R. D. for the H.E.S.S. Collaboration Parsons. AGN observations with a less than 100 GeV threshold using H.E.S.S. II. *PoS, ICRC2015:808*, 2015. arXiv:1509.06509. (Cited on page 69.)
- [191] S. Zhu, J. Chiang, C. Dermer, N. Omodei, G. Vianello, S. Xiong, and the Fermi-LAT. Fermi-LAT Observations of the Gamma-ray Burst GRB 130427A. *Science*, 343(6166):42–47, 2014. arXiv:1311.5623, doi:10.1126/science.1242353. (Cited on page 109.)
- [192] V. N. Zirakashvili and F. A. Aharonian. Analytical solutions for energy spectra of electrons accelerated by nonrelativistic shock-waves in shell type supernova remnants. *Astronomy & Astrophysics*, 465:695–702, 2007. arXiv:astro-ph/0612717, doi:10.1051/0004-6361:20066494. (Cited on page 76.)
- [193] V. N. Zirakashvili and F. A. Aharonian. Nonthermal Radiation of Young Supernova Remnants: The Case of RX J1713.7-3946. *The Astrophysical Journal*, 708(2):965–980, 2010. doi:10.1088/0004-637X/708/2/965. (Cited on page 104.)
- [194] F. Zwicky. Die Rotverschiebung von extragalaktischen Nebeln. *Helvetica Physica Acta*, 6:110–127, 1933. doi:10.1007/s10714-008-0707-4. (Cited on page 99.)